

UNCLASSIFIED

AD NUMBER

AD482453

LIMITATION CHANGES

TO:

Approved for public release; distribution is unlimited.

FROM:

Distribution authorized to U.S. Gov't. agencies and their contractors; Critical Technology; MAY 1966. Other requests shall be referred to Arnold Engineering DevelopmentCenter, Arnold AFS, TN. This document contains export-controlled technical data.

AUTHORITY

AEDC ltr, 6 Oct 1982

THIS PAGE IS UNCLASSIFIED

AEDC-TR-66-25

ARCHIVE COPY
DO NOT LOAN

by /

STATUS OF RESEARCH ON
MAGNETOHYDRODYNAMIC AUGMENTATION OF
A SHOCK TUNNEL



Wendell Norman and R. R. Walker, III

ARO, Inc.

PROPERTY OF U. S. AIR FORCE
AEDC LIBRARY

May 1966 AF 40(600)1200

Approved for public release; distribution unlimited.

Per notice from W.O.
Cole dated 6 Oct 82
(CAF STINFO)

port controls
nts or foreign
approvals of

VON KÁRMÁN GAS DYNAMICS FACILITY
ARNOLD ENGINEERING DEVELOPMENT CENTER
AIR FORCE SYSTEMS COMMAND
ARNOLD AIR FORCE STATION, TENNESSEE

AEDC TECHNICAL LIBRARY
5 0720 00003316

NOTICES

When U. S. Government drawings, specifications, or other data are used for any purpose other than a definitely related Government procurement operation, the Government thereby incurs no responsibility nor any obligation whatsoever, and the fact that the Government may have formulated, furnished, or in any way supplied the said drawings, specifications, or other data, is not to be regarded by implication or otherwise, or in any manner licensing the holder or any other person or corporation, or conveying any rights or permission to manufacture, use, or sell any patented invention that may in any way be related thereto.

Qualified users may obtain copies of this report from the Defense Documentation Center.

References to named commercial products in this report are not to be considered in any sense as an endorsement of the product by the United States Air Force or the Government.

STATUS OF RESEARCH ON
MAGNETOHYDRODYNAMIC AUGMENTATION OF
A SHOCK TUNNEL

Wendell Norman and R. R. Walker, III
ARO, Inc.

This document is subject to special export controls
and each transmittal to foreign governments or foreign
nationals may be made only with prior approval of
Arnold Engineering Development Center.

FOREWORD

The results of this research were obtained by ARO, Inc. (a subsidiary of Sverdrup and Parcel, Inc.), contract operator of Arnold Engineering Development Center (AEDC), Air Force Systems Command (AFSC), Arnold Air Force Station, Tennessee, under Contract AF 40(600)-1200. The research was conducted under Program Element 62410034, Project 7778, Task 777806. The ARO Project No. was VJ2513, and the manuscript was submitted for publication on January 11, 1966.

The success of a project of this magnitude depends ultimately upon the people who contribute their various talents. It is a pleasure to acknowledge those who have made direct contributions to the work described in this report. The investigations of the performance capabilities of the two magnetohydrodynamic (MHD) augmentation concepts treated here were made possible by the help of Dr. Leon Ring, Propulsion Wind Tunnel Facility (PWT), and the computer programming assistance of Ernest Burgess and Charles Neel of the Scientific Computing Services, and Guy Gilley, John Duncan and Cecil Taylor of the Instrumentation Branch of the von Kármán Facility (VKF). The mechanical design of the accelerator and tube modifications were handled by Gerald Reagan and Robert Van Hook, VKF Test Operations. Design of electrical components was made by James Patterson, VKF Plant Operations, H. C. Daniels and Doyle Caffey, VKF Test Operations, and Steve Wallace and Mary Ann Scott, VKF Hypervelocity Branch. Instrumentation support was provided by Dave Bynum, James Ford, Olin Johnson, Joe O'Hare, and others of VKF Instrumentation. Within the Hypervelocity Branch, Dan Skelton, Pat Shelton, Robert Watkins, and George Butler have been responsible for operation of the experiments. John Lacey and Leo Siler have served as engineers in charge of conducting the tests and interpreting the results, as well as assisting in design of the components. The support of Allen Thomas and the personnel of the Hypervelocity Branch Shop deserves special mention. Finally, the major role played by the authors' colleagues Jack Whitfield and Glenn Norfleet should be pointed out.

This technical report has been reviewed and is approved.

A. G. Williams
Technology Division
DCS/Plans and Technology

Donald D. Carlson
Colonel, USAF
DCS/Plans and Technology

ABSTRACT

Two concepts for the augmentation of shock tunnel performance are analyzed. In the first of these, termed the buffer accelerator, a magnetohydrodynamic (MHD) accelerator is used to accelerate a buffer gas, which in turn drives a shock into the test gas. In the second approach, termed the nozzle accelerator, an MHD accelerator is used to accelerate the test gas directly. The latter approach is shown to be capable of providing higher velocities and longer test times, but the aerodynamic quality of the resulting test gas suffers because of the necessity of adding seed material to develop the conductivity required for accelerator operation. Descriptions are given of the major pieces of equipment that have been built for an experimental program to investigate the two augmentation concepts. These are (1) a 10^6 -joule capacitor bank for the electric field, (2) a $10\text{-weber}/\text{m}^2$ coil for the magnetic field, and (3) a buffer accelerator.

CONTENTS

	<u>Page</u>
ABSTRACT	iii
NOMENCLATURE	ix
I. INTRODUCTION	1
II. SOME GENERAL CONSIDERATIONS	3
III. BUFFER ACCELERATOR PERFORMANCE	7
IV. NOZZLE ACCELERATOR PERFORMANCE	18
V. BASIC APPROACH FOR EXPERIMENTAL STUDIES	26
VI. ELECTRIC FIELD SYSTEM.	27
VII. MAGNETIC FIELD SYSTEM	34
VIII. BUFFER ACCELERATOR.	46
IX. OPERATIONS	47
REFERENCES	48

ILLUSTRATIONS

Figure

1. Test Section Flow Energy.	55
2. Estimate of Usable Core Section Diameter	56
3. Percent Frozen Oxygen after Isentropic Expansion across Freeze Line	57
4. Altitude for Density and Frozen Speed of Sound Matching	58
5. Initial Pressure Required in Test Section for Perfect Start of Nozzle	59
6. Illustration of Duplication Lines	60
7. Schematic of Operation of Shock Tunnel with a Buffer Accelerator.	61
8. Schematic of Accelerator Process in x-t Plane	62
9. Schematic of Accelerator Processes in the Pressure-Velocity Plane	63
10. Processes for Reduced Pressure at Accelerator Exit	64
11. Nomenclature for Downstream Processes	65

<u>Figure</u>	<u>Page</u>
12. Shock Speed Ratio across MHD Buffer Accelerator	66
13. Schematic and Wave Diagram for MHD Buffer Accelerator Shock Tunnel.	67
14. Energy for Argon Buffer $P_8 = 1 \text{ atm}$	68
15. Minimum Energy Requirements for Argon Buffers	69
16. Summary of Theoretical Shock Tube Performance for Various Energy Additions	70
17. Ratio of Stagnation Enthalpy to Static Enthalpy behind a Moving Shock in Air	71
18. Duplication Capabilities of MHD Buffer-Augmented Shock Tunnels	72
19. Nomenclature for Test Time Determination	73
20. Illustration of Nomenclature for Buffer Accelerator . .	74
21. Nozzle Accelerator Schematic.	75
22. Limit Duplication Lines, Air with 1/4-percent Potassium Seed	
a. Supply Stagnation Pressure: 100 atm	76
b. Supply Stagnation Pressure: 1000 atm	77
c. Supply Stagnation Pressure: 5000 atm	78
23. Limit Duplication Lines, $B^2 L_a = 500 \text{ weber}^2/\text{meter}^3$, with 1/4-percent Potassium Seed	79
24. Schematic Diagram for a Lossless Transmission Line - Case One	80
25. Load Current as a Function of Time and Number of Sections in Transmission Line	81
26. Current in Each Loop of the Transmission Line as a Function of Time	82
27. Voltage across Section Capacitance as a Function of Time	83
28. Load Current as a Function of Time	84
29. Load Current as a Function of Accelerator Electrode Length for Different Gas Conductivities	87
30. Current Density as a Function of Accelerator Electrode Length for Different Gas Conductivities	88

<u>Figure</u>	<u>Page</u>
31. Electric Field Intensity as a Function of Accelerator Electrode Length for Different Gas Conductivities	89
32. Schematic Diagram for Lossless Transmission Line with a Load Consisting of Resistance and Inductance - Case Two	90
33. Load Current as a Function of Time and Load Inductance	
a. $L_{load} = 10^{-6}$ henries	91
b. $L_{load} = 10^{-6}$ henries	92
c. $L_{load} = 10^{-5}$ henries	93
34. Schematic Diagram for a Transmission Line with Uniform Resistance in Each Loop - Case Three	94
35. Load Current as a Function of Time and Line Resistance	
a. $R_{line} = 5 \times 10^{-5}$ ohms	95
b. $R_{line} = 5 \times 10^{-4}$ ohms	95
c. $R_{line} = 5 \times 10^{-3}$ ohms	96
d. $R_{line} = 5 \times 10^{-2}$ ohms	96
36. Schematic Diagram for a Transmission Line with Inductance and Resistance in Series with the Capacitor of Each Loop - Case Four	97
37. Load Current as a Function of Time and Load Resistance for $L_N = 0.128 \times 10^{-6}$ henries	98
38. Load Current as a Function of Accelerator Electrode Length and Gas Conductivity for $L_N = 0.128 \times 10^{-6}$ henries	99
39. Current Density as a Function of Accelerator Electrode Length and Gas Conductivity for $L_N = 0.128 \times 10^{-6}$ henries	100
40. Nondimensional Power, Energy, Current, and Voltage as a Function of Impedance Matching	101
41. Schematic Diagram for Simulated Transmission Line Electric Field System - Final Configuration	102
42. Range of Impedance Match as a Function of L_N , C_N , and Total Test Time	103
43. Photographs of Electric Field System and Components	104

<u>Figure</u>	<u>Page</u>
44. Schematic and Photograph of Air Gap Switch	105
45. Photograph of Coaxial Bus System to Accelerator Electrodes	106
46. Accelerator Electrode Voltage Balancing Network a. Schematic	107
b. Typical Electrode to Ground Voltage Traces	107
47. Typical Electrical Discharge Characteristics of Electric Field System Using Dummy Load	108
48. Magnetic Stresses in a Helical or Single-Turn Coil Caused by Magnetic Pressure	109
49. Maximum Magnetic Field - Limited by Yield Stress of Coil Material - All Coils	110
50. Magnetic Pressure Developed inside a Coil as a Function of Magnetic Field Level	111
51. Total Energy per Unit Inside-Coil-Volume Stored in a Magnetic Field	112
52. Dimensionless Axial Field of a Thick Coil, $\alpha = 3$, $\beta = 2$, J Constant with Radius	113
53. Normalized Coil Volume as a Function of β and α	114
54. Drawing of First Coil Design	115
55. Photograph of Half-Scale Coil Model	116
56. B-Field Distribution in Half-Size Model	117
57. Drawing of Final Coil Design	118
58. Photographs of Magnetic Field Coil a. Along Tube Axis	119
b. Along Coil Axis	120
59. Electrical Schematic of Magnetic Field System	121
60. Pictorial Representation of Tunnel F 100-megajoule Inductive Energy Storage System	122
61. Photograph of B-Field SW-4 Assembly	123
62. Typical B-Field Coil Charging - Discharging Cycle . .	124
63. Comparison of Measured Magnetic Field Distribution to Theory - Final Coil Installation	125

<u>Figure</u>	<u>Page</u>
64. Research Shock Tunnel System	127
65. Photograph of Buffer Accelerator Installation.	128
66. Photograph of Components of Buffer Accelerator . . .	129
67. Cutaway Isometric Drawing of Buffer Accelerator. . .	130

TABLES

I. Summary of D-C Coils in Operation	131
II. Summary of Pulse Coils in Operation	132
III. Summary of Current, Field, and Power Relations for Different Current Distributions	133
IV. Coil Data	135

NOMENCLATURE

A	Cross-sectional area of accelerator
A_e	Area of accelerator electrode
A_i	Cross-sectional area of accelerator at inlet
a	Speed of sound
a	Radial distance for coil
a_1	Inside radius of coil
a_2	Outside radius of coil
B	Magnetic field strength
b	Half-width of coil
E	Electric field strength
\dot{E}	Energy flow rate
h	Static enthalpy
I	Current
J	Current density

ℓ	Relative nozzle size (see Fig. 3)
l_a	Effective distance between accelerator electrodes
L	Length of shock tube; inductance
L_a	Length of accelerator
L_N	Length of nozzle
M	Flow Mach number
M_S	Shock Mach number
\dot{m}	Mass flow rate
N	Number of transmission line segments; number of turns in coil
P	Pressure
R	Gas constant
Re	Reynolds number
S	Entropy; stress; skin depth
s	Interaction parameter
T	Temperature
t	Time; turn thickness
Δt_L	Time lost in nozzle
U	Flow velocity
U_d	Energy density in a magnetic field
V	Voltage
V_L	Load voltage
V_{lim}	Limiting test section velocity
V_o	Initial bank voltage
V_T	Total coil volume
x	Distance
Z_o	Impedance
Z^*	Ratio of number of moles to number of moles at standard conditions
α	Form factor for coil, a_2/a_1
β	Form factor for coil, b/a_1

β	MHD accelerator loading factor, E/BU
γ	Ratio of specific heats
δ	Boundary-layer thickness
δ^*	Boundary-layer displacement thickness
λ	Ratio of cross-section of conducting material to total cross-sectional area
μ_0	Permittivity of free space
ν	Frequency
ρ	Density
σ	Scalar conductivity
σ	Conductivity, mhos

SUBSCRIPTS

Numerical:	Refer to Fig. 13
i	Inlet to accelerator
e	Exit of accelerator
o	Stagnation value
N	Value per transmission line segment
S. T.	Shock tube
T. S.	Test section

SECTION I INTRODUCTION

This report is concerned with research directed toward the development of an aerodynamic test facility capable of providing test-section conditions corresponding to flight in the atmosphere at velocities from 10,000 to 36,000 ft/sec, at altitudes between 50,000 and 250,000 ft. Because of energy considerations, such a facility must operate on a pulsed basis rather than providing a continuous flow. A companion report (Ref. 1) describes related work on a shock tunnel system which is an integral part of the effort.

Impulse aerodynamic facilities currently operating include hotshot tunnels, shock tubes, and shock tunnels. The limitations on the performance capabilities of hotshot tunnels are fairly well established (Ref. 2). Energy-density limitations of the arc chamber gas limit test-section velocities to about 10,000 ft/sec. By expanding the test gas close to the condensation point, these tunnels are capable of providing flows at a test-section Mach number of 20, at unit Reynolds numbers corresponding to flight at about 100,000 ft.

Shock tubes are capable of providing stagnation point simulation (stagnation pressure and stagnation enthalpy match those of freeflight) for the conditions of interest here. Shock tunnels provide Mach number-Reynolds number simulation similar to that provided by hotshots. The limitations on shock tube performance arise from a number of factors (Refs. 1, 3, and 4). Arc driven tunnels are limited by the energy loss by radiation in the driver (Ref. 5). Another limitation is the practical maximum pressure that can be contained.

Based on the results from hotshot tunnels and shock tunnels, along with a limited amount of free-flight data, dynamic forces and heat-transfer rates can be predicted reasonably well from the data from these facilities. Furthermore, the predicted Mach number independence of certain coefficients has been confirmed. At the lower densities various second-order effects are not independent of Mach number but depend upon M/\sqrt{Re} . This dependence has also been confirmed (Ref. 6).

At the higher free-stream velocities of interest here, it is expected that Mach number independence will not be valid. At these higher energy

conditions, the finite rates of the various reactions taking place in the gas become comparable to the flow transit time. To provide a reasonable simulation of these effects, it is necessary to match free-stream velocities (i.e., after-shock enthalpy). Matching of the free-stream Mach number is also desirable to duplicate the flow field; then the free-stream speed of sound should correspond to the value encountered in freeflight. To duplicate the reaction rates, matching of the ρL product, where ρ is the free-stream density and L a characteristic length, should also be imposed (Ref. 7). All of the above conditions imply that the free-stream Reynolds number is also matched. However, matching of the ρL product for a scale model implies a test-section density higher than the free-flight. It will be seen that obtaining all of these conditions simultaneously is extremely difficult. To simplify the presentation of performance curves, the scale effect will be neglected, so that the requirements are matching of velocity, density, and Mach number.

To attain the conditions as given above, it is necessary to have an airstream of high velocity and high density. Because of the limitations on available impulse facilities given earlier, it is apparent that a new approach is necessary. The approach chosen here is to augment shock tube performance by means of a magnetohydrodynamic (MHD) accelerator (Ref. 8), in which directed kinetic energy is added to the gas by means of an electrical discharge in a magnetic field, thereby creating an accelerating body force.

The MHD accelerator is essentially a means of adding energy to a moving gas stream. Two different augmentation approaches are considered here. The first is the buffer accelerator, in which the energy is added to a buffer gas, such as argon, which has been heated by a shock. The added energy causes an increase in shock speed. The shock whose speed has been increased is then driven into the test gas (air). The test gas is then expanded to the test-section conditions by a nozzle. In this approach, it is necessary to operate in a nonreflected mode (because of practical pressure limits), with the result that test times are small (fraction of a millisecond). However, the gas in which the test takes place is theoretically quite clean.

In the second augmentation approach, termed the nozzle accelerator, the MHD accelerator is placed in the nozzle section and accelerates the test gas directly. This is a much more efficient process, in terms of energy addition, than the buffer accelerator. However, to operate the accelerator, it is necessary to add a small amount of easily ionized seed material to the test gas to develop the necessary electrical conductivity (Ref. 8). The effect of this added material on the flow about the

test object, and the resulting measurable quantities are under study. It is not yet clear whether this seeding will present a major problem.

Following a section on general considerations, these concepts are discussed in some detail to establish the performance limits attainable with each. The remaining sections describe equipment that is being assembled to investigate experimentally the two concepts.

SECTION II SOME GENERAL CONSIDERATIONS

There are some considerations associated with obtaining a high velocity, high density flow which are significant regardless of the particular approach used; they are discussed in this section.

2.1 ENERGY REQUIREMENTS

Figure 1 gives the values of the flow energy in a usable test core of 7-ft diameter. Values are given in megajoules per millisecond of run time. The numbers also give the power for continuous operation in megawatts. The curve of 100 megajoules per millisecond corresponds to 10^5 megawatts on a continuous basis. This is approximately equal to the total, installed, electric generating power in the United States. Therefore, continuous operation in this regime is not feasible. The values in Fig. 1 are highly idealized because no losses have been taken into account. In the impulse-type facilities, the input energy will be higher than the test-section energy by a factor of from about 10 for highly favorable conditions to about 100 or more for less favorable conditions.

The attainable run time will probably be limited to about 1 msec. Run time limitations result both from the limitations of the gas supply and the available total energy. Existing capacitor energy supplies are limited to about 10 megajoules; inductive energy supplies can supply up to 100 megajoules, but probably cannot satisfy the 1-msec time requirement. New types of energy sources may then be necessary. Explosively driven MHD generators may fulfill the requirement.

2.2 BOUNDARY LAYERS AND HIGH EXPANSION RATIOS

Boundary layers always present a problem. For the situation considered here, there are two effects of interest, both of which cause an

increase in the total energy required. The first of these is the boundary-layer buildup in the nozzle. Figure 2 gives estimates of the geometric test-section diameter necessary to provide a specified usable core diameter at the indicated altitude-velocity point (Ref. 9). These estimates are based upon empirical correlation formulas developed for lower test-section velocities. To have a usable core of 7 ft, a geometric test-section diameter of about 15 ft is required. There will be a certain amount of flow energy in the boundary layer which must be provided for in the energy source.

The second effect occurs because the boundary layer places a lower limit on the inside diameter of shock tubes and MHD accelerators. On the other hand, large area expansion ratios are required to reduce the density of the flow to the desired value. The minimum shock tube diameter and the necessary expansion ratio may combine to give a test-section area that is several times the desired value. It is possible to obtain a realistic test-section size by bleeding off part of the test gas, but this represents a loss in energy.

2.3 RELAXATION PROCESSES AND MATCHING PROBLEMS

In a nozzle expansion, the static temperature falls quite rapidly. If the temperature range is high enough, a point is reached at which the composition of the gas cannot adjust rapidly enough for local equilibrium to be attained. The composition of the gas in the test section will therefore not be the same as that of equilibrium air at the same temperature and pressure.

There are at least two effects of this mismatch in composition that must be considered. The first is the effect of the nonequilibrium composition on the flow over the test object, and the influence on the resulting measurable quantities. This situation is not yet completely clear, although work is being done on this item (see, e.g., Ref. 10). The second factor is the effect of this altered composition on the nozzle flow, and these effects have been studied extensively (e.g., Refs. 11 and 12). There is first of all a reduction in the velocity at the nozzle exit, since a portion of the initial thermal energy is not available for conversion to kinetic energy. This is, for the application here considered, a minor effect. More important is the alteration in the pressure-density relation caused by the lower temperatures. At a point in the flow at which the temperature is a given value, the density will be higher because of the nonequilibrium effects.

Some very serious questions are raised by the fact that the conditions in the test section will not match the atmospheric composition,

and much more study of this problem is needed before definite answers are possible. For an equilibrium expansion, matching of density, velocity, and temperature implies matching of pressure and speed of sound. For a nonequilibrium expansion, this is not true. The density and velocity may be matched along with temperature or pressure or speed of sound. The actual choice will probably depend on the particular phenomenon being observed. Here, the choice is made to match density, velocity, and frozen speed of sound because it appears that frozen Mach number in a frozen flow most closely corresponds to the equilibrium Mach number in an equilibrium flow. Further study may reveal that, for some conditions, another choice should be made.

In recent years, much has been learned about nozzle processes, both from the analytical approach of Bray (Ref. 11) and the numerical studies performed at Cornell Aeronautical Laboratory (Ref. 12). As yet, sufficient experimental data to verify these results have not been obtained. For the conditions of interest here, the primary imbalance in the test section composition is in the atomic oxygen in the test gas. Figure 3 gives the percentage of the original oxygen that is in atomic form at the test section for a steady isentropic expansion. It should be noted that, as indicated in Fig. 3, the amount of the atomic oxygen frozen in expansion is, to a good approximation, independent of the reservoir enthalpy (or test-section velocity) and is a function of the entropy alone. For the condition in the atmosphere, the entropy is a function of the altitude alone, the values being indicated in Fig. 3. A value of the parameter ℓ of 0.1 cm corresponds to a small facility, whereas a value of 10 cm is appropriate for the large facility of interest here.

In Fig. 4, results are given that relate altitude to entropy for various processes. The upper curve corresponds to an equilibrium expansion,* the middle curve to an expansion with chemical freezing, with matching of the frozen speed of sound, and the lowest curve gives the result for an expansion with chemical and vibrational freezing. The degree of vibrational freezing is currently in dispute, but the differences are not a major factor here. The middle curve is arbitrarily used here.

Thus far, no way has been found to overcome the effects of freezing. All that can be done is to reduce the amount of mismatching as much as possible and hope that corrections to the experimental results can be made to account for these effects.

*Throughout this report, atmospheric properties are based upon Ref. 13; air properties are from Ref. 14 for temperatures above 1500°K and from Ref. 15 for temperatures below 1500°K.

2.4 HIGH PRESSURES

The low values of entropy associated with the low altitudes, as shown in Fig. 4, indicate that very high equivalent reservoir pressures are required. The pressure level will therefore have to be placed at the highest possible value, consistent with the capabilities in pressure vessel design.

2.5 LOW PRESSURES

Although very high pressures are required at one point, the need exists for very high initial vacuums in the test sections. If the initial pressure in the test section is too high, a secondary shock will form during the nozzle starting process, reducing the available run time (Ref. 16). Figure 5 gives the initial pressures required for a perfect start of the nozzle (no secondary shock). Attainment of pressure levels of 0.1 and 0.01 micron of mercury will require a great deal of effort. It should be noted that current shock tunnels apparently operate at initial pressures of 10 or 100 times that required for a perfect start. The reasons for this are beginning to be evident (see Ref. 17), but as yet, this is not on a firm basis.

2.6 THE DUPLICATION LINE AND TESTING AT A REDUCED MACH NUMBER

In describing the performance capabilities of a given device, use is made of the duplication line concept. As used here, duplication means matching of density, velocity, and frozen Mach number.

For a given physical setup, there is a limiting performance line. The limit may be established by pressure limitations, energy limitation, etc. In the upper part of Fig. 6, such a limiting duplication line is shown. Duplication, or matching of density, velocity, and Mach number, is possible with this particular setup above and to the left of this line. For altitudes above that indicated by A, the frozen oxygen content is greater than that at A, but for lower altitudes it is less.

It is possible to test at lower altitudes than those above the limit duplication line by relaxing the restriction of true Mach number and requiring only that the flow be hypersonic (Mach number greater than about 10). Testing at a reduced Mach number with matching of density and velocity involves testing at a higher static temperature (i. e., less expansion of the nozzle flow).

The duplication lines such as shown in the lower part of Fig. 6 are generally limit lines and are therefore not performance lines for a given physical setup. Determination of the duplication line for a given physical setup is a more difficult task and is not discussed herein.

2.7 ENTROPY PRODUCTION

The central problem of providing duplication capability in the desired regime can be related to entropy. To attain the desired velocities, specific amounts of energy must be added to the working fluid. To attain the altitude duplication, the entropy of the working fluid after the energy addition must not exceed a certain value. Therefore, the energy must be added very efficiently, in terms of entropy production.

The entropy of the working fluid can be written as the sum of two parts - the initial value and the value added in the energy addition process:

$$S = S_{\text{initial}} + \Delta S_{\text{energy addition}}$$

Energy addition by shock heating is very inefficient in terms of entropy production. For the nonreflected shock tunnel, it is necessary to work at very high pressures to keep the initial entropy low. For the MHD nozzle accelerator, the entropy production can be controlled to a certain extent, but the requirement for a low value of the initial entropy must be compromised with the conditions of temperature and pressure necessary for accelerator operation.

SECTION III BUFFER ACCELERATOR PERFORMANCE

3.1 DESCRIPTION OF OPERATION

The operation of a shock tunnel with a buffer accelerator is shown in Fig. 7. Diaphragm D1 separates the high pressure driver gas from the buffer gas. Upon rupture of this diaphragm, a shock wave S1 propagates into the buffer gas. The plane separating the two gases is termed the contact surface, * C1. The gas behind the shock S1 is accelerated in the accelerator so that the shock exiting from the accelerator has a higher velocity than it did before entering the accelerator. This

*Actually, this is a mixing region of finite thickness rather than a plane.

higher velocity shock then ruptures the diaphragm D2, and a shock wave S2 is driven into the test gas. The gas between the shock S2 and the contact surface C2 is the test gas, which is expanded in a nozzle to the test-section conditions. (The diaphragm D3 is inserted to allow the nozzle and dump tank to be evacuated).

This concept of MHD augmentation in the buffer of a shock tunnel was originally proposed by Jan van der Bliek, ARO, Inc., in 1963, in an unpublished report. Earlier, work had been done by Hogan (Ref. 18) on the operation of an accelerator of the type considered herein. His work, which was continued by Leonard (Ref. 19), was devoted to the understanding of the operation of the accelerator, and no consideration was given to driving the downstream shock into a test gas. A device very similar to the one considered herein is being studied by Leonard and Rose (Ref. 20) in which the accelerator is placed at the diaphragm D1. The driver gas, which has been seeded, is accelerated, causing an increase in shock speed in the test gas. This approach involves only two sections of tube rather than the three sections that are required for the buffer accelerator. The choice between these two devices depends upon the driver capability. Leonard and Rose use an electric arc driver for which the temperature of the driver gas after expansion is sufficient to generate the necessary conductivity. At VKF, work has been devoted to drivers with indirect heating, for which the temperature of the driver gas after expansion is too low to allow for operation of the accelerator. Therefore, the shock-heated buffer gas is used as the working gas within the accelerator.

3.2 ACCELERATOR AS A SHOCK-ACCELERATING DEVICE

There are two ways of studying the operation of an accelerator of this type. The first is the shock-acceleration approach of Rosciszewski and Oppenheim (Ref. 21). In their approach, the unsteady x-t characteristics are solved to obtain shock velocity as a function of distance. They are able to obtain an approximate solution for the case of an ideal gas by assuming that the shock is a U + a characteristic. This approach has not been followed herein because extension to a nonideal gas and removal of the assumption that the shock follows a characteristic would require a fairly elaborate computer program.

The second approach, and the one that is followed herein, is the steady-state approach. It is assumed that the accelerator operation is steady-state, and the exit conditions may be obtained by applying the steady-state flow equations. Since the item of interest for the buffer accelerator is the downstream shock speed, some means must be found for relating the accelerator exit conditions to the downstream shock speed.

Figure 8 shows the situation in the $x-t$ plane. The initial shock is accelerated and at the exit condition has a velocity corresponding to the point SA. The velocity of the shock at this point is that obtained by the shock-acceleration approach of Rosciszewski and Oppenheim. A more accurate evaluation requires solving the characteristics field between the shock trajectory and the indicated U - a wave. After the U - a wave has traversed the accelerator, steady-state conditions are established in the accelerator. The shock should attenuate after it leaves the accelerator. There are a number of reasons to expect this attenuation, but the main one is the matter of adjusting to the exit pressure of the accelerator. This attenuation of the shock causes the characteristics to coalesce into a secondary shock which moves downstream, although it faces upstream (i. e., the downstream pressure is greater than the upstream pressure). The region between the initial shock and the secondary shock is one of large entropy gradients because adjacent particles have passed through shocks of different strengths.

An alternate interpretation is given in Fig. 9, which is a plot of pressure and velocity. The shock polar gives the locus of conditions behind a shock propagating into a static medium with a pressure P_1 . Shock speed is a parameter along the polar. The inlet conditions to the accelerator (denoted by 1) are the same as the aftershock conditions (denoted by 2) at the inlet shock Mach number. The shock is accelerated, and the conditions at the exit of the accelerator at the instant that the shock leaves lie at the point SA on the same shock polar. The steady-state velocity at the accelerator exit (point e) is greater than the inlet velocity, but the pressure will in general not be too different from the inlet pressure. If it is assumed that the complicated processes are adequately described by simple processes, then the simple process connecting the exit conditions e with the shock polar is a secondary shock, as shown in the figure (Ref. 22, p. 226). The intersection of the polar for the secondary shock with the polar of the primary shock locates the points b and c, and the downstream shock Mach number is determined. The key assumption is, of course, that the processes are simple ones. This should be a fair assumption, since the matching is done on the basis of pressure and velocity, which are not seriously affected by the entropy gradients.

This secondary shock involves a loss in velocity, and therefore its effect should be minimized. The processes are quite similar to the starting processes in a hypersonic nozzle. Based upon this analogy, Dr. W. Warren* has suggested placing the accelerator next to the

*General Electric Co., Space Sciences Laboratory, Valley Forge Space Technology Center, King of Prussia, Pennsylvania.

diaphragm D2 and lowering the initial pressure in this region to the point that no shock forms. This is illustrated in Fig. 10. The practical disadvantage of this approach is that in order to have a high after-shock pressure, which is necessary for high density testing, the accelerator must operate at high pressure at the exit and even higher pressures at the inlet.

Thus, far, there is no experimental evidence to verify the existence of the secondary shock. The available experimental data (Refs. 18 and 19) indicate a large deceleration of the shock at the accelerator exit, but the deceleration is much greater than can be attributed to the formation of the secondary shock. This large deceleration was attributed to the rapid reduction in the magnetic fields at the accelerator exit (Refs. 18 and 19).

An approximate theory can be developed. Figure 11 illustrates the nomenclature. The unsteady processes of Fig. 8 have been omitted for simplicity. Ideal gases are assumed. Considering the downstream shock, M_{S_1}' , for high shock strengths ($M_{S_1}' > > 1$),

$$U_{2'} = \frac{2}{\gamma_{1'} + 1} M_{S_1'} a_{1'} \quad (1)$$

and

$$P_{2'} = \frac{2\gamma_{1'}}{\gamma_{1'} + 1} M_{S_1'}^2 P_{1'} \quad (2)$$

Across the secondary shock,

$$\frac{U_e - U_{3'}}{a_e} = \sqrt{\frac{2}{\gamma_1 (\gamma_1 + 1)}} \frac{\frac{P_{3'}}{P_e} - 1}{\sqrt{\frac{P_{3'}}{P_e} + \frac{\gamma_1 - 1}{\gamma_1 + 1}}} \quad (3)$$

The simplifying assumption is now introduced that $(\gamma_1 - 1)/(\gamma_1 + 1)$ can be neglected in comparison with $P_{3'}/P_e$. Thus

$$M_e = \frac{U_{3'}}{a_e} + \sqrt{\frac{2}{\gamma_1 (\gamma_1 + 1)}} \frac{\frac{P_{3'}}{P_e} - 1}{\sqrt{\frac{P_{3'}}{P_e}}} \quad (4)$$

Across the interface between 2' and 3', pressure and velocity are matched.

$$P_{2'} = P_{3'} \quad (5)$$

$$U_{2'} = U_{3'} \quad (6)$$

Combining the above gives

$$\frac{2\gamma_{1'}}{\gamma_{1'} + 1} - \frac{P_{1'}}{P_e} \left[1 + \sqrt{\frac{P_e}{P_{1'}}} \frac{a_{1'}}{a_e} \sqrt{\frac{\gamma_1(\gamma_1 + 1)}{\gamma_{1'}(\gamma_{1'} + 1)}} \right] M_{S_1'}^2 - \sqrt{\frac{\gamma_1\gamma_{1'}(\gamma_1 + 1)}{\gamma_{1'} + 1}} \sqrt{\frac{P_{1'}}{P_e}} M_e M_{S_1'} - 1 = 0 \quad (7)$$

This is a quadratic equation which gives the downstream shock speed, $M_{S_1'}$, in terms of the exit conditions, P_e , a_e , and M_e .

Now consider the case for which there is no diaphragm at the exit of the accelerator, so that

$$P_{1'} = P_1$$

$$a_{1'} = a_1$$

$$\gamma_{1'} = \gamma_1$$

The inlet conditions to the accelerator are

$$U_i = \frac{2}{\gamma_1 + 1} M_{S_1} a_1$$

$$P_i = \frac{2\gamma_1}{\gamma_1 + 1} M_{S_1}^2 P_1$$

Assume that the accelerator is of constant area so that

$$\rho_i U_i = \rho_e U_e$$

and assume further that the temperature is constant. This has been found to be a reasonable approximation for the case of an accelerator with a constant area, constant electric field, and constant magnetic field. With these assumptions, the following result is obtained:

$$\frac{M_{S_1'}}{M_{S_1}} = \frac{1}{2} \sqrt{\frac{\gamma + 1}{\gamma - 1}} \frac{\frac{U_e}{U_1} + \sqrt{\left(\frac{U_e}{U_1}\right)^2 + 4 \frac{\gamma - 1}{\gamma + 1} + 4 \sqrt{\frac{\gamma - 1}{\gamma + 1} \frac{U_i}{U_e}}}}{\sqrt{\frac{U_e}{U_1}} + \sqrt{\frac{\gamma + 1}{\gamma - 1}}} \quad (8)$$

This equation gives the shock speed ratio as a function of accelerator velocity ratio. Figure 12 gives a plot of Eq. (8) for $\gamma = 5/3$. Also shown are the results from computer solutions. The program was written by Guy Gilley, ARO, Inc., and it solves the accelerator equations in the form given in Ref. 26 and then crosses the necessary

downstream shocks. Gas properties are based upon a singly ionizing argon model. It is seen that Eq. (8) provides a reasonable estimate.

The relationship between the steady-state accelerator performance and the downstream moving shock speed given by Eq. (8) allows the increase in shock speed to be related to the energy added in the accelerator. Assuming that most of the energy goes into the gas as directed kinetic energy,* then

$$\dot{E} = \dot{m} (1/2) [U_e^2 - U_i^2]$$

and thus

$$\dot{E}/A_i = (1/2) \rho_i U_i^3 \left[\left(\frac{U_e}{U_i} \right)^2 - 1 \right] \quad (9)$$

Furthermore, the strength of the shock in the test gas can be determined in standard ways. Referring to Fig. 13, either an unsteady expansion fan or a rear-facing shock occurs between region b and region ⑥.

Given the above results, it is possible to relate the overall performance to the energy addition. Figure 14 gives, ** for a given driver (the 600°K externally heated driver of Ref. 1) and a given downstream pressure, P_8 , the energy added in the buffer as a function of the buffer shock Mach number, M_{S1} , and the downstream shock Mach number M_{S8} . It is seen that for a given downstream shock Mach number, there is an optimum value for the buffer shock Mach number. The optimum shock speeds are high enough to generate the conductivity necessary for accelerator performance. Using the minimum energy for a number of pressure gives the curves shown in Fig. 15. There can, therefore, be constructed an equivalent driver line as the basis of the energy added. Such a set of curves is given in Fig. 16. For reference purposes, the line for an after-shock pressure (P_7) of 5000 atm is shown. The possibility of using helium rather than argon as the buffer gas has also been investigated.

*The amount of energy that appears as thermal energy depends upon the specific accelerator design. For an isothermal accelerator it is zero, but for the constant area accelerator with constant electric field and constant magnetic field the thermal energy addition is about equal to the kinetic energy addition, as determined by computer solutions.

**These results were obtained from a computer program written by Cecil Taylor, ARO, Inc.

In practice, it would be necessary to seed the helium to develop the necessary conductivity. This study was motivated by the possibility that the energy loss by radiation from the shock-heated argon might prove to be serious.* The results indicate that helium is slightly more efficient than argon as a buffer gas, with the energy added being about 25 percent less. To the level of approximation of the analysis, this amount of energy addition is not particularly significant.

3.3 DETERMINATION OF TEST-SECTION CONDITIONS

Now the equivalent shock tube performance given in Fig. 16 will be related to the duplication capabilities. It will not be possible to reflect the shock wave and expand through a converging-diverging nozzle because the pressures would be extremely high (20,000 atm or greater). Therefore, the expansion of the gas in region ⑦ (Fig. 13), begins from the shock tube area, as shown in Fig. 7.

The test-section velocity will be close to the limiting velocity

$$V_{\text{lim}} = \sqrt{2 h_{7_0}}$$

where h_{7_0} is the stagnation enthalpy of the air behind the shock (region ⑦).

Figure 17 gives the ratio of the stagnation enthalpy to the static enthalpy for calculations (Ref. 24) based upon the most recent air data (Ref. 14). For simplicity, this ratio will be taken as constant at 1.79. The variations about this number are minor. Therefore,

$$V_{\text{lim}} = \sqrt{(2)(1.79) \frac{h_7}{h_8} h_s}$$

From Ref. 24, Fig. 2d, the static enthalpy ratio h_2/h_1 is very close to the ideal gas value, which for $\gamma = 1.4$ and large shock Mach numbers is

$$\frac{h_7}{h_8} = \frac{7}{36} M_s^2 \quad (10)$$

In addition,

$$h_s = 3.234 \times 10^6 \text{ ft}^2/\text{sec}^2$$

so that

$$V_{\text{lim}} = 1500 M_s \quad (11)$$

*The results of Ref. 23 indicate that at the high pressures of interest herein the absorptivity may be high enough that there will be little total heat loss, in which case this will not be a problem.

with V_{lim} in ft/sec. To obtain the entropy of the gas behind the shock, which determines the duplication altitude, two properties are needed. One of these is the enthalpy, which is given by Eq. (10). From Ref. 24, Fig. 2a, the pressure ratio is also close to the ideal gas value, which is

$$\frac{P_7}{P_8} = \frac{7}{6} M_{S_8}^2 \quad (12)$$

With the pressure and enthalpy determined, the entropy can be obtained (Ref. 14) and the altitude determined from Fig. 4. In using the results of Fig. 16, the shock speeds were multiplied by 0.75 before determining the after-shock conditions to make an approximate allowance for shock attenuation.

The duplication results are given in Fig. 18 for the equivalent shock tube performance given in Fig. 16, for the case of an attenuation factor of 0.75. It is seen that there can be significant improvement in the duplication capabilities by the addition of energy in the buffer. It should be pointed out that very large nozzle expansion ratios will be required.

3.4 TEST TIME CONSIDERATIONS

The useful test times with this device will be quite small. Referring to Fig. 19, the shock-tube test time is

$$t_{S.T.} = \frac{L}{U_7} - \frac{L}{U_{S_8}}$$

Using

$$U_7 = \left(1 - \frac{\rho_8}{\rho_7}\right) U_{S_8}$$

gives

$$t_{S.T.} = \frac{L}{M_{S_8} a_8} \frac{1}{\frac{\rho_7}{\rho_8} - 1}$$

From Fig. 2b of Ref. 24, ρ_7/ρ_8 is about 8 for the conditions of interest here. Therefore,

$$t_{S.T.} = \frac{L}{7 M_{S_8} a_8}$$

This is divided by two to account approximately for the test time loss attributable to interface acceleration (Ref. 25). Thus,

$$t_{S.T.} = \frac{L}{14 M_{S_8} a_8} \quad (14)$$

There is a loss in test time caused by the convergence of a U - a wave from the throat as initiated by the initial shock, and a U + a wave

from the throat as initiated by the contact surface (Ref. 16). For high test-section flow Mach number in a conical nozzle,

$$\Delta t_L = \frac{3.33}{M^2} \frac{L_N}{a_{T.S.}}$$

The flow Mach number can be written as

$$M = \frac{V_{lim}}{a_{T.S.}}$$

Using Eq. (11) gives

$$M = \frac{1500}{a_{T.S.}} M_{S_8}$$

in which the speed of sound in the test section, $a_{T.S.}$, is in ft/sec. Therefore,

$$\Delta t_L = \frac{3.33}{2.25} \frac{L_N}{M_{S_8}^2 a_{T.S.}}$$

The net test time at the test section is then

$$t_{T.S.} = t_{S.T.} - \Delta t_L = \frac{L}{14 M_{S_8} a_8} - \frac{3.33}{2.25} \frac{L_N}{M_{S_8}^2 a_{T.S.}}$$

For simplicity, let

$$a_8 = a_{T.S.} = 1000 \text{ ft/sec} = 1 \text{ ft/msec}$$

so that, with the test time in msec and the lengths in ft,

$$t_{T.S.} = \frac{L}{14 M_{S_8}} - \frac{3.33}{2.25} \frac{L_N}{M_{S_8}^2} \quad (15)$$

The shock speed for which the test time is maximum for given tube length and nozzle length is then

$$M_{S_8} = 41.5 \frac{L_N}{L} \quad (16)$$

and at this condition

$$M_{S_8} t_{T.S.} = \frac{L}{28} \quad (17)$$

If the tube length downstream of the accelerator is 100 ft, and the design condition such that $M_{S_8} = 20$, giving a test-section Mach number of 30, then the test time is 180 μ sec and the nozzle length 48 ft. At lower shock Mach numbers, more test time can be obtained by proper design, but the result is that test times will generally not exceed 200 μ sec (0.2 msec). It should be again noted here that some

allowances have been made for known factors affecting test time, e.g., interface acceleration and attenuation; thus the above test time estimates are as realistic as possible based on the present state-of-the-art.

3.5 DETAILS OF ACCELERATOR OPERATION

In the preceding analysis, the accelerator was treated as an energy addition device, but no consideration was given to the details of the accelerator. Now some basic considerations will be applied to determine the size.

The one-dimensional, steady-flow equations describing the accelerator operation are (Ref. 26)

Conservation of mass

$$\rho U A = \dot{m} = \text{constant} \quad (18)$$

Conservation of momentum

$$\rho U \frac{dU}{dx} + \frac{dp}{dx} = \sigma B(E - BU) \quad (19)$$

Conservation of energy

$$\rho U \left(\frac{dh}{dx} + U \frac{dU}{dx} \right) = \sigma E(E - BU) \quad (20)$$

(The nomenclature is illustrated in Fig. 20.) The system of equations is completed by the equation of state and the specification of three quantities. For the buffer accelerator, it is reasonable to assume that E , B , and the cross-sectional area, A , are constants.* A further reasonable approximation is to neglect the pressure gradient term in Eq. (19) and assume that the conductivity is constant. This equation may then be integrated to give

$$U_e = U_i + \left(\frac{E}{B} - U_i \right) \left(1 - e^{-\frac{\sigma B^2 L_a}{\rho U}} \right) \quad (21)$$

The asymptotic final value if E/B , and this velocity is achieved in a length for which the interaction parameter

$$s = \frac{\sigma B^2 L_a}{\rho U} \quad (22)$$

is about 2 or 3.

*It may be necessary to have some variation in E to overcome the maximum velocity increase limitation pointed out in Ref. 26.

To illustrate the relative magnitudes involved, the condition of $M_{S_8} = 20$, $P_g = 10$ atm is chosen. The following values were obtained as part of the computer solutions upon which Figs. 14, 15, and 16 are based:

$$P_i = 1.7 \text{ atm}$$

$$U_e/U_i = 8.5$$

$$M_{S_1} = 11$$

From these, the desired value of E/B is

$$\frac{E}{B} = 24,800 \text{ m/sec}$$

The estimated conductivity is 5×10^3 mho/m, and assuming an interaction parameter of 3 gives

$$B^2 L_a = 23$$

in which B is in weber/m², and the length L_a in meters. Therefore, an accelerator 1 m long with a B -field of 5 weber/m² is adequate. The E -field is then

$$E = 124,000 \text{ v/m} = 1240 \text{ v/cm}$$

For an electrode separation distance of 20 cm, the electrode voltage is 24,800 v. From Fig. 15, the energy flow rate is 5×10^8 joule/sec-cm² so that for a $400-\mu\text{sec}$ run* and a cross-sectional area of 400 cm², the ideal total energy required

$$\text{Energy} = (5 \times 10^8)(400 \times 10^{-6})(400) = 8 \times 10^7 \text{ joules}$$

The average total current is then

$$I = \frac{8 \times 10^7}{(400 \times 10^{-6})(24,800)} = 8 \times 10^6 \text{ amp}$$

This is quite a high value. ** The current density is concentrated at the

*The accelerator run time should be longer than the shock tube test time to allow for the fact that disturbances from the accelerator travel at the speed of sound relative to the flow. The amount of this has not been estimated.

**The high value of the total current suggests the possibility of using this current to generate the magnetic field by means of current loops in series with the electrodes.

leading edge, and the initial value is found to be

$$J_{\max} = 5.45 \times 10^4 \text{ amp/cm}^2$$

This is also a high value.

3.6 SUMMARY OF BUFFER ACCELERATOR

These estimates have shown that the buffer accelerator is capable of providing the capability for testing in a region which is not currently available. In the next section, the nozzle accelerator is considered, and it will be seen that this approach is also theoretically capable of providing coverage of a somewhat similar region. In many respects, the nozzle accelerator is considered to be superior to the buffer accelerator. However, the buffer accelerator has one major advantage: the test gas is clean. For the nozzle accelerator, it is necessary to add seed material to the test gas; therefore there is foreign material in the test gas. The choice between a buffer accelerator and a nozzle accelerator lies wholly in the seriousness with which the effect of the seed addition is viewed.

The primary disadvantage of the buffer accelerator is the short test time, which is on the order of 200 μsec . It may be possible to perform meaningful aerodynamic experiments within this time interval.

The success of a buffer accelerator depends upon a number of factors. The test program planned for the buffer accelerator has the following purposes:

1. Determination of the validity of the mathematical models used,
2. Determination of the overall efficiency, and
3. Investigation of the ability to draw large current densities in a diffuse sheet.

SECTION IV NOZZLE ACCELERATOR PERFORMANCE

4.1 DESCRIPTION OF OPERATION

A simplified schematic of a nozzle accelerator is shown in Fig. 21. The shock tube (which need not have a buffer section) generates a slug of high pressure, high temperature air.* The shock tube may be

*An alternate approach is to use a hot shot as the gas source (Ref. 28).

operated in a nonreflected mode, but in general the requirements of run time will dictate operation in the reflected mode, using either the tailored-interface or the equilibrium interface-technique (Ref. 27). The test gas from the shock tube is then accelerated by the MHD accelerator.

4.2 DISCUSSION OF ADVANTAGES AND DISADVANTAGES

The primary advantage of this approach is that the process is inherently more efficient than the buffer accelerator because the energy is added directly to the test gas. The disadvantage is the necessity of adding seed material to the test gas, since at the conditions for which air has any significant electrical conductivity the entropy exceeds that necessary for flight duplication at the altitudes of interest.

The intentional introduction of a foreign material into the test gas* must be viewed with suspicion especially because of the large effort that was necessary to reduce the contamination of hotshot tunnels to the point where the data were useful (Ref. 2). However, seed is necessary for the nozzle accelerator to be a workable device. The effects of this seed material upon the flow about the body are, at present, uncertain although the problem is being studied (Ref. 30). Some order-of-magnitude estimates given in Ref. 31 indicate that the seed may not adversely affect the flow, particularly at velocities above 30,000 ft/sec.

4.3 DUPLICATION CAPABILITIES

This particular approach has received extensive study. The theory is fairly well developed, and there exists a general optimization theory (Ref. 31). Other analytical studies are given in Refs. 8, 32, 33, and 34, which may be taken as representatives from a large body of available papers and reports. Experimentally, the emphasis has been upon accelerators for continuous operation (see Ref. 35), but the possibility of use with pulsed supplies is receiving increased attention (Refs. 28, 36, 37, and 38).

Because a considerable body of literature exists for the nozzle accelerator approach, no attempt will be made to present the analytical details. Instead, results from previous work will be cited.

*A means of seed injection is given in Ref. 29.

The particular results cited here are those given in Ref. 32. The analysis is based upon a set of operating conditions chosen as follows:

1. The applied magnetic field (B) is constant,
2. The static temperature is constant, and
3. The loading factor (E/BU) is constant.

The inlet conditions are chosen to maximize the test-section velocity for a given entropy. Although the particular set of operating conditions was chosen on the basis of analytical simplicity, the results from this approach agree well with those of a more exact theory, in which the optimum operating conditions are determined (Ref. 32). In addition, studies have been made of accelerators with some practical simplifications (primarily in the area distribution).

These studies show that the duplication limits are determined by three basic parameters:

1. seed concentration (i. e., conductivity);
2. the parameter $B^2 L_a$, where B is the externally applied magnetic field strength and L_a the accelerator length; and
3. the stagnation pressure of the reservoir supplying the accelerator.

A high value for each of these is called for. The first two of these parameters should actually be considered together since the governing combination is really the interaction parameter (Eq. 22) which contains the grouping $\sigma B^2 L_a$. The conductivity varies roughly as the square root of the seeding fraction; thus, calculations based upon one value of the seeding fraction can be used for other seeding fractions by making the proper adjustment in the parameter $B^2 L_a$.

The requirement for a high seeding fraction must be compromised with the difficulty of data interpretation if the test gas contains a large amount of seed. Since, at present, the degree of difficulty caused by seed is uncertain, the allowable seed fraction must be set arbitrarily. The studies that have been conducted to date have been based upon either 1/4- or 1/2-percent potassium seed. The actual contaminant concentration will probably be larger, since the potassium would in practice be introduced in the form of a compound.

The upper limit on the parameter $B^2 L_a$ may be set by a number of factors. At very high B -field levels, the internal magnet stresses may be large. At a magnetic field strength of 25 weber/m² this stress is 36,000 psi. By proper choice of material, this may be contained. Joule

heating is a problem for continuous operation, but it is probably not a factor here since the coil may be operated on a pulsed basis. Further discussion is given in Section VII. The length of the accelerator must not be such that boundary-layer buildup within the accelerator is a problem. Other practical problems may also limit the length. The energy in the B field, and therefore the energy required to generate the field on a pulsed basis, is proportional to the product of B^2 and the volume over which the field acts; therefore the energy varies directly as $B^2 L_a$. The actual energy necessary can be determined only by a detailed design, taking into account the various packaging problems.

The results of the calculations are given in Figs. 22 and 23. Results are given for three different values of the stagnation pressure, 100, 1000, and 5000 atm, representing three different levels of shock-tube performance.* The influence of the accelerator performance is shown by the three values of $B^2 L_a$ of 100, 500, and 2000 weber $^2/m^3$. The first of these values corresponds to a magnetic field of 5 weber/ m^2 with an accelerator length of 4 m (or other possible combinations). The higher values correspond to accelerator lengths of, say, 5 m, with resulting magnetic fields of 10 weber/ m^2 and 20 weber/ m^2 , respectively.

The figures illustrate first of all that this type of accelerator is limited to duplication of altitudes above 150,000 to 200,000 ft. In Ref. 8, the limits are given as from 100,000 to 150,000 ft. There are two reasons for these differences. The first is that here the more restrictive requirement of true test-section Mach number is imposed, rather than the requirement of a hypersonic Mach number used in Ref. 8. The second reason is that the relationship between altitude and entropy used in Ref. 8 is based upon an expansion with frozen chemistry and vibration, whereas here the relationship is based upon an expansion with frozen chemistry and vibrational equilibrium.

Figures 22a, b, and c show the effect of higher accelerator performance for a given supply stagnation pressure. The results show quite strongly the necessity of high values of $B^2 L_a$ if high test-section velocities are to be obtained at altitudes below 250,000 ft. For a supply pressure of 100 atm, the curves are terminated on the low-velocity end at the velocity for which the inlet Mach number is 1.5. The low-velocity termination point for the case of a 5000-atm supply is the limit of the tables of Ref. 19.

*Shock tube performance depends upon stagnation temperature as well as stagnation pressure, but for these calculations the temperature is implicitly determined by the requirement of adequate electrical conductivity.

Figure 23 illustrates the effect of the supply for a given accelerator ($B^2 L_a = 500 \text{ weber}^2/\text{m}^3$). From this it is seen that the influence of the stagnation pressure is not as strong as that of the accelerator performance, which is perhaps not too surprising.

In comparing the capabilities of the nozzle accelerator as given in Fig. 22 with those of the buffer accelerator as given in Fig. 18, it is seen that the nozzle accelerator provides a capability at the high velocities that the buffer accelerator cannot provide. The buffer accelerator, on the other hand, provides coverage of the high density (low altitude), moderate velocity area, which the nozzle accelerator does not cover.

4.4 SPECIFIC CASE

To illustrate the magnitudes of the parameters involved, a specific case will be assumed. Take from Fig. 22b the case for a test-section velocity of 30,000 ft/sec at a duplication altitude of 200,000 ft. The parameter $B^2 L_a$ is then $2000 \text{ weber}^2/\text{m}^3$, which could be provided by a magnetic field strength of $20 \text{ weber}/\text{m}^2$, and an accelerator length of 5 m.* A shorter accelerator with larger magnetic field strengths would be desirable. The reservoir pressure is 1000 atm.

From Ref. 8, the optimum accelerator inlet conditions are

$$T_i = 3000^\circ\text{K}$$

$$P_i = 7.67 \text{ atm}$$

$$S/R_i = 31.4$$

Because of the uncertainty in the conductivity estimates, the inlet conditions are taken at a higher temperature.** Therefore, take

$$T_i = 3500^\circ\text{K}$$

$$S/R_i = 31.4$$

$$P_i = 21.0 \text{ atm}$$

$$\rho_i = 0.129 \text{ lb}/\text{ft}^3$$

*Smaller values are obtained if the seeding fraction is increased above 1/4 percent.

**Recent unpublished studies have shown that in order to keep the magnitude of the Hall potential reasonable, even higher inlet temperatures are required.

The reservoir conditions are determined by the stagnation pressure and the inlet entropy

$$P_o = 1000 \text{ atm}$$

$$S/R_o = 31.4$$

from which

$$T_o = 6100^\circ\text{K}$$

The shock tube conditions required to obtain these conditions in the reflected region are

$$M_S = 8.8$$

$$P_1 = 1 \text{ atm}$$

Therefore

$$U_i = 10,450 \text{ ft/sec}$$

$$M_i = 2.9$$

The mass flow rate through a usable core of 7-ft diameter is

$$\begin{aligned} \dot{m} &= \rho A U \\ &= (1.29 \times 10^{-5}) (38.5) (30,000) \\ &= 15 \text{ lb/sec} \end{aligned}$$

From Fig. 2, the geometric diameter would have to be about 15 ft. The mass flow entrapped in the boundary layer in the test section is not definite, but the total mass flow rate will be less than four times that through the core. Therefore, as an approximation, take the mass flow rate through the accelerator as

$$\dot{m} = 50 \text{ lb/sec}$$

This assumes that the boundary-layer buildup occurs primarily downstream of the accelerator. The inlet area is then

$$\begin{aligned} A_i &= \dot{m} / \rho_i U_i \\ &= 50 / (0.129) (10,450) \\ &= 0.0371 \text{ ft}^2 \\ &= 5.34 \text{ in.}^2 \end{aligned}$$

which requires an inlet diameter of 2.31 in.

The accelerator exit conditions are found to be

$$T_e = 3500^\circ K$$

$$P_e = P_i/e = 7.73 \text{ atm}$$

$$\rho_e = \rho_i/e = 0.0475 \text{ lb/ft}^3$$

$$(S/R)_e = 32.4$$

$$U_e = 29,800 \text{ ft/sec}$$

$$M_e = 8.2$$

$$A_e = 5.1 \text{ in.}^2$$

An exit diameter of 2.26 in. is required. Continuity considerations therefore call for a slight decrease in flow area through the accelerator, which is undesirable for other reasons. In practice, a sufficient increase in area must be provided to eliminate the possibility of choking caused by boundary-layer formation. The amount necessary is not known absolutely, but it is assumed that a small additional divergence angle of 1 or 2 deg on the walls of the accelerator will be sufficient.

By use of a real air expansion, the nozzle throat area is found to be 0.00805 in.^2 , calling for a diameter of 0.28 in.

Turning now to the power supply requirements for the accelerator, the energy added in the accelerator is ideally

$$\begin{aligned} E &= \dot{m} (U_e^2 - U_i^2)/2 \\ &= 8 \times 10^8 \text{ joule/sec} \\ &= 0.8 \text{ megajoule/msec} \end{aligned}$$

The power supply requirement then depends upon the run time and the overall efficiency. A run time of 2 or 3 msec should be possible at this shock tube condition. The overall efficiency is unknown, but assuming provisionally a value of 10 percent gives as the energy requirement or 24 megajoules for 3 msec.

The maximum voltage required may be estimated by using the fact that at the exit the loading factor

$$\beta = E/BU$$

is close to unity. Therefore

$$E = (20) (29,800 \times 0.3048)$$

$$= 182,000 \text{ v/m}$$

The potential difference across the core is

$$\begin{aligned} V &= (182,000) (2.26/39.37) \\ &= 10,450 \text{ v} \end{aligned}$$

To this must be added the voltage drop in the boundary layers, which is at present unknown. In any event, the E-field power supply must have a voltage capability of from 10 to 20 kv.

The accelerator will be built of segmented electrodes, with individual floating power supplies for each pair, to neutralize the Hall voltage (Ref. 8). The magnitude of this Hall potential is estimated at from 10 to 40 kv. There are a number of problems to be studied in regard to the number of electrodes required and the insulation thickness between adjacent electrodes that is necessary to prevent shorting caused by the Hall potential.

Estimates of the energy requirement for the magnetic field power supply are more difficult to obtain since the total volume over which the B-field is generated must be known. This total volume must take into account the increase in accelerator size attributable to boundary-layer growth as well as the various packaging problems. At a B-field level of 20 weber/m², the energy stored in the field is about 8×10^8 joules per cubic meter of unit inside coil volume. The internal volume of the accelerator, not including boundary-layer corrections, is 0.0168 m³. On this basis, the ideal energy requirement is 1.34×10^7 joules. Therefore, the actual energy requirement to provide the B field on a pulsed basis will be perhaps 100 megajoules. This is indeed a large value, and study must be devoted to this particular aspect of the problem to keep it within bounds. It is interesting to note that the energy requirement to provide the B-field is greater than that required to provide the E-field.

The purpose in presenting this specific case is not to provide an actual design but to point out the problem areas and areas of uncertainty. Design of an actual facility requires answers to some of these problems as well as more complete parameter studies.

4.5 SUMMARY OF NOZZLE ACCELERATOR

The nozzle accelerator has the theoretical capability of providing a test capability approaching escape velocity for altitudes above 150,000 to 200,000 ft.

The primary areas that need study are

1. seeding, both in regard to technique and effect on flow about test object;
2. boundary layers, both in the accelerator channel and the nozzle;
3. determination of overall efficiency;
4. working with high voltages and high energies on a pulsed basis; and
5. electrode segmentation.

SECTION V BASIC APPROACH FOR EXPERIMENTAL STUDIES

The two previous sections have pointed out that of the two possible approaches to MHD augmentation of a shock tube, the buffer accelerator theoretically provides a clean test gas but short test times, whereas the nozzle accelerator requires the addition of a seed material to the test gas. The choice between the two depends upon the relative importance of a clean test gas and test time for the class of problems to be studied. For aerodynamic tests the clean test gas will probably be the governing consideration, whereas for propulsion tests the test time may be the key item.

Because of the lack of data for either approach, it was decided to perform experimental studies for both. Following these preliminary studies, one of the two approaches will be selected as the most promising, and further work will be performed.

The guiding consideration in the present research program is to develop a test setup that, with minor modification, can be used for investigating both the buffer accelerator and nozzle accelerator concepts. For either of these, there are four basic items needed: (1) a shock tube, (2) an electric field supply, (3) a magnetic field power supply and a magnet, and (4) an accelerator. Of these four items, the first three are common; the major difference is in the accelerators. The buffer accelerator can consist of a single pair of electrodes, whereas the nozzle accelerator will have a number of segmented electrodes. This difference leads to certain differences in the power supply requirements, and of necessity there will be modifications to the tube to accommodate the accelerators. Fortunately, these differences are not major.

In discussing the components in the remainder of the report, the design for the buffer accelerator is given. The buffer accelerator was

chosen for initial investigation, because an AEDC-funded program on the nozzle accelerator was underway elsewhere (Ref. 36).

Considering first the shock tube, the existing Tunnel J shock tube was selected because of its availability and performance. Planned development of drivers for this tube is adequate for the purposes here. Reference 1 gives in detail the capabilities and planned development of this tube.

The electric field power supply must be sufficiently flexible to operate as a single bank for the buffer accelerator and as a number of independent banks for the nozzle accelerator. Capacitors fulfill this requirement quite well; therefore the existing 10^6 -joule Hotshot 1 capacitor bank (Ref. 2) was relocated. This particular bank consists of 4000-v cans, and stacking is necessary to develop the required voltages. A description of this bank is given in Section VI.

The decision was made to use the existing Tunnel F generators as the power supply for the magnetic field and to procure a special coil. Since the generators are of relatively low voltage, a large cross-sectional area in the coil is required. By judicious design, a potential magnetic field strength of 10 weber/m^2 was obtained, which is sufficiently high to perform meaningful experiments. The possibility also exists for increasing the attainable field strength. The details of this component are given in Section VII.

The final component is the accelerator. The design for the buffer accelerator is given in Section VIII. The design of the nozzle accelerator is not complete.

SECTION VI ELECTRIC FIELD SYSTEM

6.1 INTRODUCTION

Because of considerations presented in previous sections of this report and other factors, the general design criteria for the electric field system were to deliver 10^6 joules of electrical energy into a conditioned gas behind the shock wave within a specific time duration, with a given pulse shape, and at specific electric field and current density levels. The conductivity of the accelerator inlet gas could be varied one and one-half orders in magnitude, depending on the particular shock tube performance regime.

The specific electric field system design criteria were determined to be as follows:

This performance capability required a very versatile energy storage system. After studying existing VKF energy storage systems, it was concluded that a simulated transmission line made from an existing 10^6 -joule, 4-kv capacitor bank would be preferable to existing inductive energy storage systems, and, therefore, theoretical studies were made to determine the system characteristics and required values for various parameters.

6.2 THEORETICAL STUDIES

Several case studies were made to determine the effects of various parameters. These studies were made using an analog computer programmed with the exact differential equations. The following relationships were used from Ref. 39.

- ### (1) Characteristic impedance for a lossless line

$$Z_o = \left(\frac{L_N}{C_N} \right)^{\frac{1}{2}} \text{ ohms} \quad (23)$$

The terms L_N and C_N are the inductance and capacitance of each section measured in henries and farads, respectively.

(2) Pulse Duration

$$t = 2N [L_N C_N]^{1/2} \text{ sec} \quad (24)$$

where N = number of transmission line sections employed.

(3) Load Voltage

$$V_L = V_0 \left(1 - \frac{Z_0}{R_L + Z_0} \right) \quad (25)$$

V_0 = initial voltage on capacitors in volts

R_L = resistance of load in ohms

(4) Load Current

$$I_L = V_L / R_L \text{ amp} \quad (26)$$

In addition, the MHD accelerator channel resistance was assumed to be

(5) Resistance of the Channel

$$R = \frac{1}{\sigma} \frac{l_a}{A_e} \quad (B = 0) \quad (27)$$

where

l_a = effective distance between
accelerator electrodes, m

A_e = area of accelerator electrode, m^2

σ = electrical conductivity, mho/m

From the accelerator dimensions given in Section VIII and the geometrical considerations of Fishman (Ref. 40), this equation becomes

$$R_L = \frac{0.336 \times 10^2}{\sigma L_a} \quad (B = 0) \quad (28)$$

where

σ = electrical conductivity, mho/m

L_a = length of accelerator electrodes, in.

(6) Current Density (Neglecting the UB Term)

$$j = \sigma E \quad (29)$$

where

E = electric field intensity, v/m

The following cases were considered:

6.2.1 Case One

The simplest case considered was the lossless transmission line as shown in Fig. 24. For this case, with a matched load (i.e., $R_L/Z_0 = 1$) and values of the various parameters in the range of interest, the effect of varying the number of sections in the line (Fig. 25) was to decrease the pulse duration as the number of loops decreased while the average current level remained the same. Figures 26 and 27 show the behavior for the matched case of the loop currents, and the voltage across each section capacitance as a function of time. Figure 28 shows typical plots of the shape of the current pulse through the load for various values of R_L/Z_0 where the characteristic impedance, Z_0 , was constant and the resistance, R_L , was varied according to Eq. (28) for a number of electrode lengths and gas conductivities. Figures 29, 30, and 31 summarize the plots of Fig. 28 plus many others not presented herein by showing the variation of load current, current density, and electric field intensity with accelerator electrode length and gas conductivity.

6.2.2 Case Two

Having seen in Section 6.2.1 that a reasonably square pulse could be obtained across the load with the desired range of current density, the effect of adding inductance to the load was considered as shown schematically in Fig. 32. With the resistance of the channel, R_L , equal to the characteristic impedance, Z_0 , it was evident (Fig. 33a) that for a small value of inductance (10^{-6} henry) the average current across the load remained the same as for the case with no inductance (Fig. 25) and that the inductance removed most of the ringing effect at the initial part of the current pulse. This value of inductance changed the rise time by less than 2 percent. However, for larger values of inductance (5×10^{-6} and 10^{-5} henries, Figs. 33b and c), the rise time changed considerably, the pulse shape was no longer square, and the average current did not reasonably approach the value in Fig. 25. It was therefore desirable to limit the inductance in the load to approximately the value of L_N to obtain a smooth pulse.

6.2.3 Case Three

The circuit in Fig. 34 considered the effect of resistance in the cables connecting the capacitors, and calculated results for such a circuit are shown in Fig. 35. A comparison of the pulse shapes (Figs. 33a and 35a) revealed that a small resistance in each loop (-5×10^{-5} ohms) had very little effect on the shape or value of the current across the load,

but as this value was increased to 5×10^{-3} ohms (Fig. 35d) the initial slope decreased slightly, there was a slight decrease in the average current, and the current began falling off sooner. It was therefore desirable to limit the resistance in each section to one milliohm or less.

6.2.4 Case Four

The final case considered the total effect of line and load inductance and line resistance as shown schematically in Fig. 36. It was desirable to study the current which could be obtained for several pulse durations as determined by Eq. (24). Since the value of C_N could not be decreased without losing energy for a given load voltage requirement, five arbitrary values of L_N were selected to give pulse widths from 0.4 to 2.0 msec in 0.4-msec increments.

Figure 37 shows the behavior of the current across the load for one of the five values of inductance for the matched case. This plot and other matched and unmatched cases not presented herein are summarized for one of the five values of inductance in Fig. 38. The effect of accelerator electrode length and gas conductivity on the load current is given in Fig. 38 and the effect on current density in Fig. 39.

Although all the pulse durations are not presented herein, the pulse duration lengthened as the value of inductance increased (Eq. (24)), but as the inductance increased the maximum current which could be obtained decreased. Also, as the inductance increased, the current density which could be obtained with a specific load resistance decreased. Therefore, when the current pulse lengthened, the current density obtainable decreased.

Maximum energy transfer in the specified pulse time was obtained with a matched ($R_L = Z_0$) load. Figure 40 shows normalized energy delivered in the first pulse as a function of the degree of mismatch. Normalized current through and voltage across the load are also plotted as a function of normalized load resistance in Fig. 40.

6.3 SYSTEM DESCRIPTION

Based on the analog computer studies presented herein and other local design considerations, the electric field system configuration that was built is that which is shown schematically in Fig. 41. Referring to Fig. 41, the electric field (E-field) system consisted of a ten-section, simulated transmission line, an air gap switch, the load bus, and the accelerator electrodes through which (when $B = 0$) a resistive gas flowed.

Each of the ten sections of the simulated transmission line consisted of capacitance, line resistance and inductance, and a variable inductance. The section capacitance was provided by 50 "can-stacks" connected in parallel. Each can-stack consisted of two 125- μ f, 4-kv rated capacitors connected in series to provide 62.5 μ f at 8 kv in each can-stack, making a total section capacitance of 3.125 millifarads at a design rating of 8 kv. The line resistance and inductance was due to the parallel combination of 200 RG8A/U coaxial cables, each 75 ft long, connecting the section capacitance to a collector plate. Each can-stack was connected to the collector plate by four parallel cables. The total line resistance was 1.04 milliohms and the total line inductance, 0.0286 microhenry (μ h). The 75-ft length of each cable was due to a multiple accelerator location test plan and the desire to keep the inductance, resistance, and capacitance of each section balanced. The range of impedance matching as a function of section inductance, capacitance, and total pulse time is shown in Fig. 42. The variable inductance was provided by either 1 or 2 turn inductors of variable diameter to give the values shown in Fig. 41. The inductors were physically located between the collector plates of each section and were made from 1- by 1-in. cross-section, heat-treated aluminum bar stock. Figure 43 shows photographs of the racked capacitors of each section, the current collector plate, and the installed inductors between each section.

The ten sections were connected in series as shown in Fig. 41 and were switched on by means of an air gap switch shown in Fig. 44. The current pulse was fed through a coaxial bus system* to the accelerator electrodes as shown in the photograph in Fig. 45. A discussion of the accelerator is provided in Section VIII.

Because of the requirement for quickly disconnecting the load bus from the accelerator electrodes and the time element involved in the original fabrication of the load bus, a higher inductance ($L_{bus} \approx 0.8 \mu h$) was obtained than was desirable.

The "switching on" of the electric field was accomplished by the circuitry shown schematically in Fig. 44. For normal operation, the tungsten-tipped gap electrodes were spaced such that the gap would hold off 2 kv more than the bank charge voltage to prevent premature self-firing caused by changes in humidity, dust in the gap, et cetera. The

*An improved bus system was installed later because the bus system shown in the photograph was found to transmit forces to the electrodes.

automatic gap firing system, designed by Mr. D. S. Bynum, ARO, Inc., sensed the pressure rise behind the shock wave with a pressure transducer immediately downstream of the driver diaphragm and, provided, the pressure level was at a predetermined level, transmitted a 10-msec permissive pulse, only during which the gap could be fired automatically. With the permissive pulse provided, when the shock wave arrived at a given station upstream of the accelerator electrodes, the system sensed the passing shock wave with an ionization probe and transmitted a pulse to a time delay unit. After a predetermined time delay, the third electrode in the auxiliary gap was pulled to ground potential via a thyratron firing and the auxiliary gap then conducted current. This placed the 20-kv auxiliary capacitors across the gap switch. The very short pulse from the auxiliary capacitors broke down the gap, and the voltage balance network drew a small sustaining current until the discharge across the electrodes was underway. Inductance between the gap and capacitors and between the gap and the accelerator was essential for this mode of operation. The time resolution in synchronizing the switching on the electric field with the shock wave is on the order of a few microseconds. The accelerator electrode voltage balancing circuit shown in Fig. 46 was used to balance the voltage between each electrode and the accelerator housing (ground potential) to relieve a critical electrode insulation problem inside the accelerator.

The remaining components of the electric field system consisted of a standard 8-kv charger and high voltage relays for disconnecting during discharge, a grounding switch system for grounding when not in use, a crowbar switch, and a crowbar load for dumping the energy in the bank.

Standard instrumentation measurements included total current, total electrode voltage, voltage between each electrode and the accelerator housing (ground potential), voltage across the air gap switch, and rate of change of current. All voltage measurements were made using a standard voltage divider and were displayed on an oscilloscope and the oscilloscope traces photographed. The rate of change of current was measured by means of a calibrated search coil wound toroidally around the inner conductor of the coaxial load bus. The current measurement was made by passively integrating the rate-of-change-of-current measurement. Both dI/dt and the current were displayed on oscilloscopes and the oscilloscope traces photographed.

6.4 SYSTEM PERFORMANCE

To determine the performance of the E-field system, about sixty discharges were made into dummy load resistors which were matched

to the characteristic impedance of the system. The dummy load discharges were made at various initial voltage levels and with different inductors. The discharge characteristics were in good agreement with theory except for the 400- μ sec case for which the stray inductance of the system was significant relative to the inductance of the inductors. This resulted in a longer pulse duration and a slower initial rise time.

Oscilloscope traces of total current, total electrode voltage, voltage between each electrode and ground (balancing network), voltage across air gap switch and rate of change of current for a typical low level dummy load run are shown in Fig. 47.

SECTION VII MAGNETIC FIELD SYSTEM

7.1 INTRODUCTION

As the MHD parametric studies progressed, it became more and more evident that high-level, transient, magnetic fields over large volumes would be required for high performance, pulsed MHD accelerators. In addition to the high magnetic field levels, the magnetic field had to be tailored along the channel axis at the entrance and exit of the accelerator to prevent large kinetic energy losses in the working gas.

As a result, a study of previous, high magnetic field work was made with particular emphasis on the following general magnetic field system design criteria:

1. Magnetic Field Level: 0-10 weber/m²
2. Field Distribution: Uniform throughout accelerator electrode length and decreasing uniformly to zero along channel axis in not less than 5 tube diameters (-8 in.) at both entrance and exit of accelerator
3. Pulse Time Duration: Minimum of 2000 μ sec
4. Pulse Shape: Uniform through pulse time duration
5. Pulse Synchronization: Magnetic field to be on when electric field "switched on" upon arrival of shock wave

6. Field Volume: A minimum consistent with the required field distribution along the channel axis
7. Energy Source: From existing AEDC-VKF energy storage systems

To meet the above design criteria, a detailed search of the literature was made to determine the theoretical considerations required and to compile the fundamental coil parameter relationships necessary for a coil design.

7.2 THEORETICAL CONSIDERATIONS

7.2.1 Summary of Applicable Work by Others

In the literature (Refs. 40-68), coils for producing high magnetic fields are generally classified into three broad categories: (1) d-c coils, (2) pulse coils, and (3) superconducting coils. The coils may or may not be operated continuously, and may or may not be cooled, but are generally operated for longer durations of time than pulse coils and are usually cooled in some manner. Pulse coils are usually used in applications where the duration of the pulse time is on the order of millisecond or less and almost always are not cooled since during such short times the total heat that can be transferred is usually small. This provides an inherent temperature limitation. Superconducting coils are operated at temperatures below their superconducting critical temperature and can be pulsed or operated indefinitely without generating Joulean heat. Because of the availability of low impedance, unipolar generators, superconducting and short time pulse coils were eliminated very early in the study. In this section, the fundamental parametric relationships applicable to uncooled, long pulse duration (~ 10 sec) coils are presented.

7.2.1.1 Summary of Existing Coils

Powerful d-c coils have long been used to study various magnetic effects; however, by far the majority of the cases were such that the higher fields were produced over very small volumes. This was unfortunate from the MHD point of view since high fields over large volumes were desirable; however, much was gained from studying the work of others, while at the same time keeping in mind the large volume requirements.

The first powerful d-c coil was constructed by Francis Bitter at MIT in 1939 (Ref. 69). The coil consisted of a stack of flat copper

washers and insulating spacers, split and connected so that the washers form a continuous helix for the current path. This coil produced 10 weber/m² over a volume of 25×10^{-6} m³ and was water cooled.

For a long time the Bitter coil was the only one in the world which could produce such high fields. In the last decade, however, powerful coils have been constructed in several countries and are summarized in Table I along with other pertinent information. In their complex of equipment, cooling principle and design, they are basically similar to Bitter's coil.

The first pulse coil for producing strong transient magnetic fields was constructed by Kapitsa (Ref. 42) in 1923-1927. With this device, magnetic fields of 50 weber/m² were achieved. Pulse techniques were further developed in 1956-1961 such that regular investigations could be made at field levels of 70 weber/m². Since then, extremely high magnetic fields have been generated, the highest reported in the literature being 1400 weber/m², produced by chemical implosion at Los Alamos (Ref. 43). Table II summarizes the more important of the existing pulse coils along with other pertinent data.

From the d-c coils field-power relations, very high magnetic fields require very high power levels. The principal advantage of a pulse system is the ability to store energy over a long period of time and discharge the energy through the coil in a short time, thus generating very high transient power levels, and relying on thermal inertia to prevent overheating.

Thus, by this crude definition of a pulse coil, the same general d-c coil parameter relationships hold provided "skin effect" is taken into consideration when defining the current density distribution in the conductors of the pulse coil.

7.2.1.2 Coil Parameter Relationships

According to Montgomery (Ref. 70), of the several ways of generating a magnetic field, the choice is dictated by considerations of field magnitude, volume, duration, power, weight, and space. Thus, it was of interest to summarize the relationships between field, current, power, and volume for a uniform current distribution, a Bitter radial current distribution, a Gaume current distribution, and a Kelvin current distribution. These current distributions are sketched at the top of Table III. In general, the relations summarized in Table III are essentially the same as those of Montgomery (Ref. 70).

7.2.1.3 Magnetic Stresses in Coils

The interaction between magnetic fields and currents produces forces. For a cylindrical coil these forces act in such a manner as to compress the coil axially and enlarge the coil radially. Thus, according to Furth (Refs. 40 and 41) the axial magnetic field of an air core coil behaves like a two-dimensional gas that exerts a radial pressure mathematically identical with the magnetic energy density,

$$\begin{aligned} P_m &= \frac{B^2}{2\mu_0} \text{ newton/m}^2 \\ &= 57.5 B^2 \text{ lb/in.}^2 \end{aligned} \quad (30)$$

where

$$B = \text{weber/m}^2$$

$$\mu_0 = 4\pi \times 10^{-7} \text{ for free space}$$

Generally, for a thick-walled coil, the stresses are simply treated using thick-walled pressure vessel theory. Referring to the coil model shown in Fig. 48, Furth gives the radial stress at any point (a) as

$$S_a = P_m \frac{1}{a^2 - 1} \left(1 - \frac{a_2^2}{a^2} \right) \text{ where } \alpha = a_2/a_1 \quad (31)$$

and the tensile stress at any point (a) as

$$S_\theta = P_m \frac{1}{a^2 - 1} \left(1 + \frac{a_2^2}{a^2} \right) \quad (32)$$

for α large

$$S_a = P_m \left(\frac{a_1}{a} \right)^2 \quad (33)$$

$$S_\theta = P_m \left(\frac{a_1}{a} \right)^2 \quad (34)$$

Thus, the maximum tensile stress is equal to P_m . Figure 49 shows the approximate magnetic yield points of various metals in terms of the B -field. Another way of interpreting Fig. 49 is in terms of the highest steady-state magnetic field that can be attained using various coil materials before the material begins to yield. Furth (Ref. 41) has made a large number of tests to verify the above relations and the attainable levels given in Fig. 49.

The above relations only relate to the bursting stresses, and do not take into account inertial effects. There are also axial compressive

stresses which must be considered. According to Montgomery (Ref. 70), the maximum average value of the axial compressive stress is approximately 20 percent of the bursting stresses and except for insulation considerations can generally be ignored.

7.2.1.4 Skin Effect Considerations

In Bitter-type pulse coils, the current distribution is governed by skin depth phenomena. The skin depth is defined as the depth below the surface at which the current density is $1/e$ of its value at the surface. The skin depth, S , is a function of frequency, resistivity, and permeability. Stratton (Ref. 44) gives the relation

$$S = \left(\frac{2\rho}{\omega\mu} \right)^{1/2} \text{ meters} \quad (35a)$$

where

ρ = resistivity in ohm-meter

ω = frequency in radians per second ($= 2\pi\nu$)

ν = frequency in cycles per second

μ = permeability of material, $4\pi \times 10^{-7}$ for a nonmagnetic medium

For copper at 293°K, $\rho = 1.72 \times 10^{-8}$ ohm-meter. Thus, Eq. (35a) becomes for copper

$$S = (6.6 \times 10^{-3}) \nu^{-1/2} \text{ meters} \quad (35b)$$

For a 1-msec pulse (~ 500 cycle/sec), the skin depth in copper is only 0.295×10^{-2} m or about 3 mm. Thus, it is seen that most disc-type pulse coils have somewhat large unused portions of conducting medium which are used only for additional strength and as a sink. If this additional strength and heat capacity are not needed, then it is obvious that the maximum radial thickness of the individual coil turn should be on the same order as the skin depth.

According to Montgomery (Ref. 70), in determining the various parameter relations for a pulse coil, if $S/a_1 > 1$, $j(a)$ quite closely approximates the d-c case of a $1/a$ current distribution; however, in most pulse coils $0 < S/a_1 < 1$ and the current drops off much faster than $1/a$. Thus, if a is close to 1, a very reasonable approximation can be found by assuming the current is $1/a$ since the field is not very dependent on the current distribution for this case. Further, it is generally conventional to assume the current is $1/a$ when calculating inductance and resistance, and thus the actual values of L and L/R

can be expected to be smaller and R larger when assuming a $1/a$ current distribution.

7.2.2 High Transient Magnetic Fields for MHD Accelerators

For high performance pulsed MHD accelerators, high transient magnetic fields are required over large volumes. In addition, the magnetic field must be tailored along the channel axis at the entrance and exit of the accelerator to prevent large kinetic energy losses (Ref. 19) in the working gas.

7.2.2.1 Type of Coil for a Pulsed MHD Accelerator

The desired duration of the $\bar{j} \times \bar{B}$ force acting on the gas in the high performance pulsed MHD accelerator is on the order of one millisecond. Therefore, the simplest type of coil to use for the B-field would be a pulse coil. This is particularly true if the switching synchronization of the E- and B-fields can be readily achieved. The pulse coil is most desirable mainly because the complex cooling system can be eliminated and thus a greater degree of design freedom is allowed in the coil and accelerator configuration. However, skin effect presents a more difficult situation in the B-field tailoring problem. This can be overcome by providing for a "forced" current density distribution in the coil wall and will be discussed more thoroughly later.

In any event, the superconducting coil is presently eliminated if the B-field levels required exceed about 10 weber/m^2 . Although a plain, cooled coil can be pulsed and has the advantage of lower I^2R heat generation since R is lower, the overall gain is usually negative because of the refrigeration system that is required. Thus, for these reasons, an attempt should be made to design the B-field coil to operate in a pulse duration regime where the skin effect is low enough to be tolerated and yet the cooling system can be left out of the design.

7.2.2.2 Coil Configurations for MHD Accelerator

In general, just about any reasonable coil configuration can be built to provide the B-field for an MHD accelerator, provided funds are available. The coil parameter relations presented in Table III apply; however, an "effective" α , B, and a_1 will have to be applied where the coil geometry used is other than that described herein.

7.2.2.3 Large B-Field Volumes for MHD Accelerator

Although in most of the experimental work noted herein small B-field volumes were used, large volumes are strictly a matter of

funds (Ref. 51, i.e., coil and power supply costs). Since magnetic pressure is a function of B^2 , a larger inside-diameter-coil presents a greater problem in the design of the de facto pressure vessel. A plot of the magnetic pressure developed, using the relation (Eq. (30))

$$P_m = \frac{B^2}{2\mu_0} \text{ newton/m}^2$$

or

$$P_m = 57.5 B^2 \text{ lb/in.}^2$$

where B is in weber/m², is shown in Fig. 50 as a function of B .

7.2.2.4 Energy in the B-Field for MHD Accelerator

The energy density, U_d , in a magnetic field is

$$U_d = \frac{B^2}{2\mu_0} \text{ joule/m}^3 \quad (36)$$

To find the total energy, one must know $B(x, y, z)$ over all space and integrate over all space. This is most often difficult to do. By thinking in terms of an ideal coil (one where no flux linkages exist within the coil wall), then every flux line outside the coil must also continue inside the coil. Therefore, by taking the inside volume (V_I) of the coil and multiplying by B_0 at the center of the coil yields, very approximately, one-half the total energy required.

Thus, the maximum total energy, U_T , that can be stored in the magnetic field is

$$U_T = \frac{B_0^2}{\mu_0} V_I \text{ joules} \quad (37)$$

A plot of the total energy per unit inside volume (V_I) of the coil is shown in Fig. 51. In addition to the energy stored in the magnetic field, the Joulean heat energy must be added to arrive at the total energy required.

7.2.2.5 Attainable Magnetic Field Levels for MHD Accelerator

From the graph in Fig. 49, it is seen that magnetic field levels up to about 60 weber/m² can be attained without destroying or damaging the coil. The limiting factor in this case is the tensile yield strength of the coil material (assuming adequate cooling or mass to limit the temperature rise in the coil). Further, this assumes a suitable structure can be designed to contain the de facto pressure vessel. The design of a d-c coil to produce a steady-state magnetic field level of 60 weber/m² would be a formidable engineering problem and would be very expensive.

7.2.2.6 Tailoring the Magnetic Field at the Entrance and Exit of a MHD Accelerator

According to Leonard (Ref. 19) it is necessary to tailor the magnetic field at the entrance and exit of a MHD accelerator to prevent high kinetic energy losses in the working fluid. This can be done simply by choosing the proper wall thickness for the coil at the entrance and exit of the MHD accelerator. Figure 52 shows a nondimensionalized plot of the radial variation of the axial field component at several axial stations. It should be pointed out that this plot is for constant current density with radius, a given α and B , and it does not consider skin effect. For pulse coils the skin effect can be greatly reduced by a forced current distribution through the coil wall. One way to accomplish this is to wind the turns of the coil in a spiral so that the current in the inner turns must also flow in the outer turns. This will not only force the desired current distribution in the wall, but also, according to Furth (Ref. 40), will reduce the magnetic pressure at the inside coil wall and the temperature rise in the skin volume.

Based on the high magnetic field theory and other considerations presented herein, it was concluded that

1. Although the production of B-field levels is a formidable engineering problem, levels of 60 weber/m² (600,000 gauss) could be attained for use with large MHD accelerators.
2. To properly tailor the entrance and exit B-field distribution along the accelerator channel axis, a forced current distribution in the coil wall must be provided if the skin depth is small relative to the coil wall thickness.
3. The radial coil structure must be designed such that it can withstand 57.5 B² lb/in.² equivalent gas pressure acting radially on the inside surface of the coil wall at a given B-field level and that the axial coil structure must be capable of withstanding in compression approximately 20 percent of the radial pressure.
4. Although coils have not been built to produce 60 weber/m² over volumes on the order of a few cubic meters, such coils seem technically if not economically feasible.
5. Due consideration should be given MHD pulse generators to drive such a coil so that the high costs of power supplies can be drastically reduced.

7.3 DESIGN OF MAGNETIC FIELD COIL FOR RESEARCH MHD ACCELERATOR

Based on the general magnetic field system design criteria and the theoretical considerations presented herein and on other studies not

herein presented, the following specific design criteria were established for the present MHD accelerator magnetic field coil design:

1. Magnetic Field Level: 10 weber/m² maximum throughout accelerator electrodes
2. Field Distribution: Uniform throughout accelerator electrode length of 12 in., which dictated an inside coil diameter of 18 in.; and uniformly decreasing to zero in not less than 8 in., which dictated a forced current distribution in the coil wall. Also, the coil wall thickness could not be less than 8 in.
3. Pulse Shape: Damped RLC circuit pulse shape with seconds of relatively little change at peak of pulse.
4. Pulse Time Duration: A maximum of 10 sec because of the time constant of low voltage energy storage system selected as energy source.
5. Pulse Synchronization: Because of the long pulse time of B-field pulse, E-field to be fired on peak of pulse.
6. Field Volume: Inside diameter of coil to be sufficiently large to provide the required channel axis field distribution and also to provide space to connect E-field load bus to accelerator electrodes.
7. Energy Source: Existing AEDC-VKF Tunnel F 100-Megajoule Inductive Energy Storage System. Maximum voltage of 90 v and maximum current of 10⁶ amp, where both do not occur at the same time because of decay in speed of motor-generator sets.
8. Temperature Rise: Maximum $\Delta T \approx 125^{\circ}\text{F}$
9. Coil Shape: Circular design because of high magnetic pressures, and, further, coil shape must be compatible with accelerator housing.

With the above specific design criteria, the coil was originally designed as indicated below.

From the relation (assuming uniform current distribution)

$$B_0 = \mu_0 a_1 J \lambda [f(\alpha, \beta)] \text{ weber/m}^2$$

where the nondimensional coil parameters α and β are defined as shown in Table III and λ is the ratio of current conducting area to total area. For

$$B_0 = 10 \text{ weber/m}^2$$

$$a_1 = 9 \text{ in.}$$

$$\mu_0 = 4\pi \times 10^{-7} \text{ henry/m}$$

$$\lambda = 0.9 \text{ (assumed from other coil designs)}$$

$$J = 25,000 \text{ amp/in.}^2 \text{ (based on allowable total temperature rise of } 125^\circ\text{F in 10 sec)}$$

the $f(\alpha, \beta)$ was computed to be

$$f(\alpha, \beta) = 1.0$$

For the value of $f(\alpha, \beta) = 1.0$, using the plot of normalized volume versus β with α the running parameter as shown in Fig. 53, the values of α and β for a minimum volume in the coil were selected. These values were taken as

$$\alpha = 2.555 \quad \text{and} \quad \beta = 1.667$$

which, when actually calculated, give a value for $f(\alpha, \beta) = 1.06$. This 6-percent margin was provided to compensate for a reduction in field strength at the center of the coil that was caused by holes through the coil walls. The holes were provided so that the accelerator tube could extend through the coil in an area of maximum field strength.

From the selected values of α and β , other coil parameters were computed as follows:

Total Coil Volume:

$$\begin{aligned} V_T &= 2\pi a_1^3 [\beta (\alpha^2 - 1)] \\ &= 42.2 \times 10^3 \text{ in.}^3 \end{aligned}$$

Total Current per Turn:

$$I_T = \frac{(v_T \lambda \rho) J^2}{E_{coil}}$$

Allowing 65 v for the coil after bus voltage drop,

$$I_T = 255,000 \text{ amp}$$

Number of Turns:

$$N = \frac{A_T \lambda J}{I}$$

$$N = 37 \text{ turns}$$

Area per Turn:

$$A_N = \frac{1}{J \lambda}$$

$$A_N = 11.34 \text{ in.}^2$$

Outside Diameter:

$$2a_2 = 2\alpha a_1$$

$$= 46.0 \text{ in}$$

Coil Length:

$$2b = 2\beta a_1$$

$$2b = 30.0 \text{ in.}$$

Turn Thickness:

$$t_{N_{total}} = \frac{A_N}{2b}$$

$$= 0.378 \text{ in.}$$

$$\begin{aligned} t_{N_{copper}} &= t_{N_{total}} \lambda \\ &= 0.340 \text{ in.} \end{aligned}$$

$$\begin{aligned} t_{N_{insulation}} &= t_{N_{total}} - t_{N_{copper}} \\ &= 0.038 \text{ in.} \end{aligned}$$

Magnetic Pressure Inside Coil:

$$P_{m,radial} = \frac{B_c^2}{2\mu_0}$$

$$= 5750 \text{ psi}$$

A sketch of this coil design is shown in Fig. 54. A half-scale model of this coil was built, and measurements were made of the magnetic field distribution along the MHD accelerator channel axis to determine the effect of the accelerator holes through the coil walls. A photograph of this model is shown in Fig. 55, and the measurements of the magnetic field distribution along the MHD accelerator channel axis are shown in Fig. 56.

The original design of the coil shown in Fig. 54 specified turns made of copper sheet, spirally wound to give 37 turns and a hole bored through the coil walls for the accelerator tube to go through. Because of a copper shortage and long lead times required for copper sheet, an alternate design was chosen where copper magnet wire was substituted for the copper sheet. In addition, however, the magnet wire had to be wound around the accelerator tube hole to make the inner spirals, or pancakes, effective. This proved to be difficult to do, and as a result several design changes were made to make fabrication easier. A 4-in.-thick insulator was added between the coil halves, and smaller spacers were added between each coil pancake to provide proper pancake spacing so that backup load bearing area between turns would be sufficient. These necessary design changes resulted in other changes in α , β , and the number of turns to get the desired magnetic field level at the center of the coil. The final design was done in the same manner as the first design except using new values of α , β , N , and λ that were compatible with the fabrication technique. A drawing of the final coil that was built is shown in Fig. 57, and a photograph of the coil installed is shown in Fig. 58. The final values of the various coil parameters are compared to the original values in Table IV.

7.4 SYSTEM DESCRIPTION

An electrical schematic of magnetic field system is shown in Fig. 59. The system consists of the coil (final design) previously described, the Tunnel F unipolar generators, the interconnecting bus, associated switchgear, and the necessary control system.

A pictorial representation of the Tunnel F inductance energy storage system is shown in Fig. 60, and a description of its normal operation and performance characteristics is given in Ref. 71.

The switch SW-4 (Fig. 59) consists of eight, 3000-amp-rated, disconnect switches ganged together and actuated by an air cylinder. The switches are mounted on 20-kv insulators. The bus connecting the coil to SW-4 consists of 42 paralleled 1000-MCM cables approximately 150 ft long and were designed to allow a 20-v drop in the bus at 280,000 amp. Photographs of the SW-4 installation and the terminating cables are shown in Fig. 61. Overvoltage protection for the coil when SW-4 interrupts the current after a pulse is provided by a resistor and a voltage breakdown disc, both connected in parallel with the coil (Fig. 59). The control system on the generators only regulates the generator terminal voltage down to approximately 0.75 v, and thus, when SW-4 interrupts, the resistor in parallel limits the coil voltage to 2000 v or less. The over-voltage discs back up the resistors and are set to break down at a voltage slightly higher than 2000 v.

A typical coil charging cycle is shown in Fig. 62. The long time at maximum current through the coil was necessary because of the non-repeatability of the shock tube diaphragm rupture and will be reduced when better repeatability is achieved.

7.5 SYSTEM PERFORMANCE

The measured magnetic field levels inside the coil are compared with theory in Fig. 63, and the agreement is considered satisfactory.

SECTION VIII BUFFER ACCELERATOR

The buffer accelerator was located near the entrance to the driven tube (accelerator goes through magnetic field coil) as is shown in the drawing of the research shock tunnel system in Fig. 64. Figure 65 shows a photograph of the installed accelerator relative to the B-field coil and other shock tube components. A photograph showing the components of the accelerator is given in Fig. 66. The details of construction and assembly can best be seen in the isometric cutaway drawing shown in Fig. 67.

The inside diameter of the accelerator was made 40 mm to reduce the total energy required. The accelerator housing was made of a non-magnetic 303 stainless steel and was designed to contain a maximum pressure of 10,000 psi. A Plexiglas® window with three ports was provided for viewing the electric discharge. The electrodes through the

accelerator housing and the electrode conducting surfaces were made of BeCu for strength and conductivity. Except for the epoxy resin insulation on part of the backside of the conducting surface, all insulators inside the accelerator were nylon.

Versatility was provided in the design so that any length of electrode conducting surface from 0.5 to 12 in. could be used. Also, the current path to the conducting surfaces could either be through the upstream or downstream electrode position, depending on the desired effect.

During E-field discharge studies, some difficulty was experienced with the epoxy resin potting on the conducting surfaces. Improved potting techniques and an electrode-to-ground voltage balancing circuit (Fig. 46) proved to be a satisfactory solution to this insulation problem.

SECTION IX OPERATIONS

The operational testing of the equipment described in this report has alternated with the shock tube operation described in Ref. 1.

The initial tests were made over the period from February 18 to May 21, 1965, and consisted of discharges without the magnetic field. During these tests the emphasis was on working out instrumentation, equipment, and timing problems. These tests indicated difficulties with the accelerator, which was redesigned to provide more electrical insulation. These tests also provided a base from which to compare operation with the magnetic field. Operations with combined electric and magnetic fields were undertaken on September 21, 1965.

A segmented-electrode accelerator is currently being designed for the basic experiments on the nozzle accelerator. Initially, tests will be conducted with the accelerator in the same position as the present buffer accelerator, with a complete nozzle installation at a later date if the initial results are encouraging. During the time period between the conclusion of the buffer accelerator tests and the segmented-electrode tests, a number of shock tube tests will be made (Ref. 4).

REFERENCES

1. Whitfield, Jack D., Norfleet, Glenn D., and Wolny, W. "Status of Research on a High-Performance Shock Tunnel." AEDC-TR-65-272, to be published.
2. Lukasiewicz, J., Jackson, R., and Whitfield, J. D. "Status of Development of Hotshot Tunnels at the AEDC." The High Temperature Aspects of Hypersonic Flow, Pergamon Press, 1964.
3. Bird, K. D., Martin, J. F., and Bell, T. J. "Recent Developments in the Use of the Hypersonic Shock Tunnel as a Research and Development Facility." Third Hypervelocity Techniques Symposium, Denver, March 1964.
4. Flagg, R. F. "Advances in Shock Tunnel Driving Techniques." Third Hypervelocity Techniques Symposium, Denver, March 1964.
5. Camm, J. C. and Rose, P. H. "Electric Shock Tube for High Velocity Simulation." Avco-Everett Research Report 136; AF CRL-62-568, July 1962.
6. Whitfield, J. D. and Griffith, B. J. "Hypersonic Viscous Drag Effects on Blunt Slender Cones." AIAA Journal, Vol. 2, No. 10, October 1964, pp. 1714-1721.
7. Gibson, W. E. "Dissociation Scaling for Nonequilibrium Blunt-Nose Flows." AEDC-TDR-62-25 (AD 271079), February 1962.
8. Ring, L. E. "General Considerations of MHD Acceleration for Aerodynamic Testing." AEDC-TDR-64-256 (AD 453419), December 1964.
9. van der Bliek, J. A. von Kármán Institute for Fluid Dynamics Course Note 45, Rhode St. Genese, Belgium, May 1964.
10. Inger, G. R. "Similitude of Hypersonic Flows over Slender Bodies in Nonequilibrium Dissociated Gases." AIAA Journal, Vol. 1, No. 1, January 1963, p. 46.
11. Bray, K. N. C. "Simplified Sudden-Freezing Analysis for Non-Equilibrium Nozzle Flows." American Rocket Society Journal, Vol. 31, 1961, p. 831.
12. Lordi, J. A. and Mates, R. E. "Nonequilibrium Expansions of High-Enthalpy Airflows." Cornell Aeronautical Laboratory Report No. AD-1716-A-3, March 1964.

13. U. S. Standard Atmosphere 1962, U. S. Government Printing Office, Washington, D. C., 1962.
14. Hilsenrath, J. and Klein, M. "Tables of Thermodynamic Properties of Air in Chemical Equilibrium Including Second Virial Corrections from 1500°K to 15,000°K." AEDC-TR-65-58(AD612301), March 1965. See also: Lewis, Clark H. and Neel, C. A. "Specific Heat and Speed of Sound Data for Imperfect Air." AEDC-TDR-64-36(AD609469), May 1964; Neel, C. A. and Lewis, Clark H. "Interpolations of Imperfect Air Thermodynamic Data I. At Constant Entropy," AEDC-TDR-64-183(AD605471), September 1964, II. At Constant Pressure." AEDC-TDR-64-184(AD446386), September 1964.
15. Humphrey, R. L. and Neel, C. A. "Tables of Thermodynamic Properties of Air from 90 to 1500°K." AEDC-TN-61-103 (AD262692), August 1961.
16. Glick, H. S., Hertzberg, A., and Smith, W. E. "Flow Phenomena in Starting a Hypersonic Shock Tunnel." AEDC-TN-55-16 (AD56231), March 1955.
17. Smith, C. E., Jr. "An Analytical Study of the Starting Process in a Hypersonic Nozzle." Proceedings of the 1964 Heat Transfer and Fluid Mechanics Institute.
18. Hogan, William T. "An Experimental Investigation of a Magnetogasdynamics Accelerator." Project Squid, Technical Report MIT-28-T-P, April 1962. See also "Engineering Aspects of Magnetogasdynamics." Proceedings, 3rd Symposium March 1962, Gordon and Breach.
19. Leonard, R. Leon. "Operation of a $J \times B$ Accelerator in the Steady State." Master of Science Thesis, MIT Department of Mechanical Engineering, June 1963. See also AIAA Journal, Vol. 3, No. 1, January 1965, p. 115.
20. Leonard, R. Leon and Rose, Peter H. "Design and Operation of a Large Pulsed $J \times B$ Accelerator." Sixth Symposium on Engineering Aspects of Magnetohydrodynamics, April 1965.
21. Rosciszewski, J. and Oppenheim, A. K. "Shock Interaction with an Electromagnetic Field." The Physics of Fluids, Vol. 6, No. 5, May 1963.
22. Glass, I. I. and Hall, J. Gordon. "Shock Tubes," Section 18, Handbook of Supersonic Aerodynamics, NAVORD Report 1488, Vol. 6.

23. Pomerantz, J. "The Influence of the Absorption of Radiation in Shock Tube Phenomena." J. Quant. Spectrosc., Radiat. Transfer, Vol. 1, pp. 185-248.
24. Lewis, Clark H. and Burgess, E. G., III. "Charts of Normal Shock Wave Properties in Imperfect Air." AEDC-TDR-64-43 (AD 433958), March 1964.
25. Mirels, H. "Test Time in Low Pressure Shock Tubes." Physics of Fluids, Vol. 6, No. 9, September 1963, pp. 1201-1214; see also "Shock Tube Test Time Limitation Due to Turbulent-Wall Boundary Layer." AIAA Journal, Vol. 2, No. 1, January 1964, pp. 84-92.
26. Norman, W. S. "One-Dimensional MHD Equations for the Non-Ideal Gas, with Application to Singly-Ionizing Argon." AEDC-TR-65-185 (AD 470771), September 1965.
27. Hertzberg, A., Smith, W. E., Glick, H. S., and Squire, W., et al. "Modifications of the Shock Tube for the Generation of Hypersonic Flow." AEDC-TN-55-15, March 1955.
28. Durran, D. A. and Grabousky, W. R. "Development of Hotshot Gas Source for Pulsed MHD Wind Tunnel Study." Sixth Symposium on Engineering Aspects of Magnetohydrodynamics, April 1965.
29. Lau, J. "Electrical Conductivity of Inert Gases-Seed Combination in Shock Tubes." National Research Council of Canada, Mechanical Engineering Report MT-51, N. R. C. No. 7884, December 1963.
30. Boyer, Donald W. "Ionization Nonequilibrium Effects on the Magnetogasdynamical Interaction in the Stagnation Region of an Axisymmetric Blunt Body." ASD-TDR-62-1078, Cornell Aeronautical Laboratory Report No. AG-1547-Y-1, June 1963.
31. Ring, L. E. "Optimization of MHD Crossed-Field Accelerators and Generators." AEDC-TDR-64-278 (AD 456163), January 1965.
32. Norman, Wendell and Chmielewski, Gerald E. "Limit Duplication Lines for Isothermal, Constant Loading Factor, $J \times B$ Accelerators." AEDC-TR-65-37 (AD 457134), February 1965.
33. Mirels, Harold. "Analytical Solution for Constant Enthalpy MHD Accelerator." AIAA Journal, Vol. 2, No. 1, January 1964, p. 145-146.

34. Mirels, Harold, Gold, Richard R., and Mullen, James F. "Minimum-Length MHD Accelerator with Constant Enthalpy and Magnetic Field." AIAA Journal, Vol. 2, No. 6, June 1964, p. 1141-1143.
35. Ring, Leon E. "Status of MHD Accelerators for Test Facilities." 6th Biennial Gas Dynamics Symposium, Northwestern University, August 1965.
36. Harris, C. J., et al. "A High Density Shock Tunnel Augmented by a Faraday MHD Accelerator." Fourth Hypervelocity Techniques Symposium, November 1965.
37. Schreier, Stefan. "On the Use of a $J \times B$ Accelerator to Improve Shock Tunnel Performance." Grumman Research Department Report RE-202, February 1965.
38. DeSanto, D. F. and Burke, A. P. "A Feasibility Study of the Use of a MHD Accelerator Channel in a Shock Tunnel." Cornell Aero. Lab. Report 134, February 1964.
39. Stewart, John L. "Circuit Analysis of Transmission Lines." John Wiley and Sons, Inc., New York, 1958.
40. Furth, H. P., Levine, M. A., and Wanick, R. W. "Production and Use of High Transient Magnetic Fields, II." Review of Scientific Instruments, Vol. 28, No. 11, November 1957, pp. 949-958.
41. Furth, H. P. "Transient Field Magnets and Energy Supplies." Proceedings of the International Conference on High Magnetic Fields, High Magnetic Fields, M. I. T. Press, Chapter 22, pp. 235-248.
42. Kapitza, P. "Further Developments of the Method of Obtaining Strong Magnetic Fields." Proc. Royal Soc. A., 115, 1927, pp. 658-683.
43. Fowler, C. M. et al. "Flux Concentration by Implosion." High Magnetic Fields, M. I. T. Press, Chapter 25, 1962, pp. 269-276.
44. Stratton, J. A. Electromagnetic Theory. McGraw-Hill, New York, 1941, p. 504.
45. Grover, F. W. Inductance Calculations. Dover Publications, N. Y., 1962.
46. Rose, E. B. and Grover, F. U. Report No. 169, National Bureau of Standards, Washington, D. C., 1916.

47. Terman, F. E. Radio Engineers Handbook. McGraw-Hill, N. Y., 1943.
48. Kunzler, J. E. "Superconductivity in High Magnetic Fields at High Current Densities." High Magnetic Fields, M. I. T. Press, Chapter 68, 1962, pp. 574-577.
49. Wiederhold, Peter, Magnion, Inc., Burlington, Massachusetts, Private Communication, June 1964.
50. Mawardi, O. K. "Flux Concentration by Hydromagnetic Flows." High Magnetic Fields, M. I. T. Press, Chapter 24, 1962, pp. 259-268.
51. Waugh, A. F. "Optimization of D-C Coil Design with Respect to Fabrication Cost and Cost of Installed D-C Power." ORNL-2745, October 1950.
52. de Klerk, D. and Corder, C. J. "An Efficiency Criterion for Iron-Core Electromagnets." High Magnetic Fields, M. I. T. Press, Chapter 17, 1962, pp. 194-201.
53. Laquer, H. L. "The Cryogenic Magnet Program at Los Alamos." High Magnetic Fields, M. I. T. Press, Chapter 13, 1962, pp. 156-165.
54. Gaum, F. I. Rech. Scient., 9, 243, 287; 1957.
55. Kunzler, J. E. "Superconductivity in High Magnetic Fields at High Current Densities." Rev. Modern Physics, Vol. 33, p. 501-509, 1961.
56. Giauque, W. F. and Lyon, D. N. "Design of a 100-kilogauss 4-inch Core Solenoid for Continuous Operation." Rev. Scient. Instrum., Vol. 31, p. 374-390, 1960.
57. Lawrence, J. C. and Brown, G. V. "A Large Liquid Non-Cooled Electromagnet." High Magnetic Fields, M. I. T. Press, Chapter 15, 1962, pp. 170-179.
58. Maeda, Sejiro. "High Field Research at Tohoku University." High Magnetic Fields, M. I. T. Press, Chapter 46, 1962, pp. 406-411.
59. Kolm, H. "Recent Advances in the Design of High-Field dc Solenoid Magnets." J. Applied Physics, Vol. 29, 1958, p. 489-491.
60. Bitter, F. "Water-Cooled Magnets." High Magnetic Fields, M. I. T. Press, Chapter 8, 1962, pp. 85-100.

61. De Blois, R. W. "Miniature Coils for High Magnetic Field Research." Rev. Scient. Instrum., Vol. 32, 1961, p. 816-818.
62. Morpugo, M., et al. CERN Scient. Report No. 27, 1960.
63. Karasik, V. R. "Strong Magnetic Fields." Instr. Exper. Techniques, USA, No. 6, November 1962, pp. 1075-1086 (Published July 1963).
64. Foner, S. and Kolm, H. "Coils for the Production of High-Intensity Pulsed Magnetic Fields." Rev. Scient. Instrum., Vol. 28, p. 799-807, 1957.
65. van der Sluijs. "Hydrogen-Cooled Pulsed Magnets." High Magnetic Fields, M. I. T. Press, Chapter 29, 1962, pp. 290-291.
66. Bergmann, H., et al. "Pulsed Bubble Chamber." High Magnetic Fields, M. I. T. Press, Chapter 30, 1962, pp. 292-295.
67. Skellett, S. "Design of 100-KC Pulsed Coils for Phoenix Mirror Machine." High Magnetic Fields, M. I. T. Press, Chapter 31, 1962, pp. 296-306.
68. Boom, R. W. and Livingston, R. S. "Superconducting Solenoids." Proceedings of IRE, Vol. 50, No. 1, January 1962, pp. 274-285.
69. Bitter, F. Review of Scientific Instruments, Part I, Vol. 7, p. 479; Part II, Vol. 7, p. 482; Part III, Vol. 8, p. 318; Part IV, Vol. 10, p. 373; 1936-39.
70. Montgomery, D. B. "The Generation of High Magnetic Fields." Reports on Progress in Physics, Vol. 26, 1963, pp. 69-104.
71. Ball, Henry W. "Calibration of the 100-Inch Hypervelocity Tunnel (F)." AEDC-TDR-63-46 (AD 298279), March 1963.
72. Boyer, D. W., Eschenroeder, A. Q. and Russo, A. L. "Approximate Solutions for Nonequilibrium Airflow in Hypersonic Nozzles." Cornell Aeronautical Laboratory Report No. AB-1345-W-3. Also AEDC-TN-60-181 (AD 246226), August 1960.
73. Brown, G. V., et al. "Axial and Radial Magnetic Fields of Thick, Finite Length Solenoids." NASA Technical Report R-170, 1963.

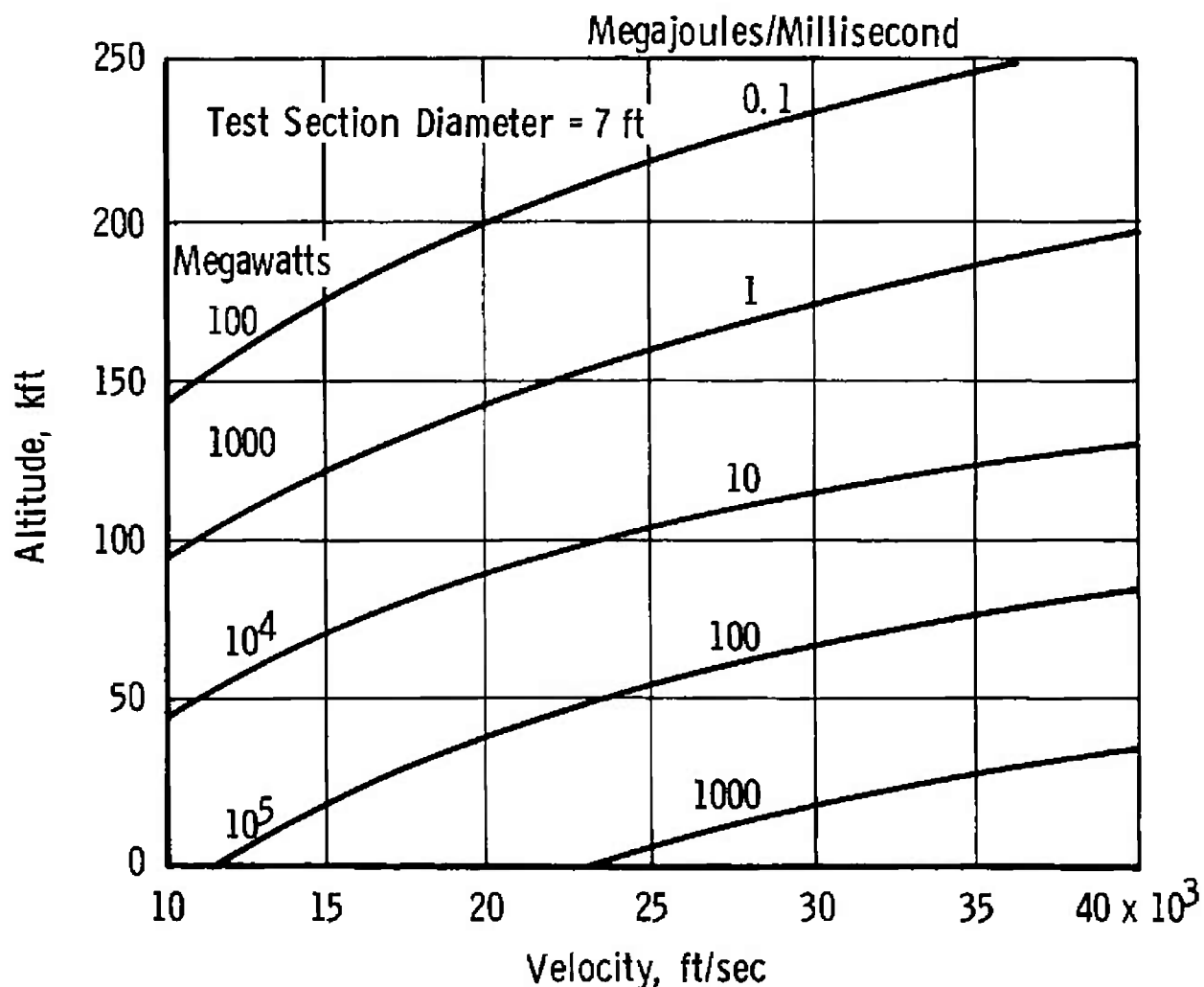


Fig. 1 Test Section Flow Energy

Test Section Velocity = 30,000 ft/sec

Density Altitude = 200,000 ft

Turbulent Boundary Layer

Nozzle Half-Angle = 5 deg

$\delta^* = 26^*$

(Based upon empirical results obtained for lower velocities)

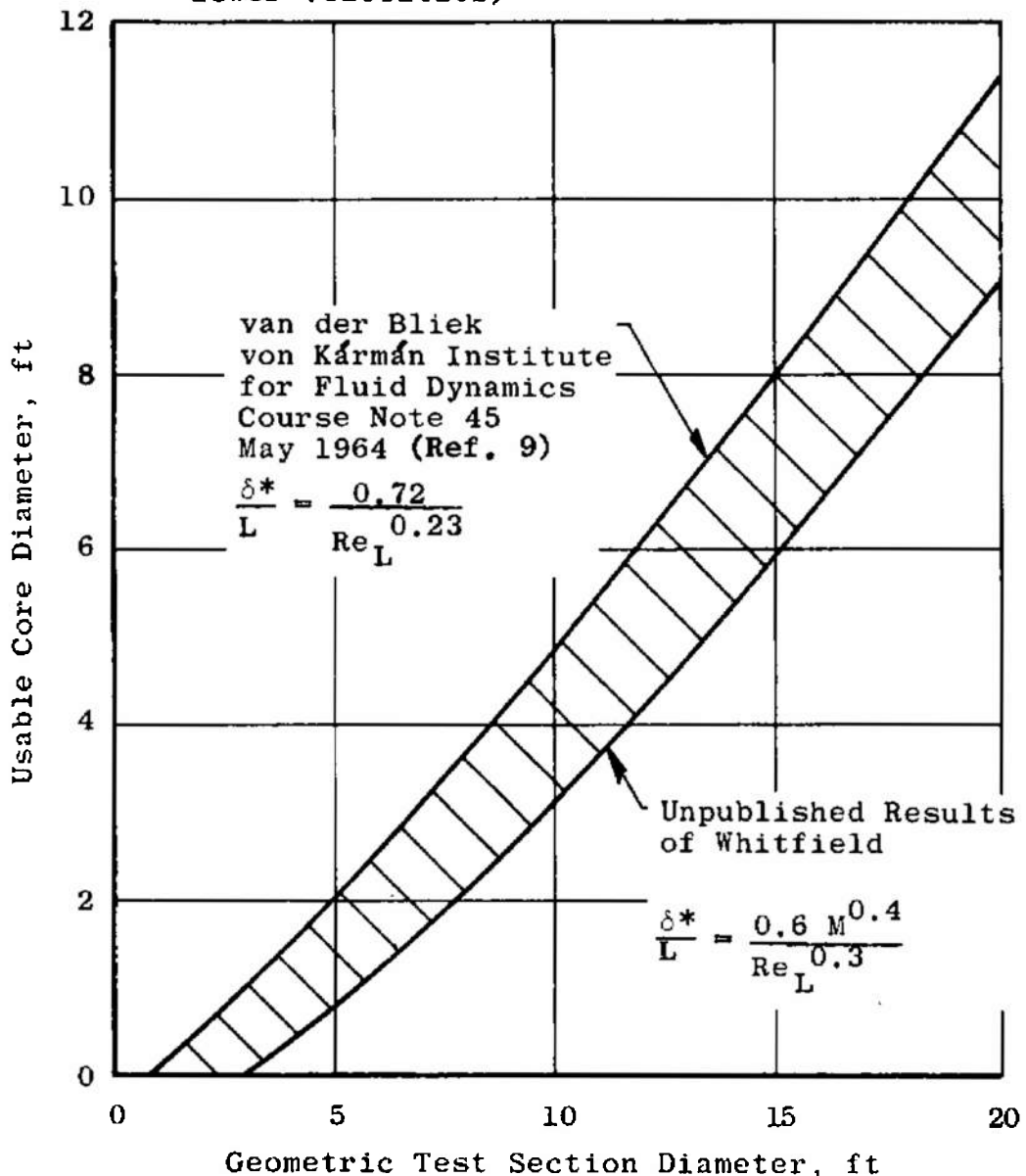


Fig. 2 Estimate of Usable Core Section Diameter

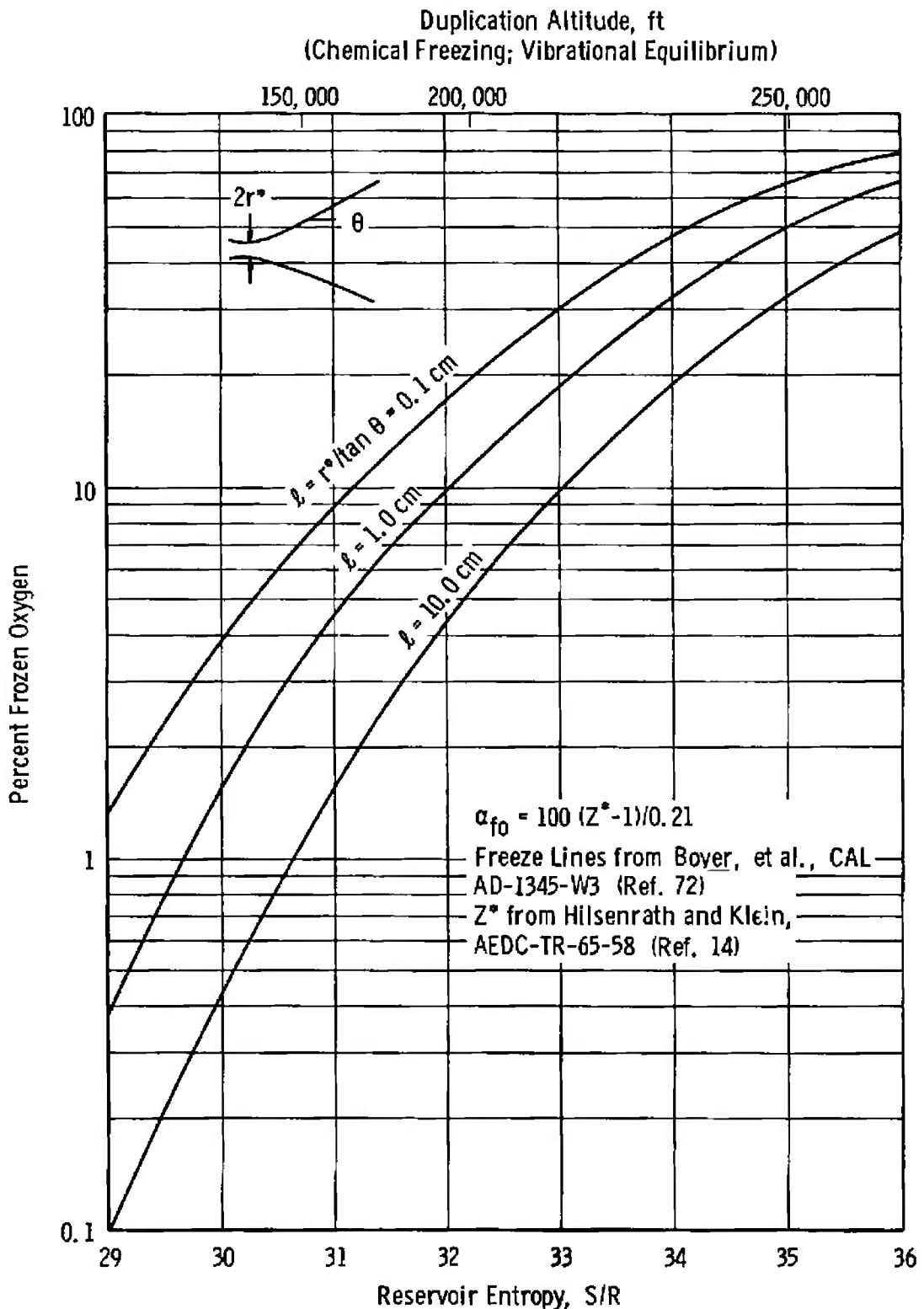


Fig. 3 Percent Frozen Oxygen after Isentropic Expansion across Freeze Line

1962 U. S. Standard Atmosphere (Ref. 13)
Air Data: Humphrey and Neel
(AEDC-TN-61-103, Ref. 15)

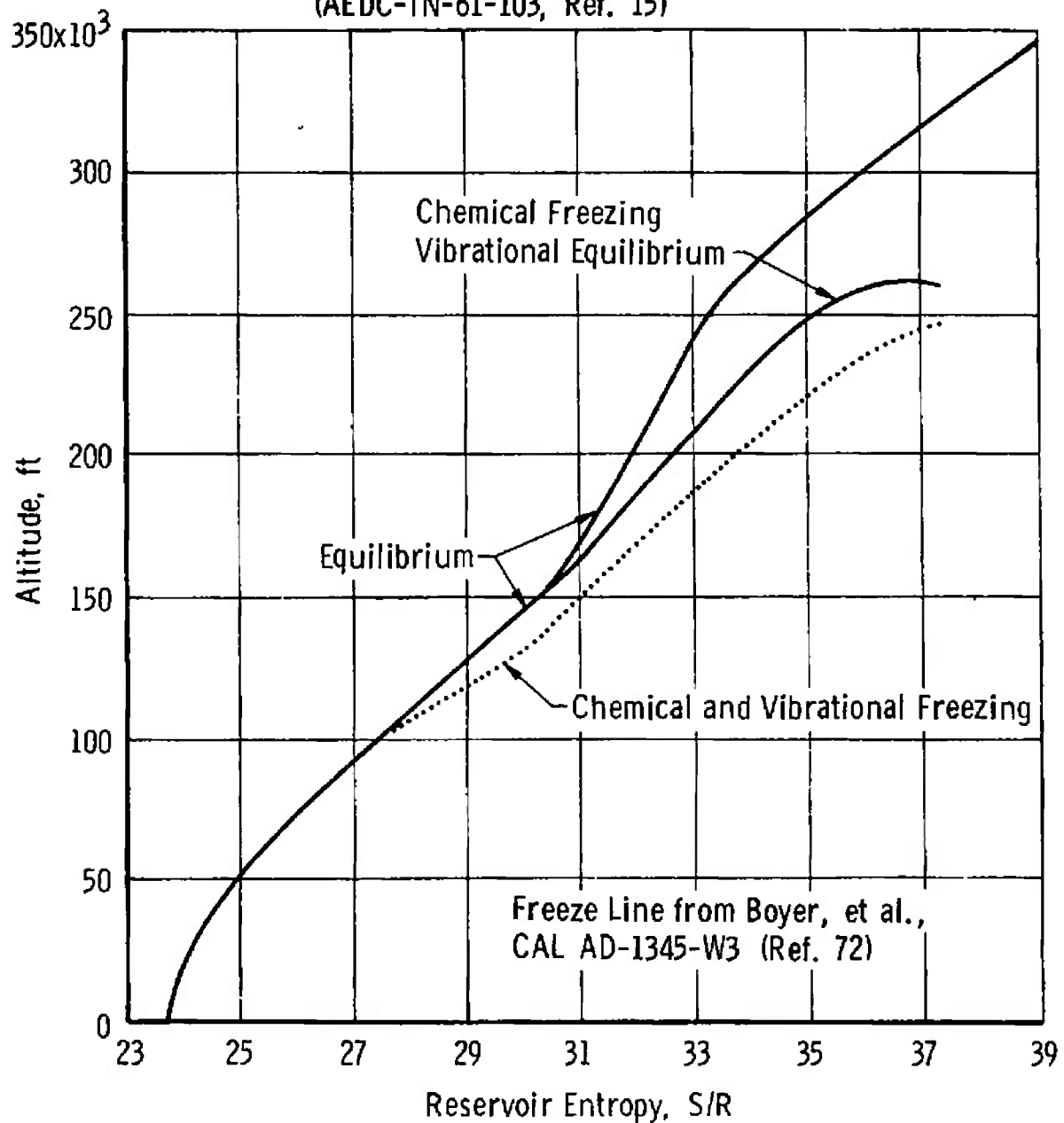


Fig. 4 Altitude for Density and Frozen Speed of Sound Matching

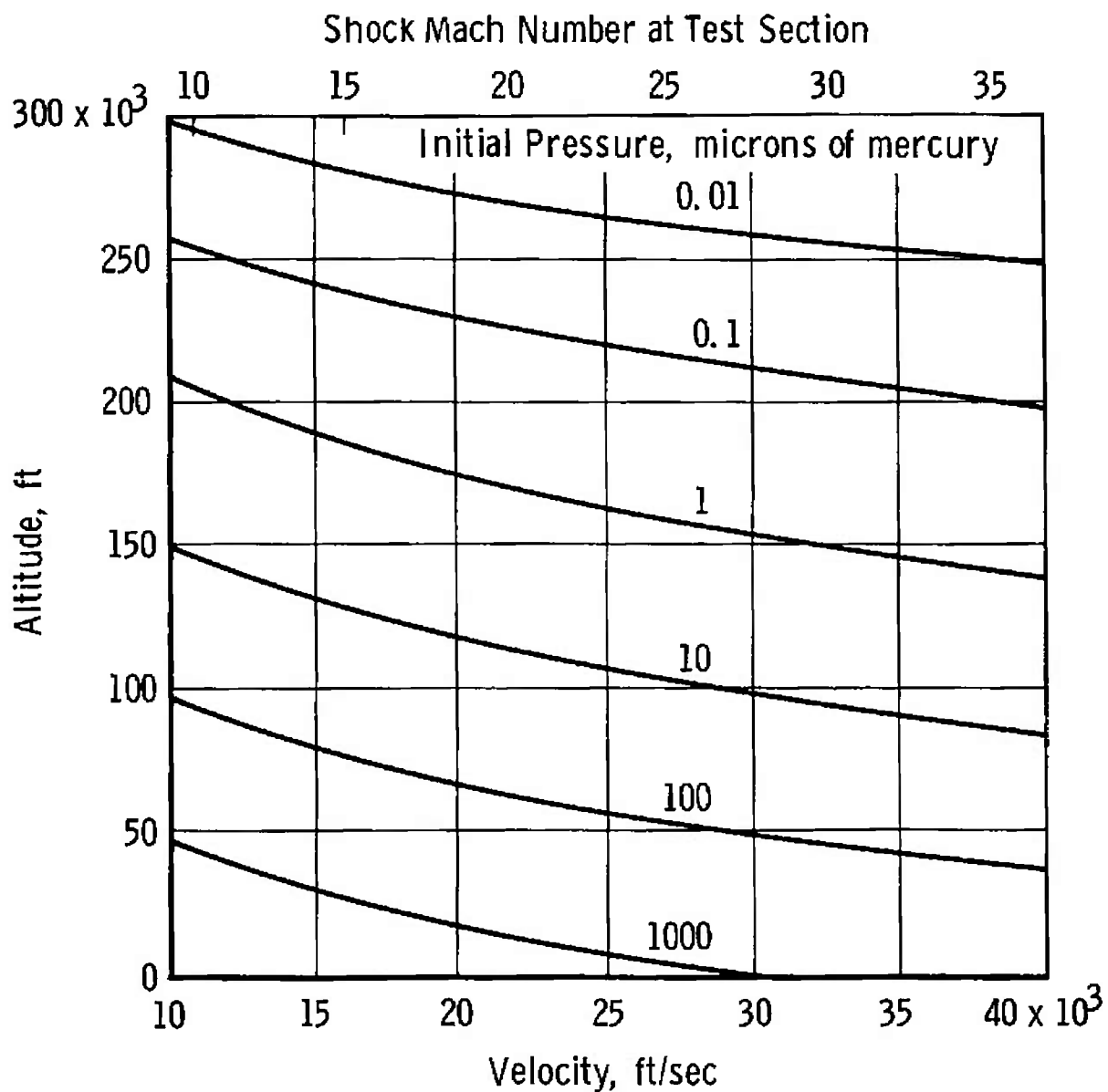


Fig. 5 - Initial Pressure Required in Test Section for Perfect Start of Nozzle

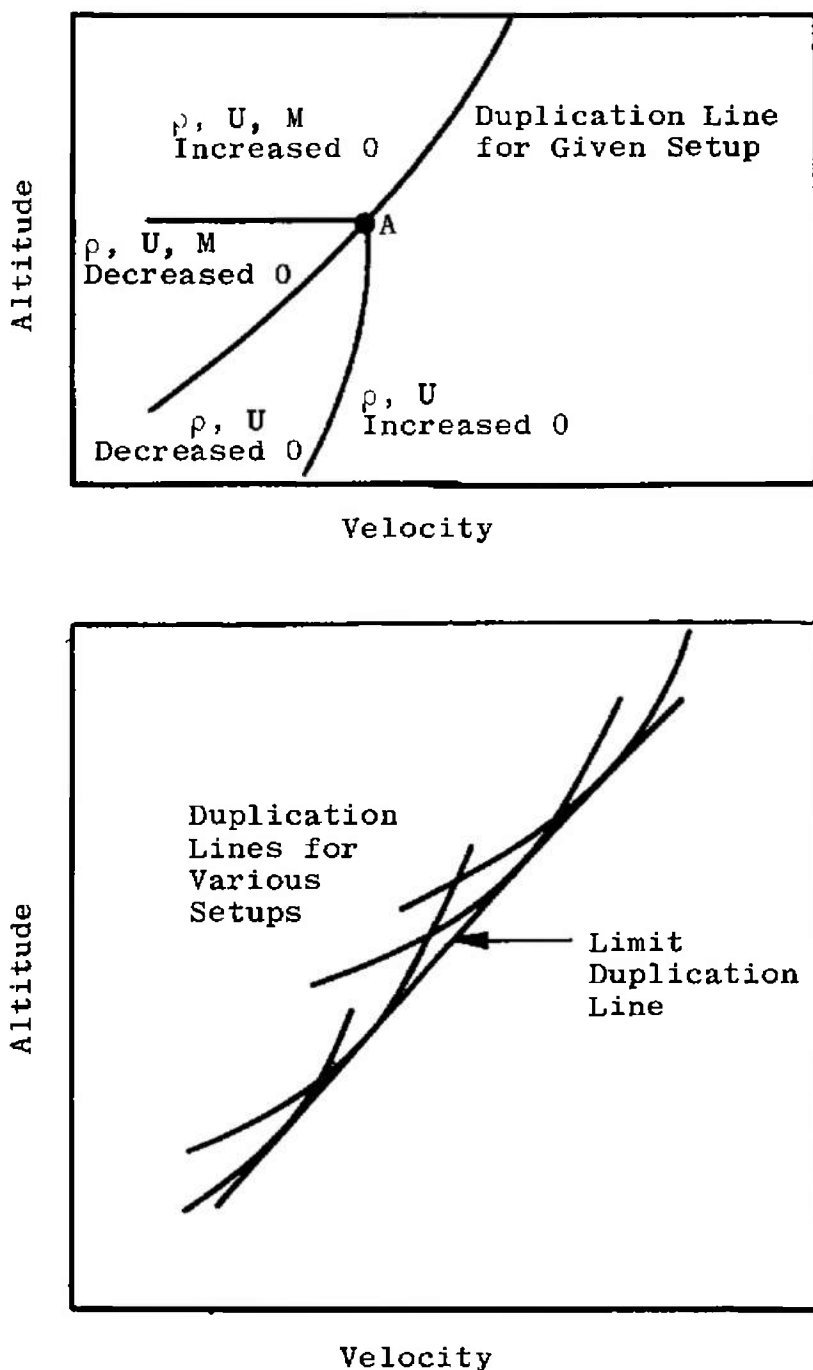


Fig. 6 Illustration of Duplication Lines

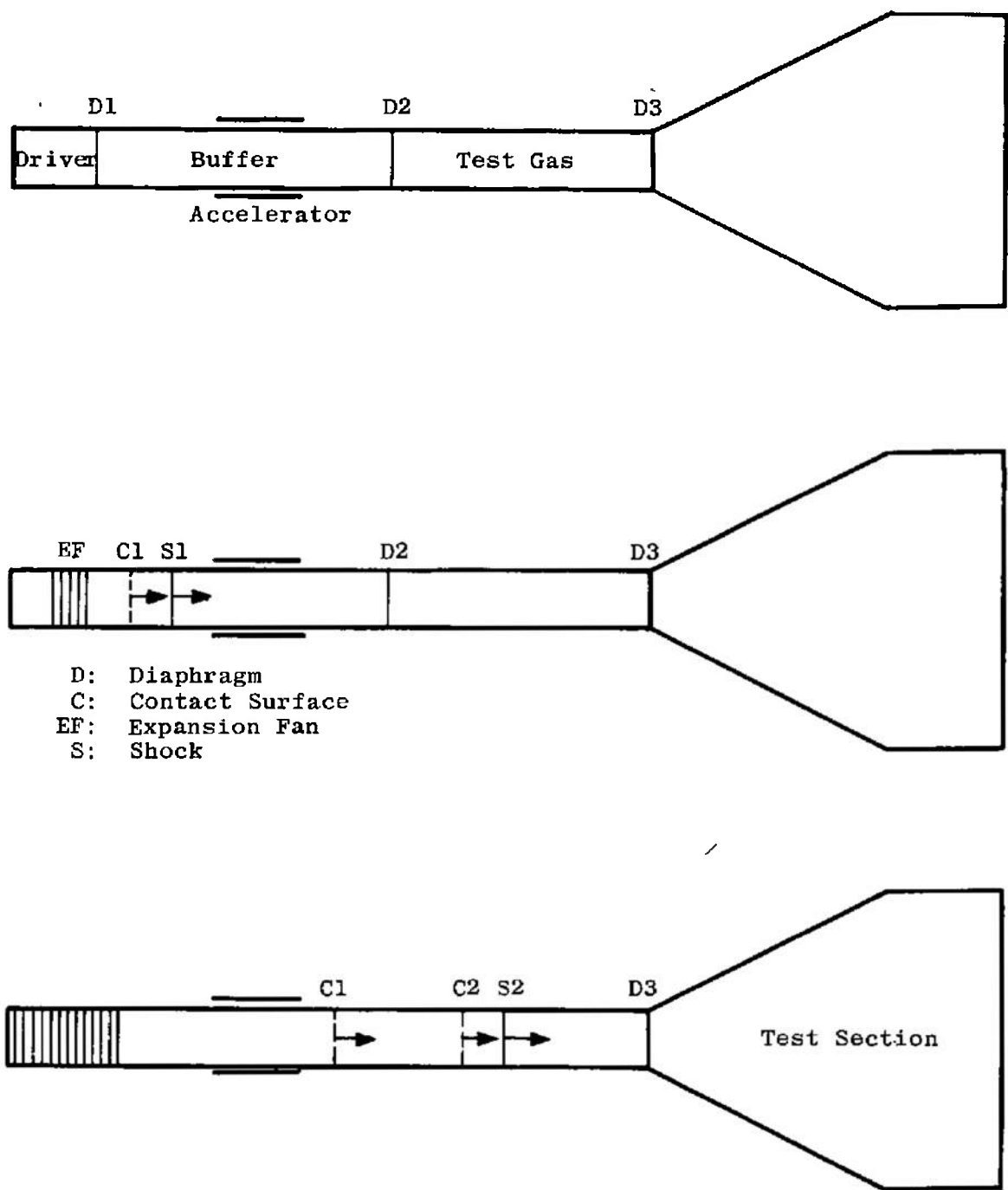


Fig. 7 Schematic of Operation of Shock Tunnel with a Buffer Accelerator

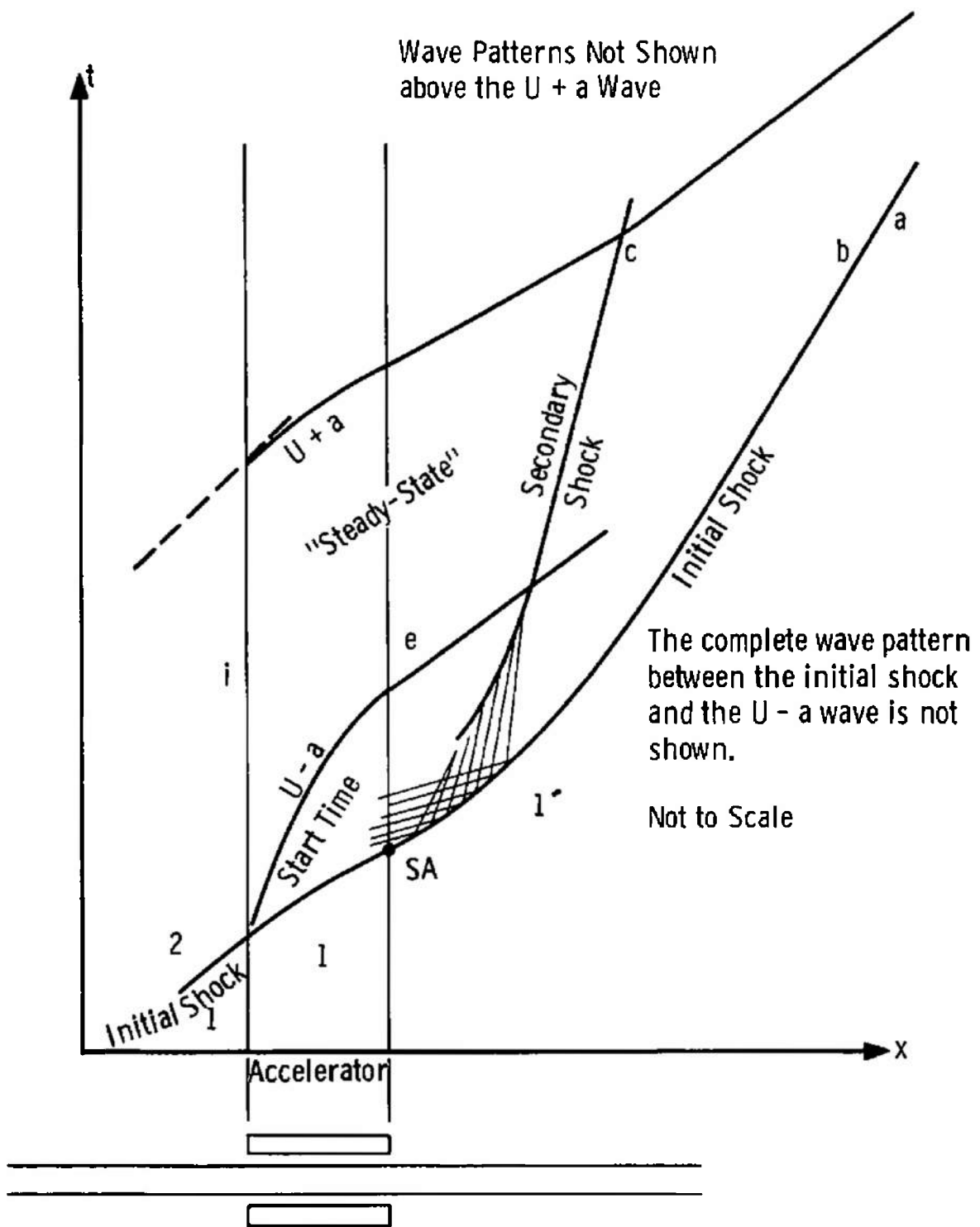


Fig. 8 Schematic of Accelerator Processes in x-t Plane

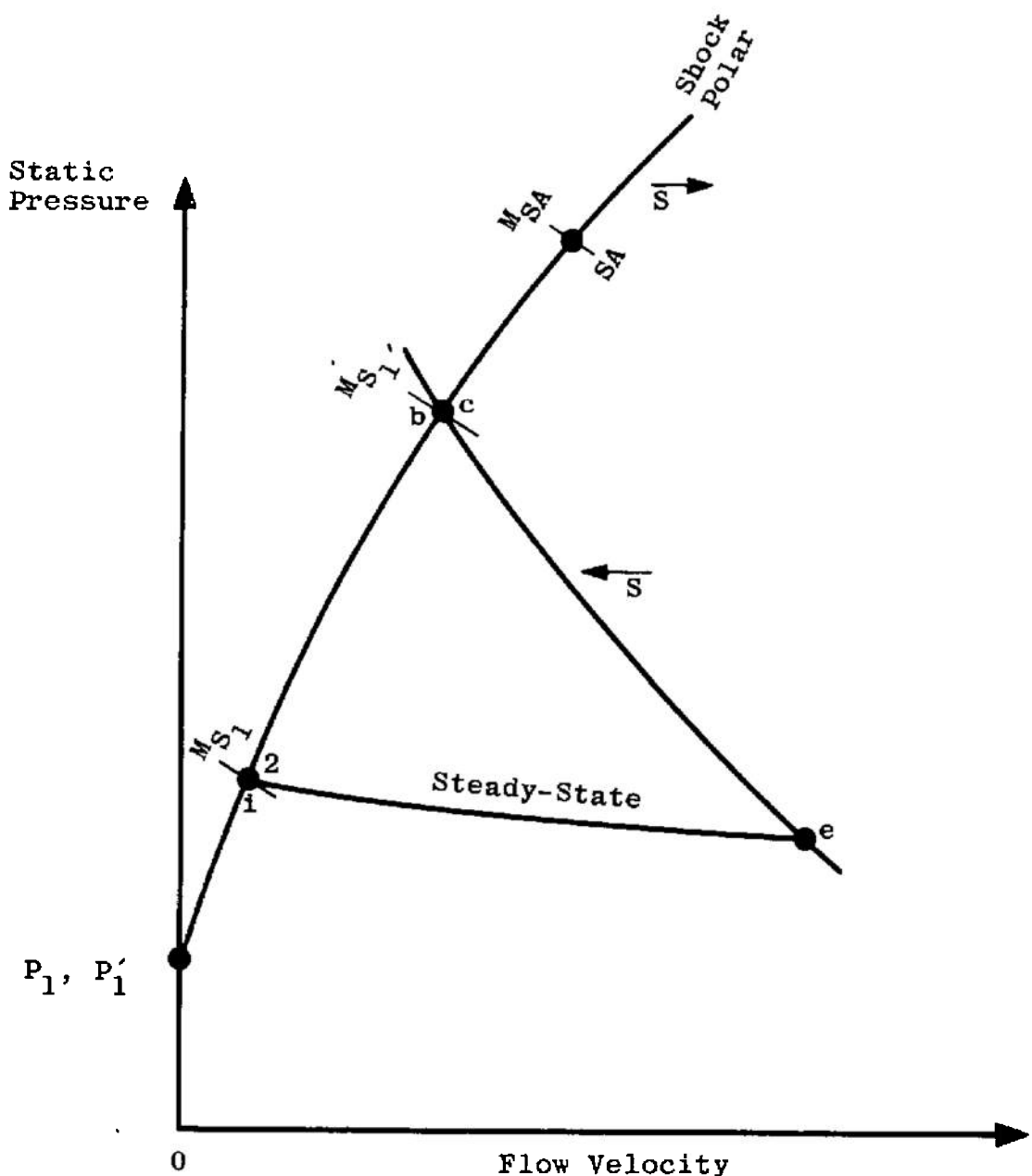


Fig. 9 Schematic of Accelerator Processes in the Pressure-Velocity Plane

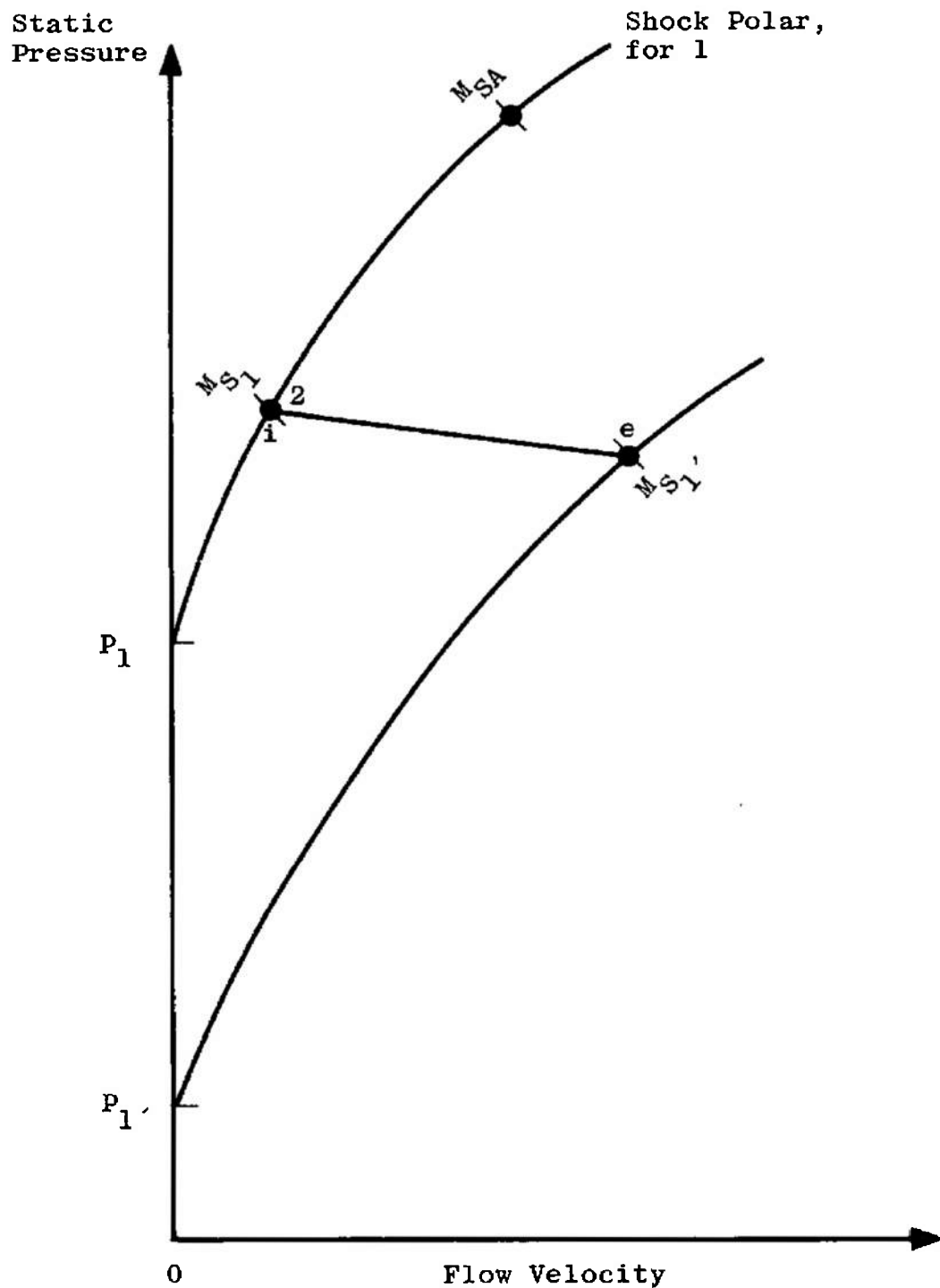


Fig. 10 Processes for Reduced Pressure at Accelerator Exit

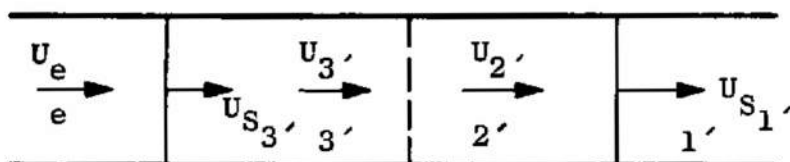
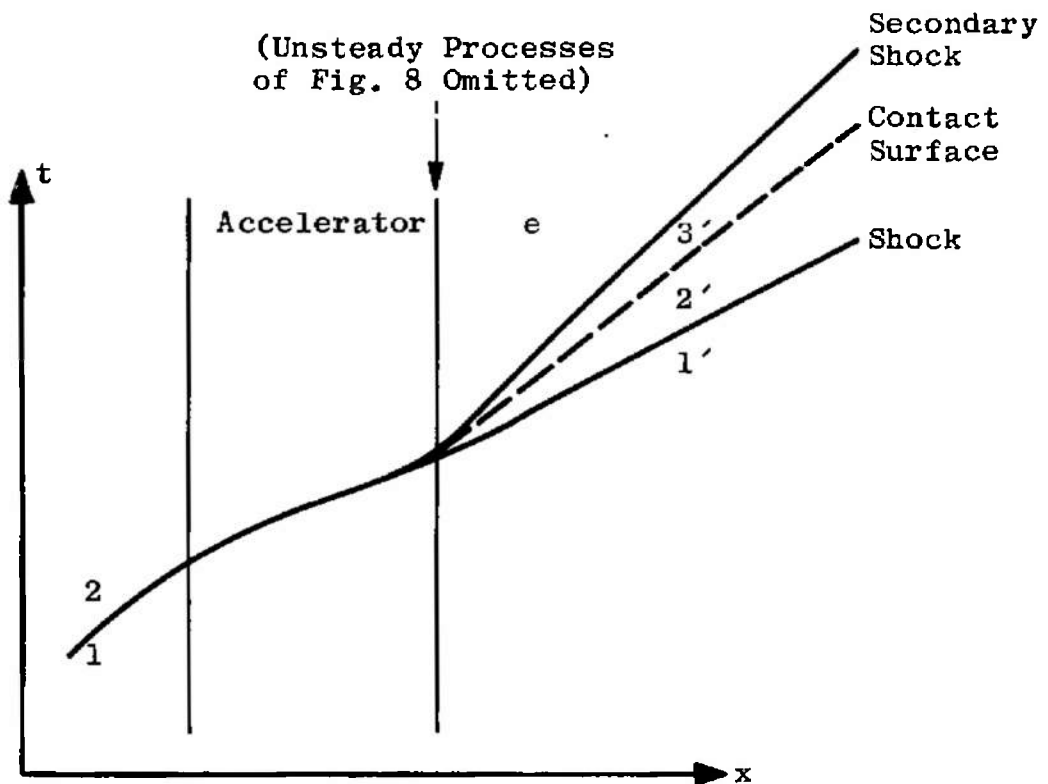


Fig. 11 Nomenclature for Downstream Processes

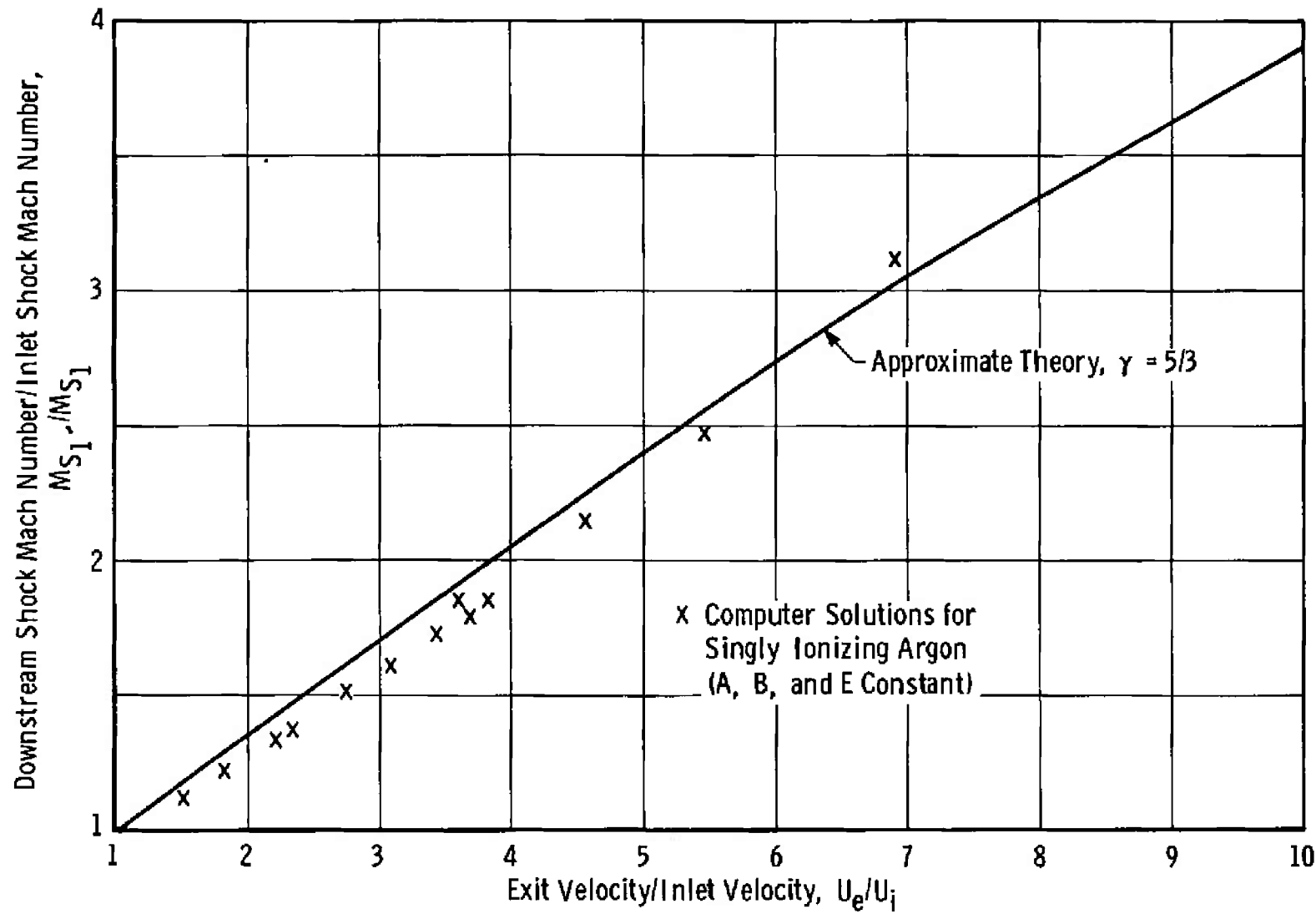


Fig. 12 Shock Speed Ratio across MHD Buffer Accelerator

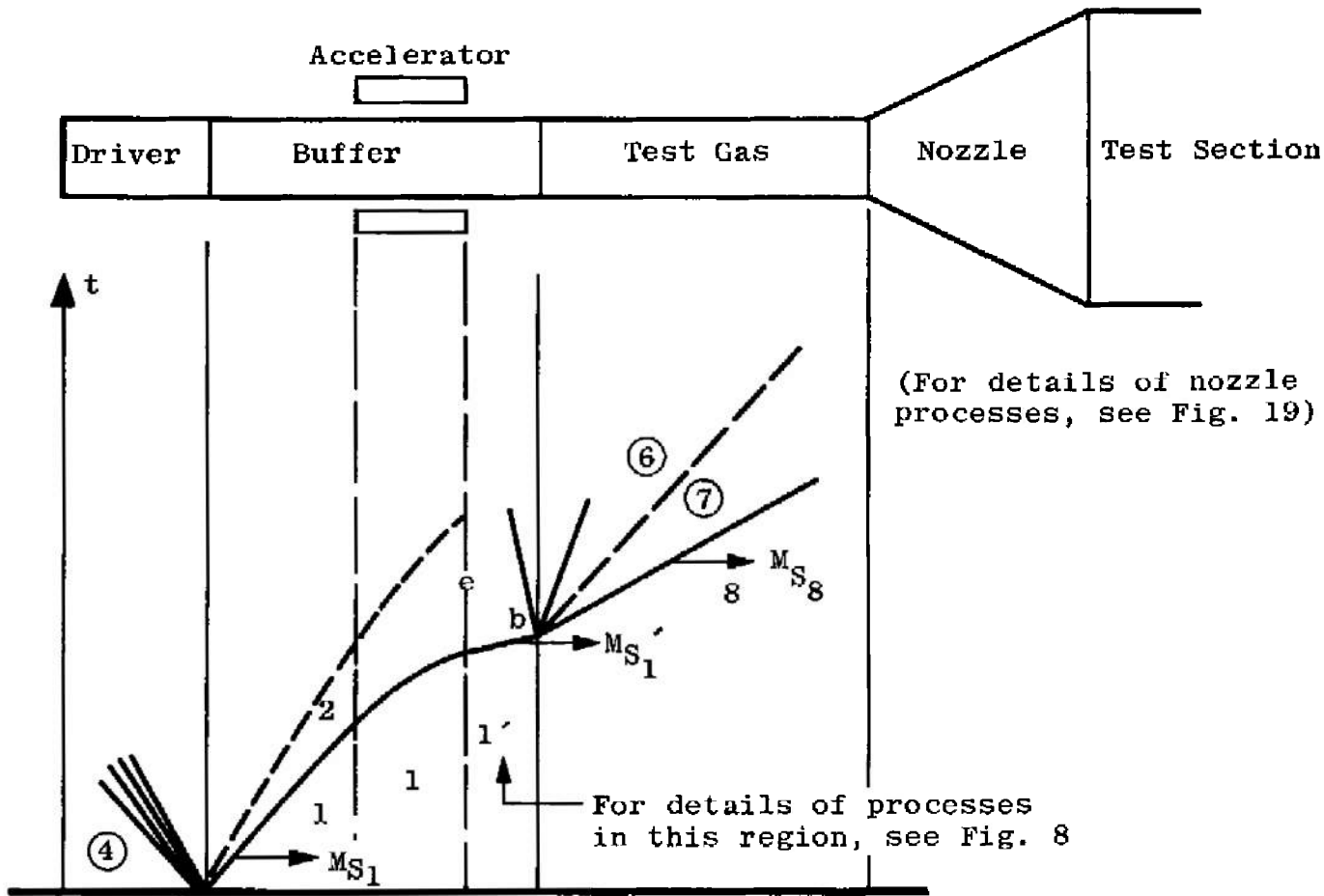
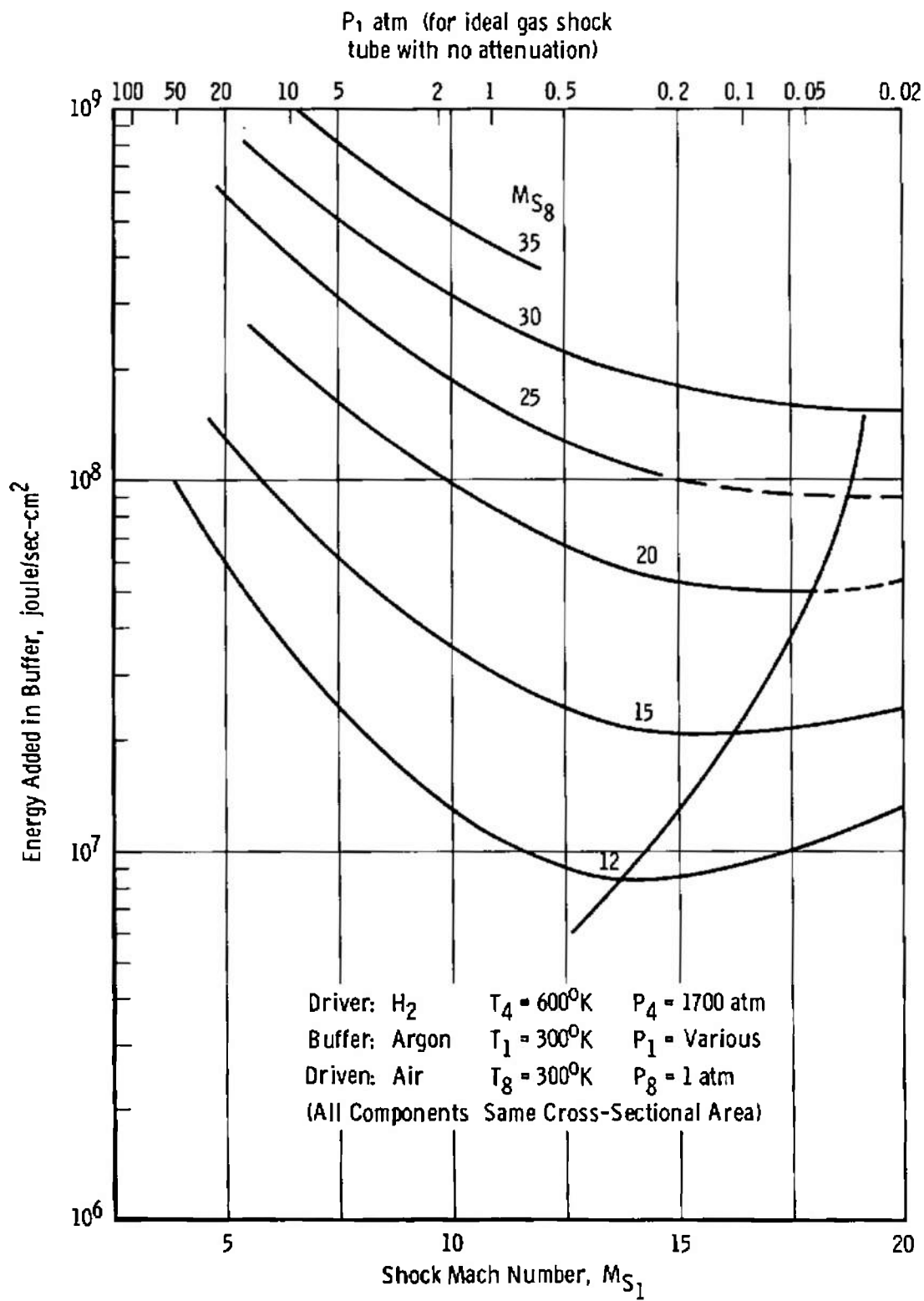


Fig. 13 Schematic and Wave Diagram for MHD Buffer Accelerator Shock Tunnel

Fig. 14 Energy for Argon Buffer $P_8 = 1 \text{ atm}$

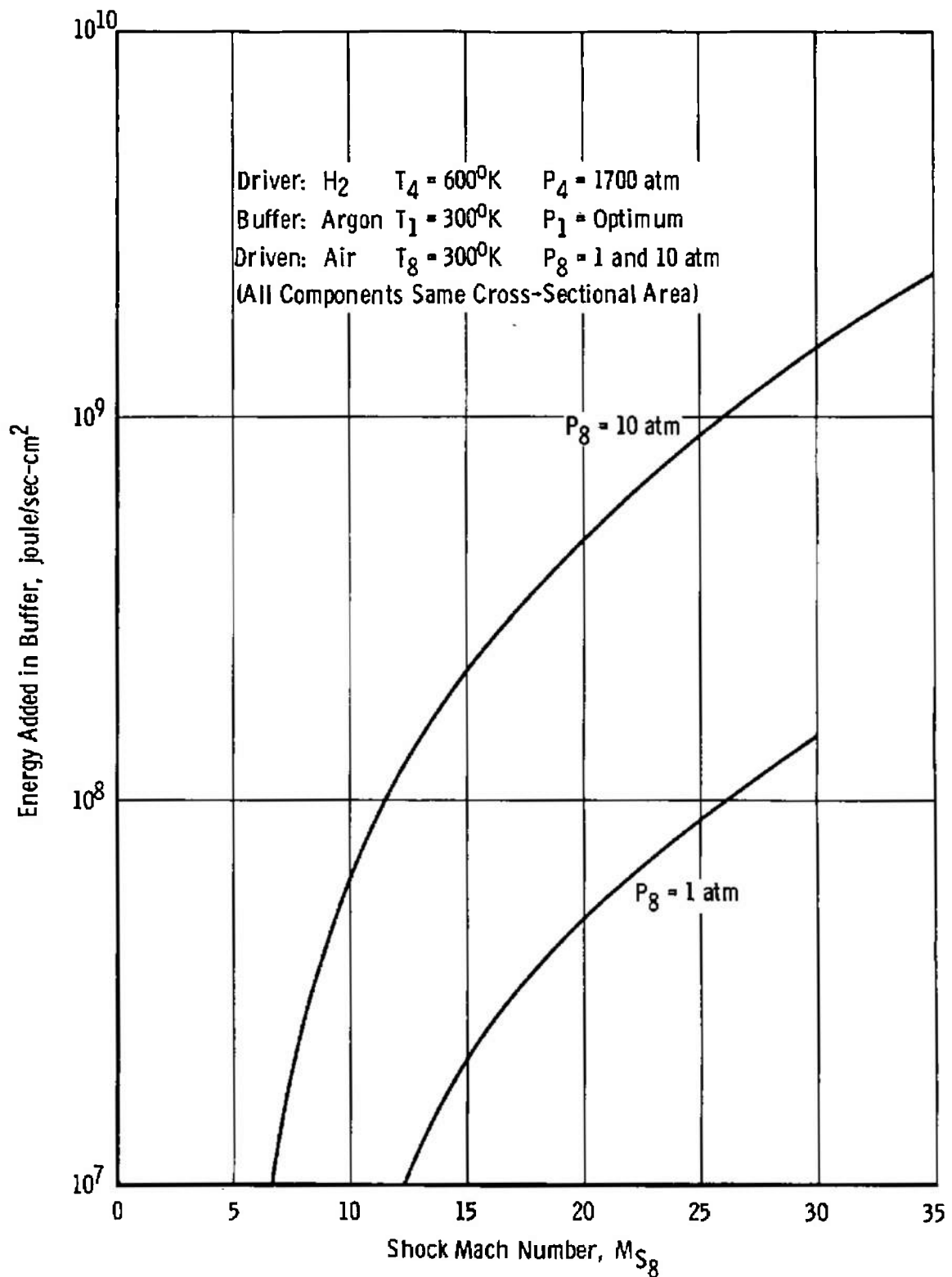


Fig. 15 Minimum Energy Requirements for Argon Buffers

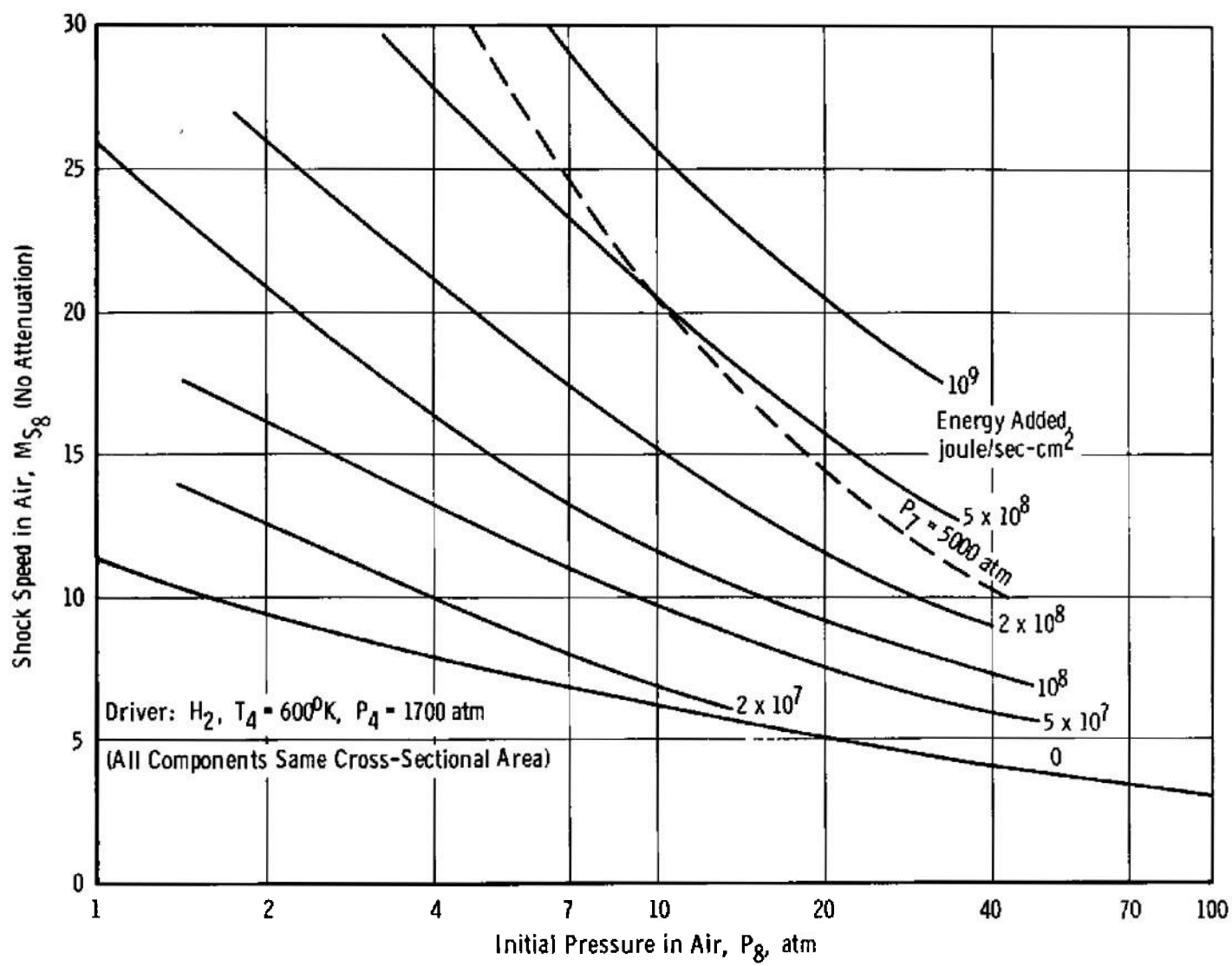


Fig. 16 Summary of Theoretical Shock Tube Performance for Various Energy Additions

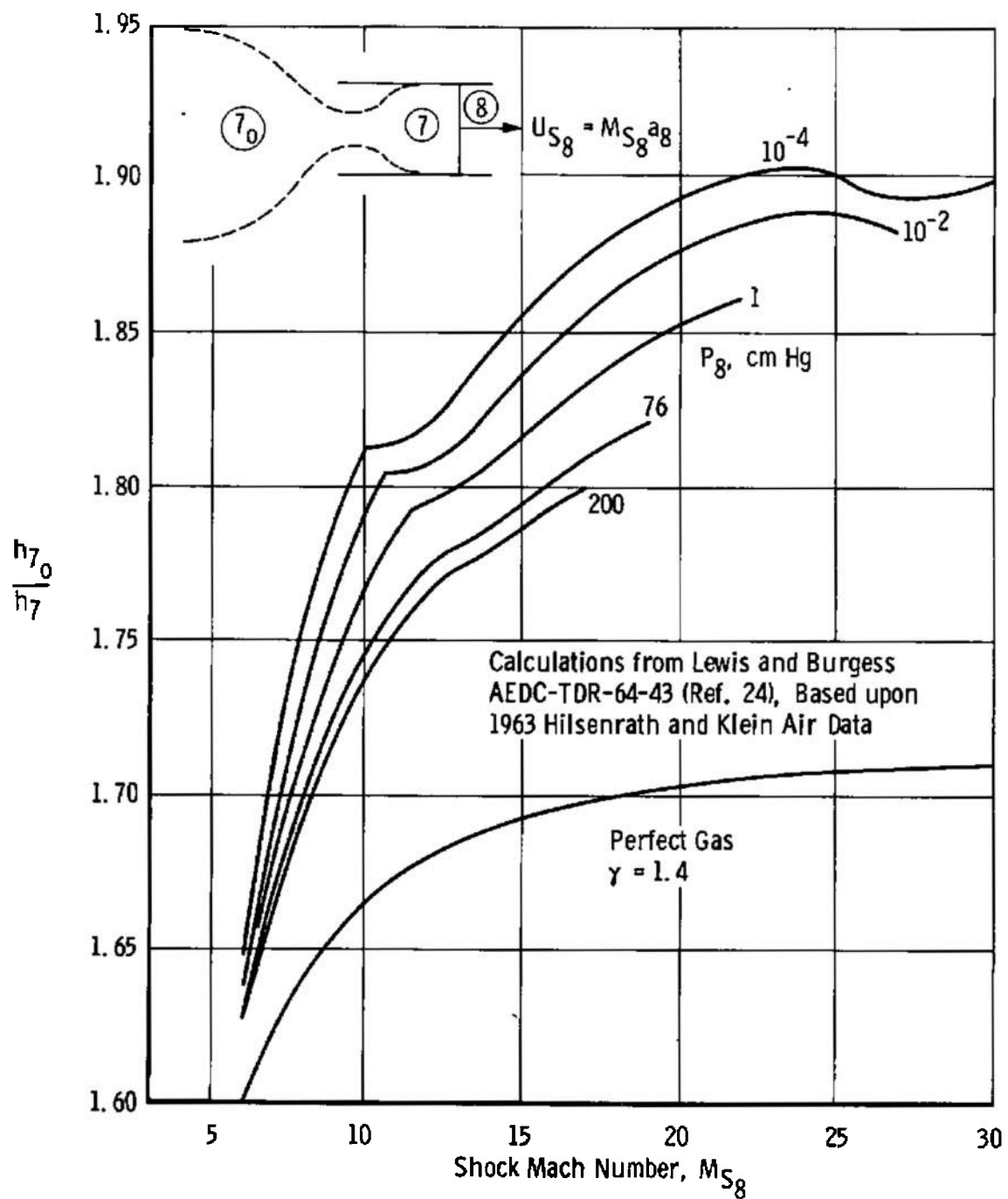


Fig. 17 Ratio of Stagnation Enthalpy to Static Enthalpy behind a Moving Shock in Air

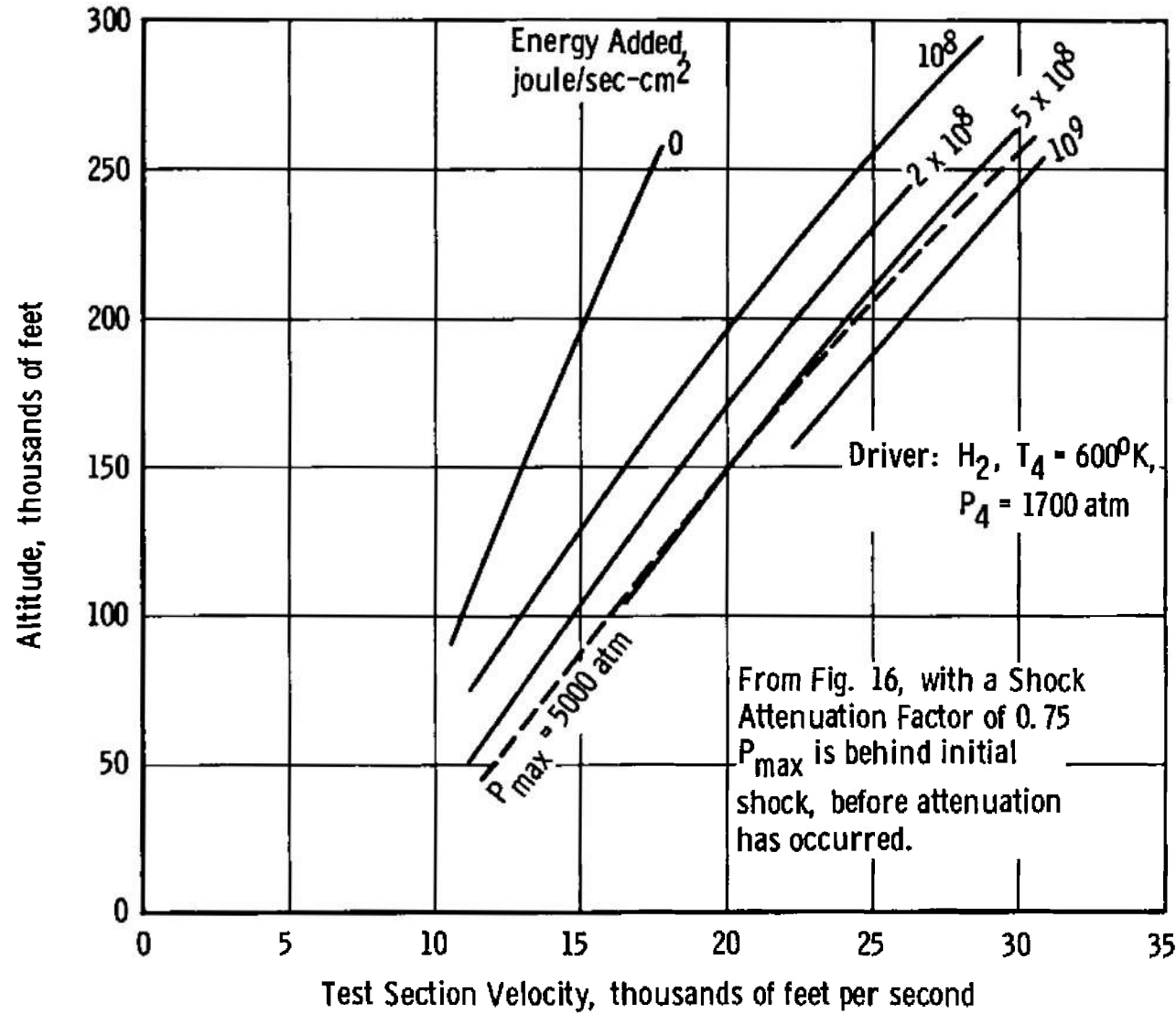


Fig. 18 Duplication Capabilities of MHD Buffer-Augmented Shock Tunnels

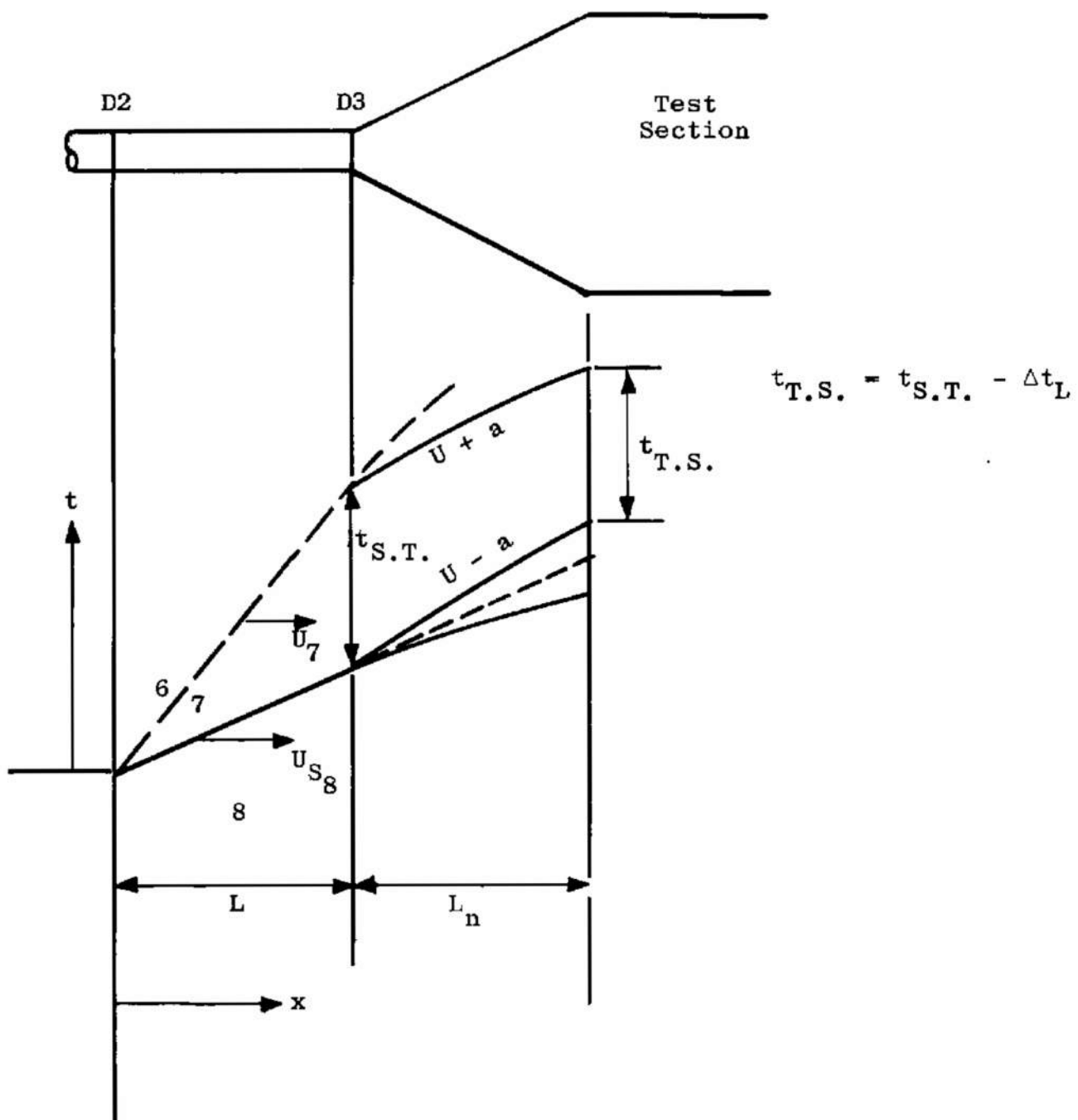


Fig. 19 Nomenclature for Test Time Determination

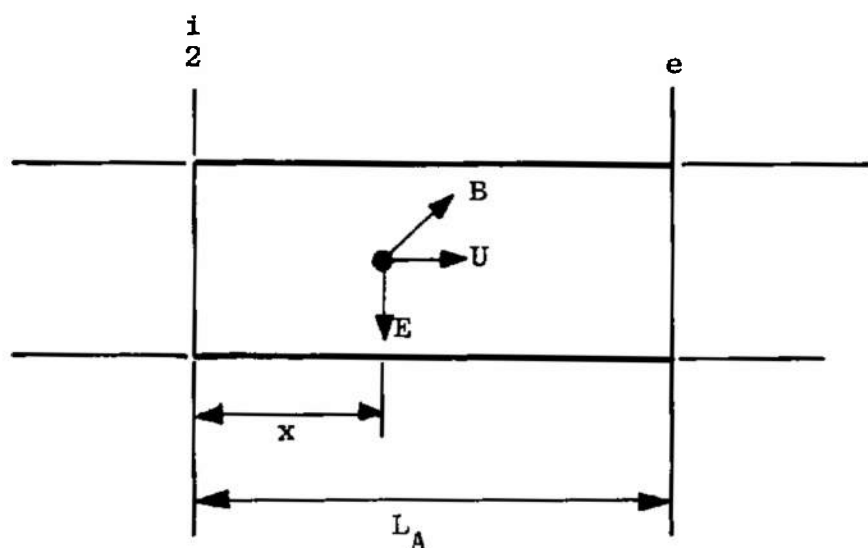


Fig. 20 Illustration of Nomenclature for Buffer Accelerator

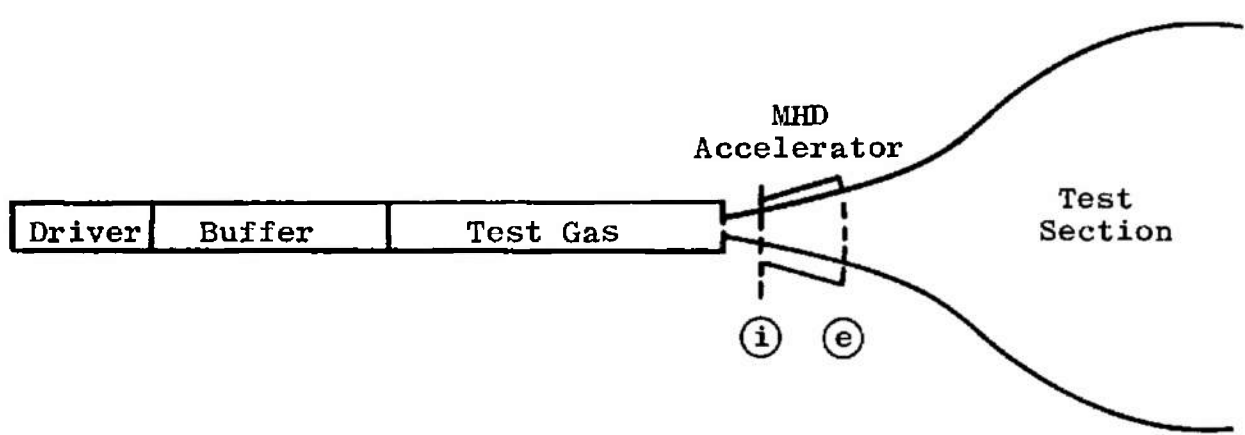
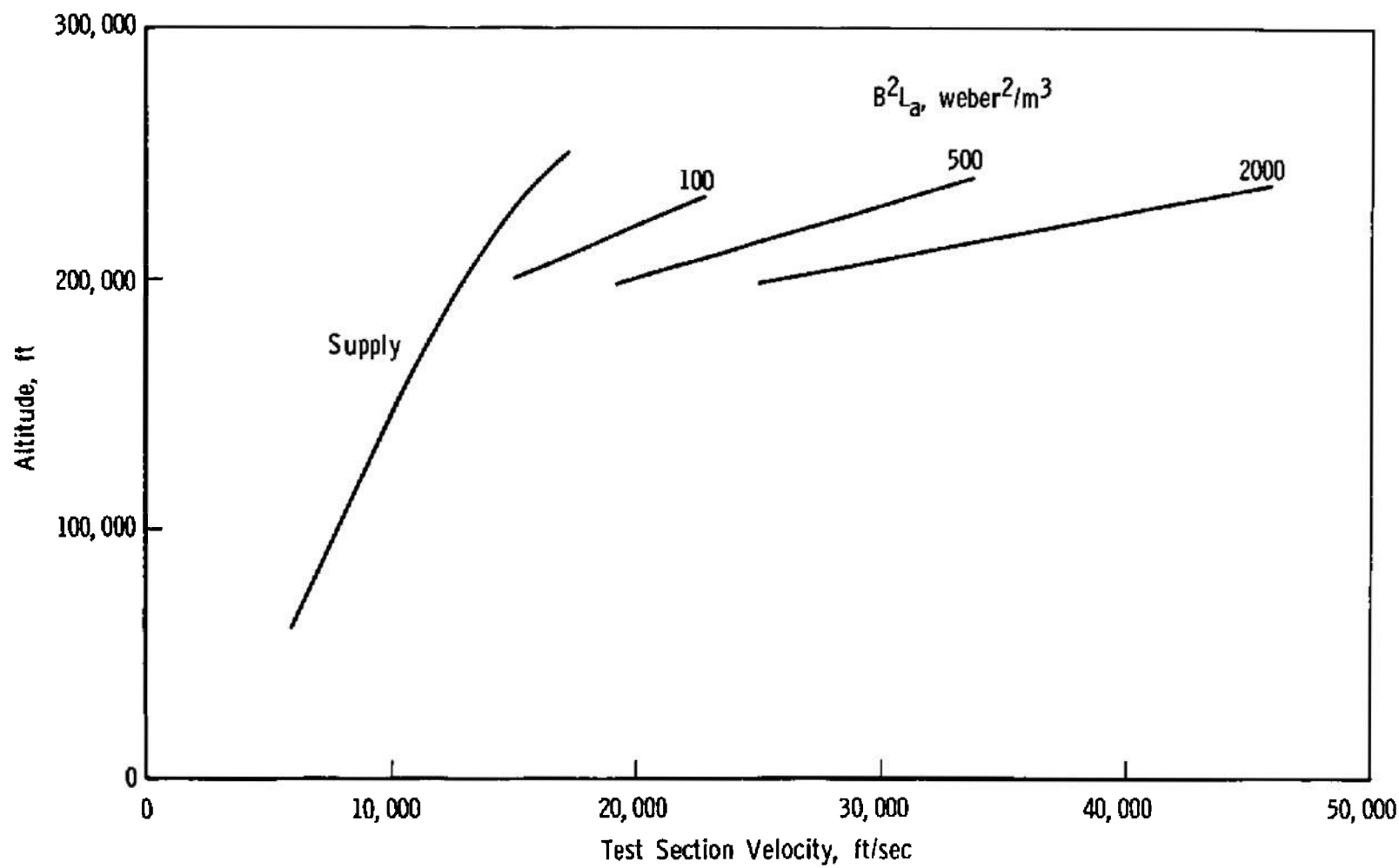
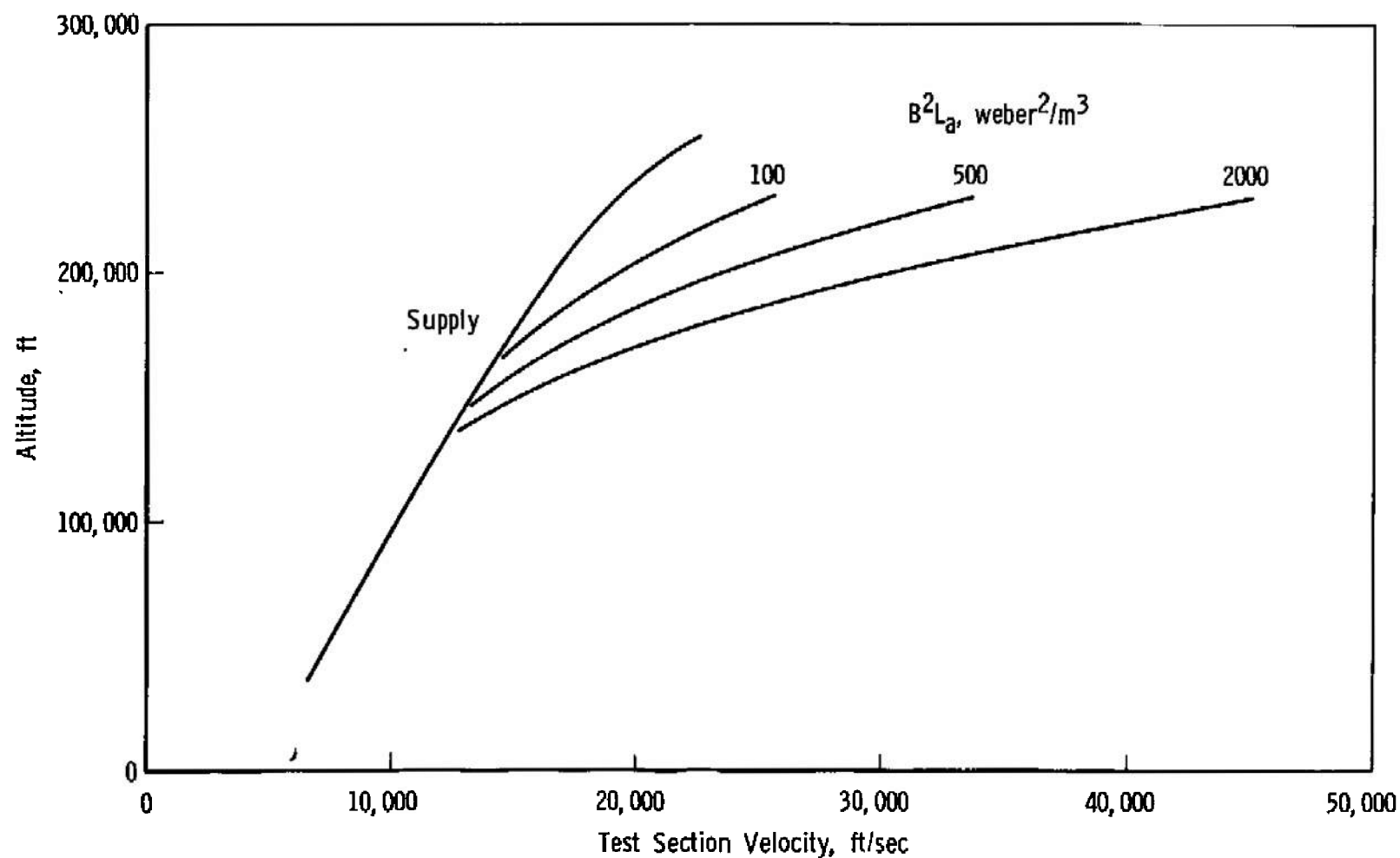


Fig. 21 Nozzle Accelerator Schematic



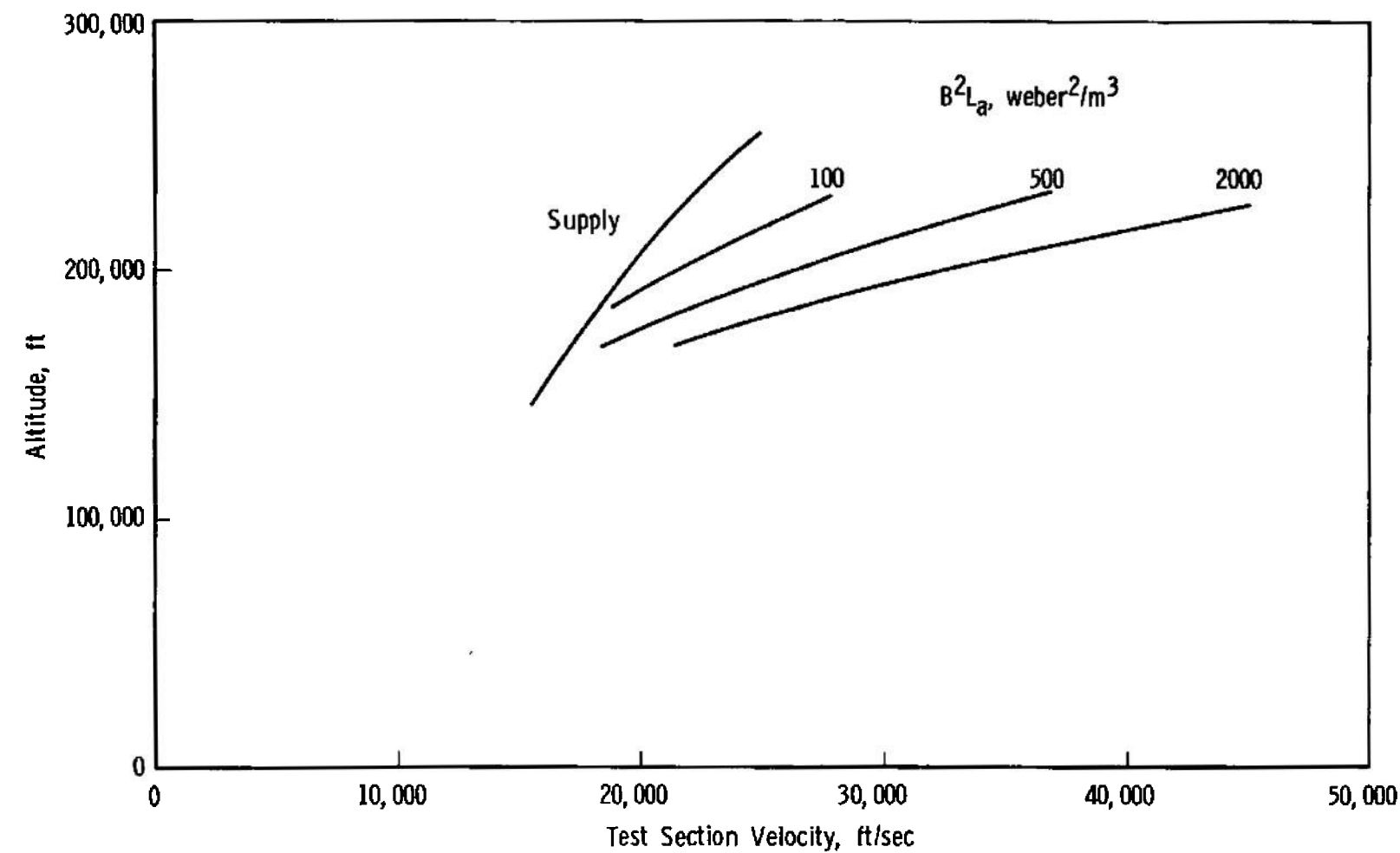
a. Supply Stagnation Pressure: 100 atm

Fig. 22 Limit Duplication Lines, Air with 1/4-percent Potassium Seed



b. Supply Stagnation Pressure: 1000 atm

Fig. 22 Continued



c. Supply Stagnation Pressure: 5000 atm

Fig. 22 Concluded

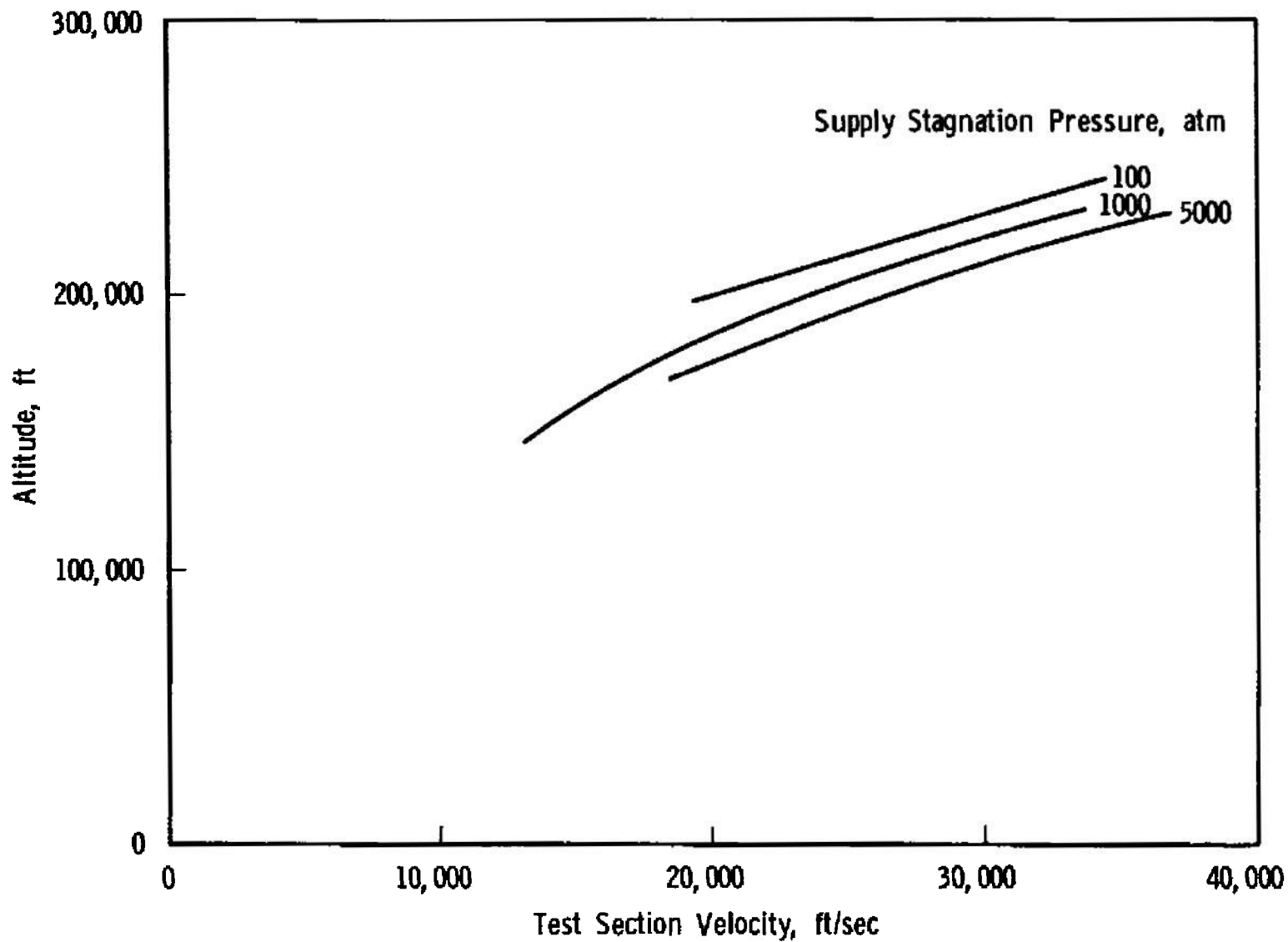
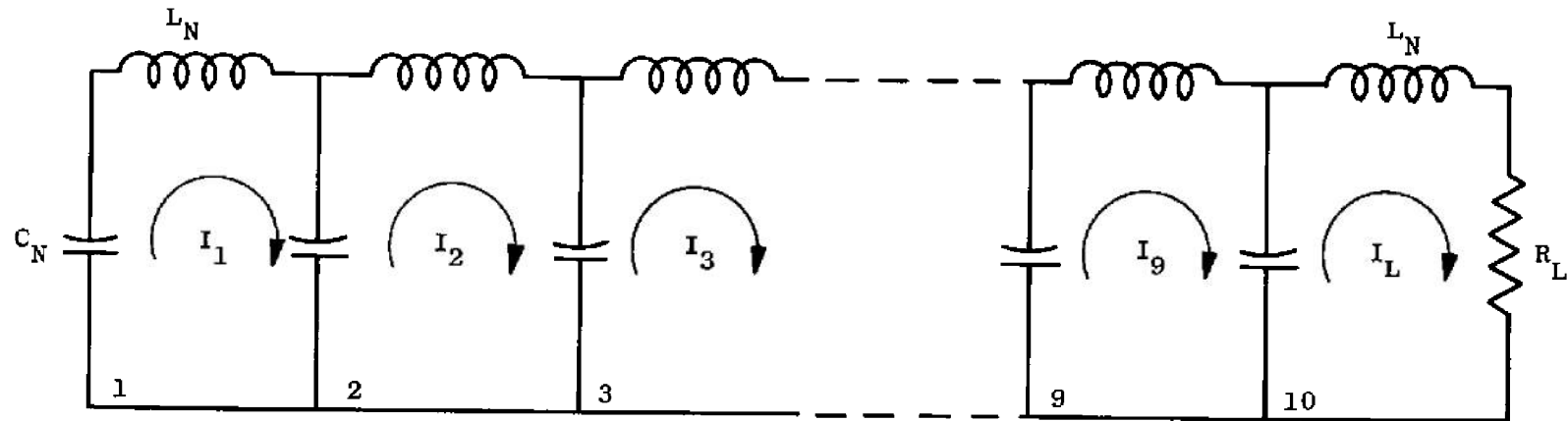


Fig. 23 Limit Duplication Lines, $B^2 L_0 = 500 \text{ weber}^2/\text{meter}^3$, Air with 1/4-percent Potassium Seed



$$L_N = 1.0 \times 10^{-7} \text{ henries}$$

$$C_N = 0.0031 \text{ farad}$$

$$Z_o = 0.00567 \text{ ohm}$$

$$V_o = 8000 \text{ volts}$$

$$R_L = \frac{0.336 \times 10^2}{\sigma l} \text{ ohm} \quad \text{where } \sigma, \text{ mho/m}$$

Fig. 24 Schematic Diagram for a Lossless Transmission Line - Case One

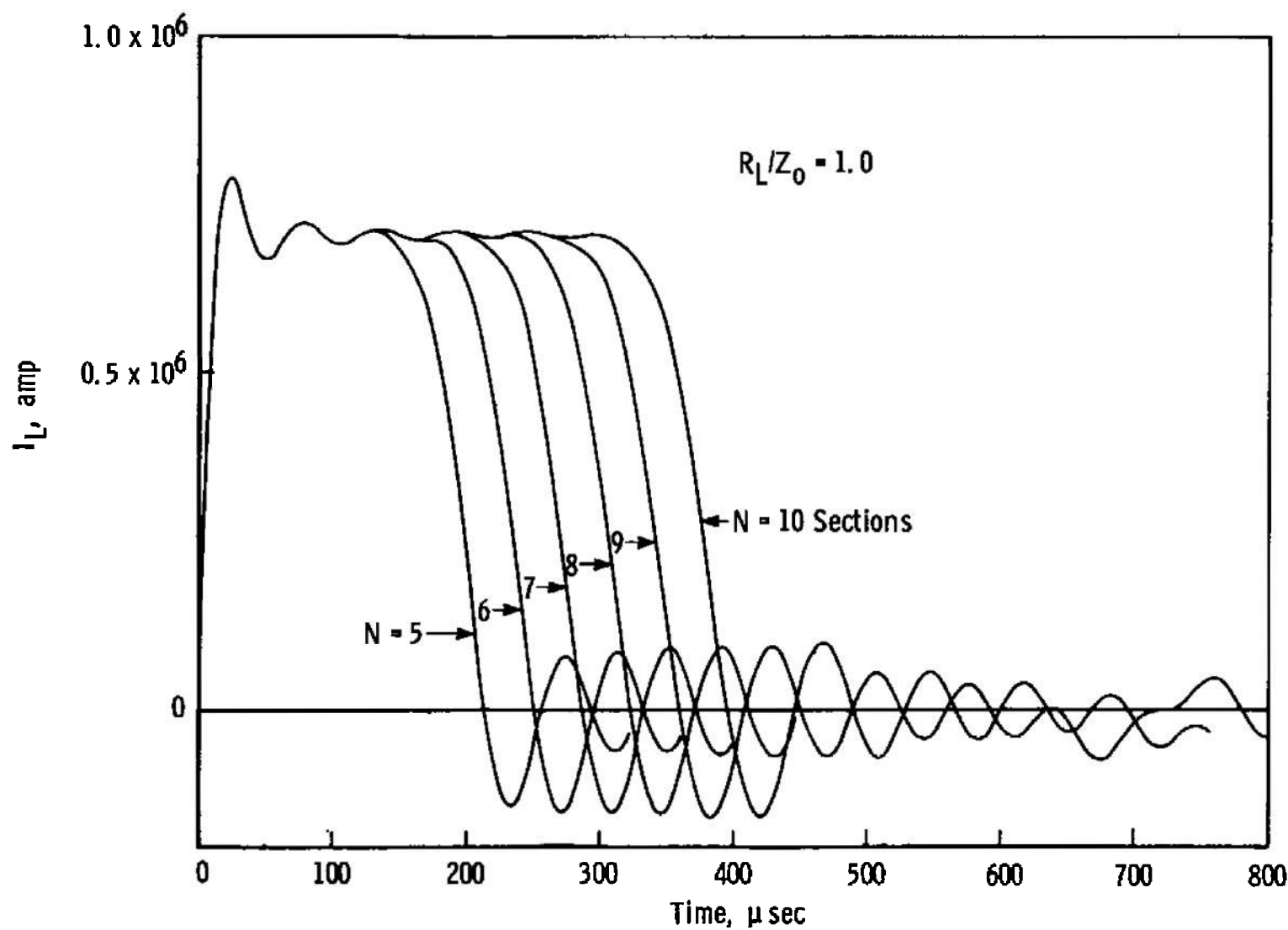


Fig. 25 Load Current as a Function of Time and Number of Sections in Transmission Line

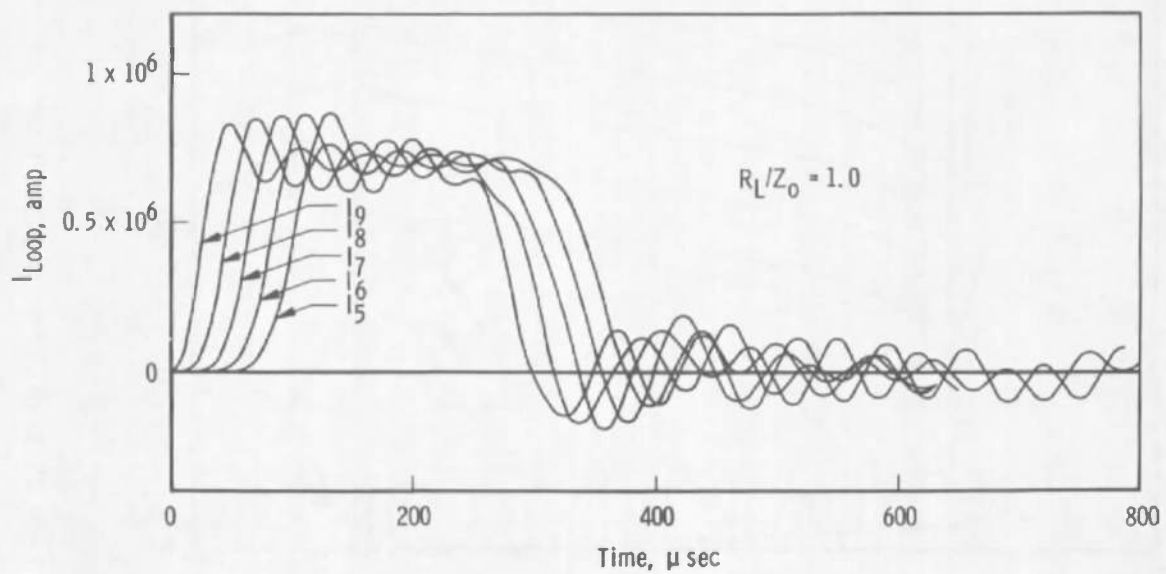
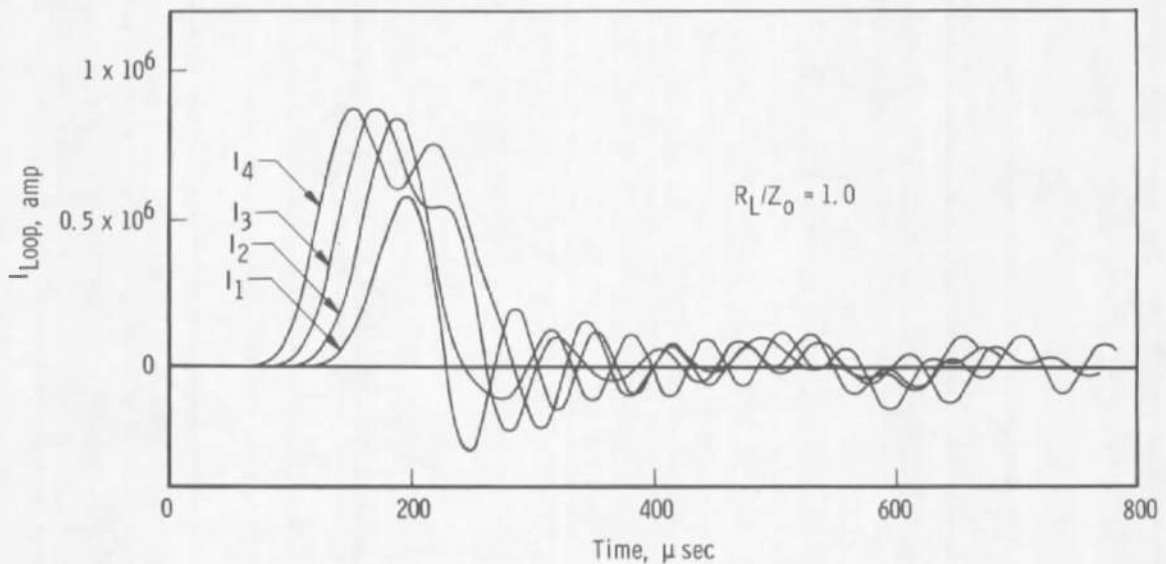


Fig. 26 Current in Each Loop of the Transmission Line as a Function of Time

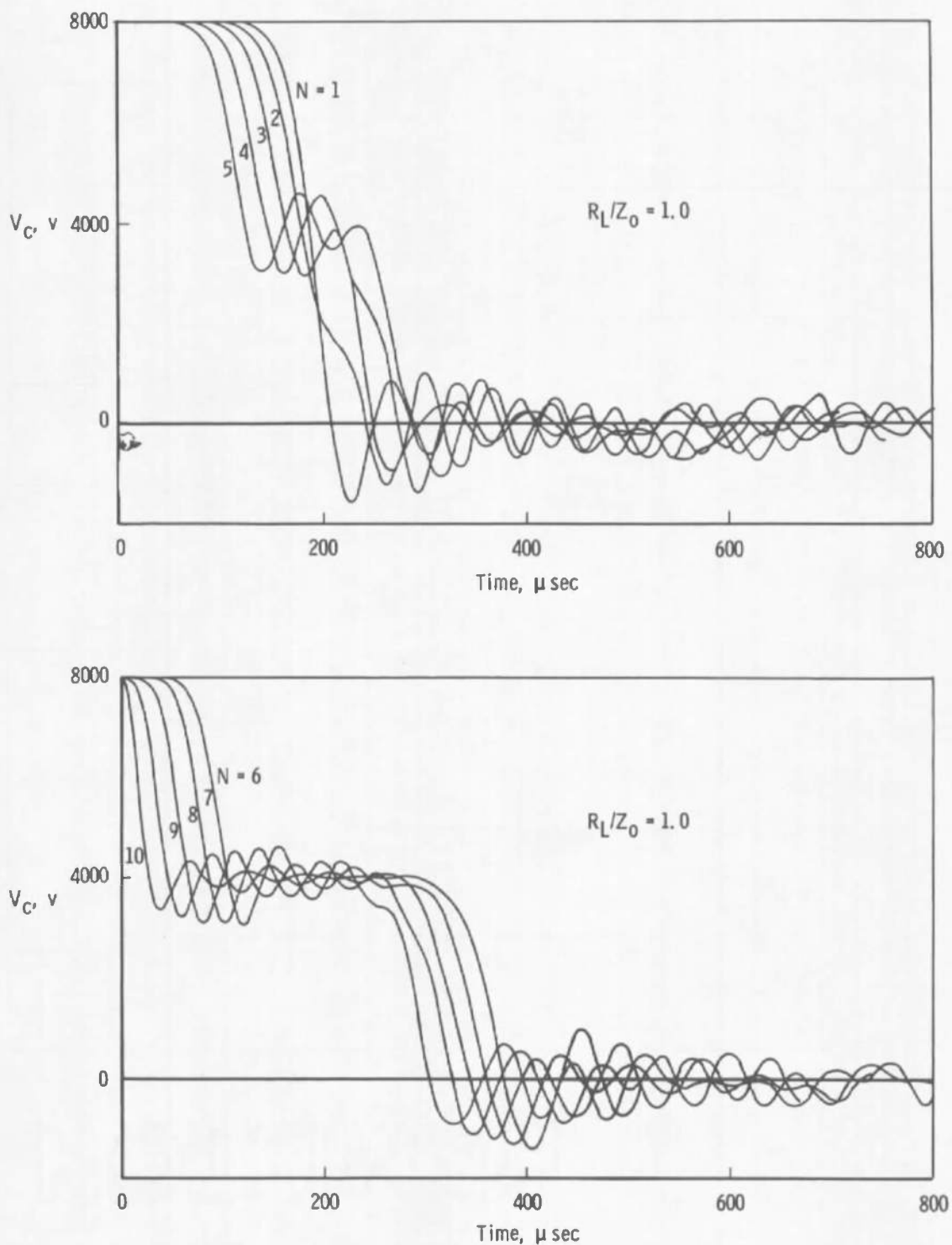


Fig. 27 Voltage across Section Capacitance as a Function of Time

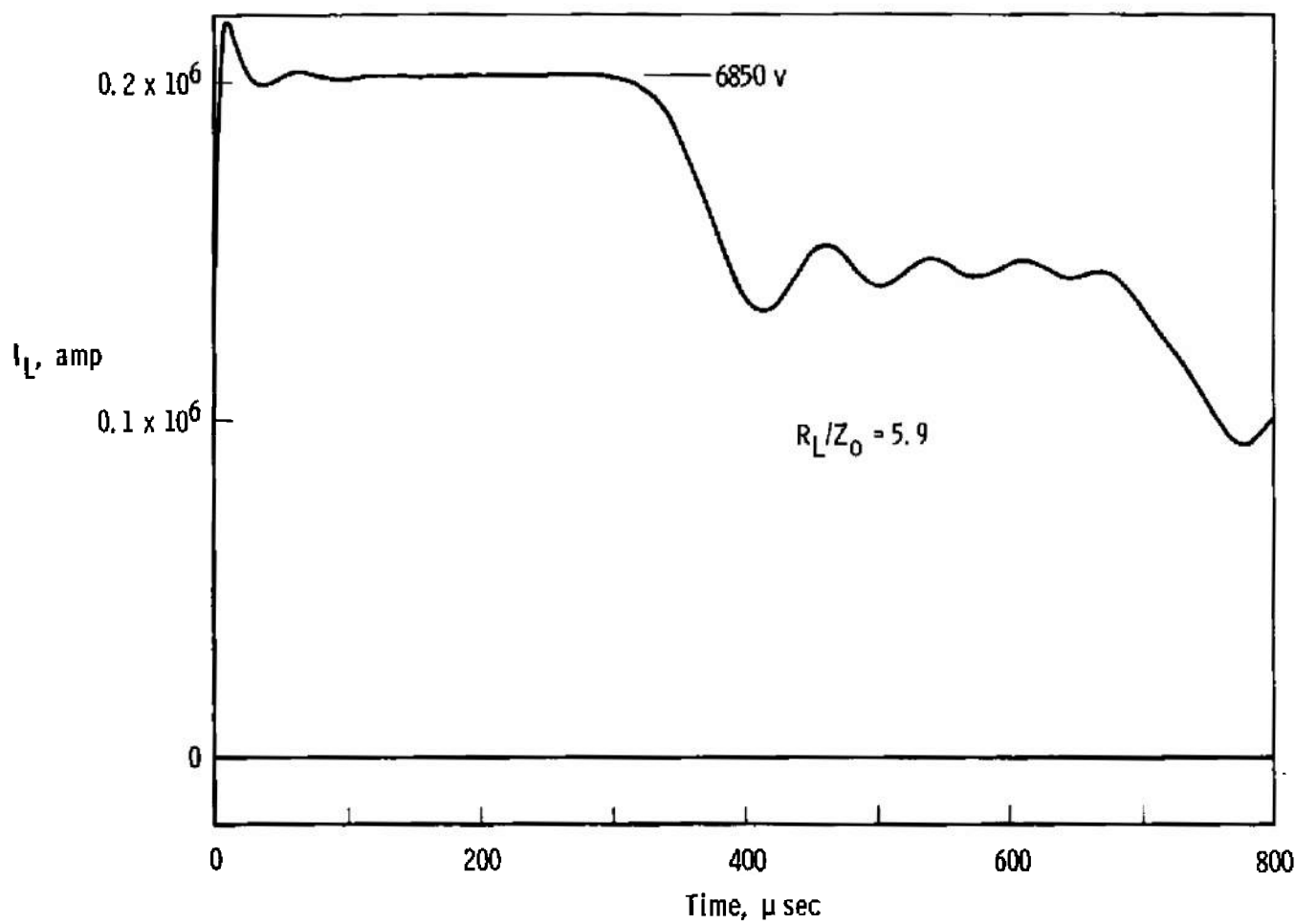


Fig. 28 Load Current as a Function of Time

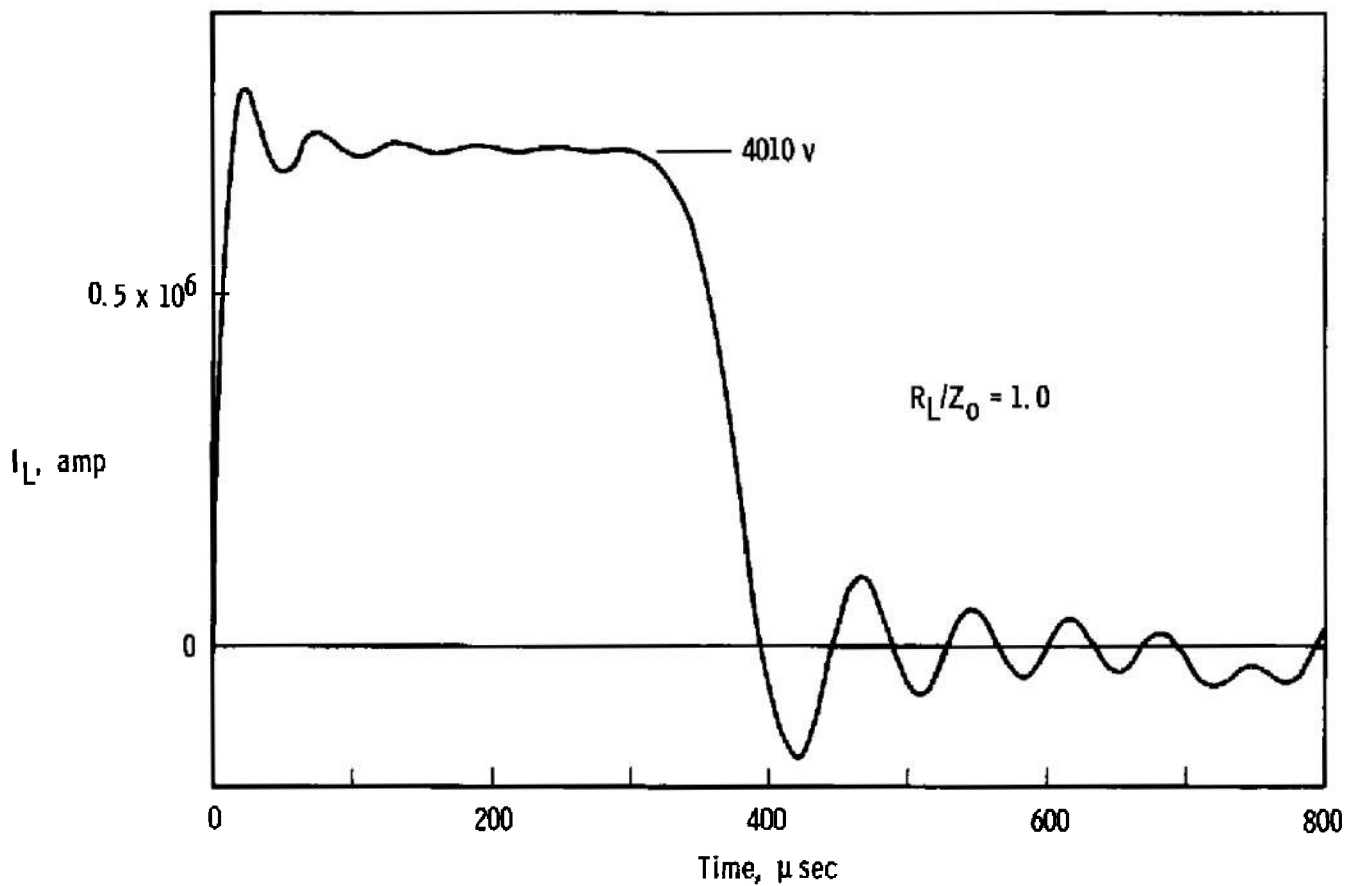


Fig. 28 Continued

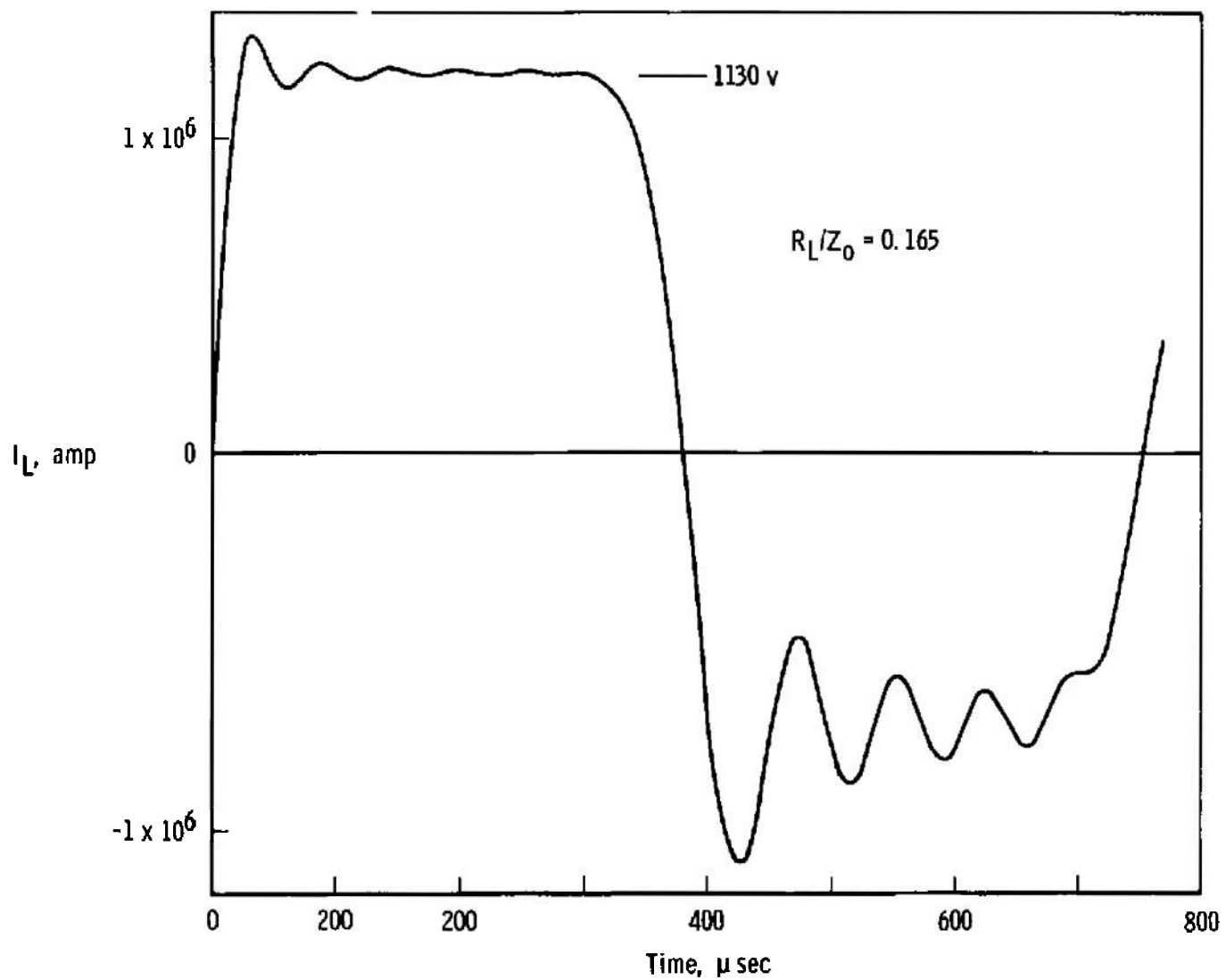


Fig. 28 Concluded

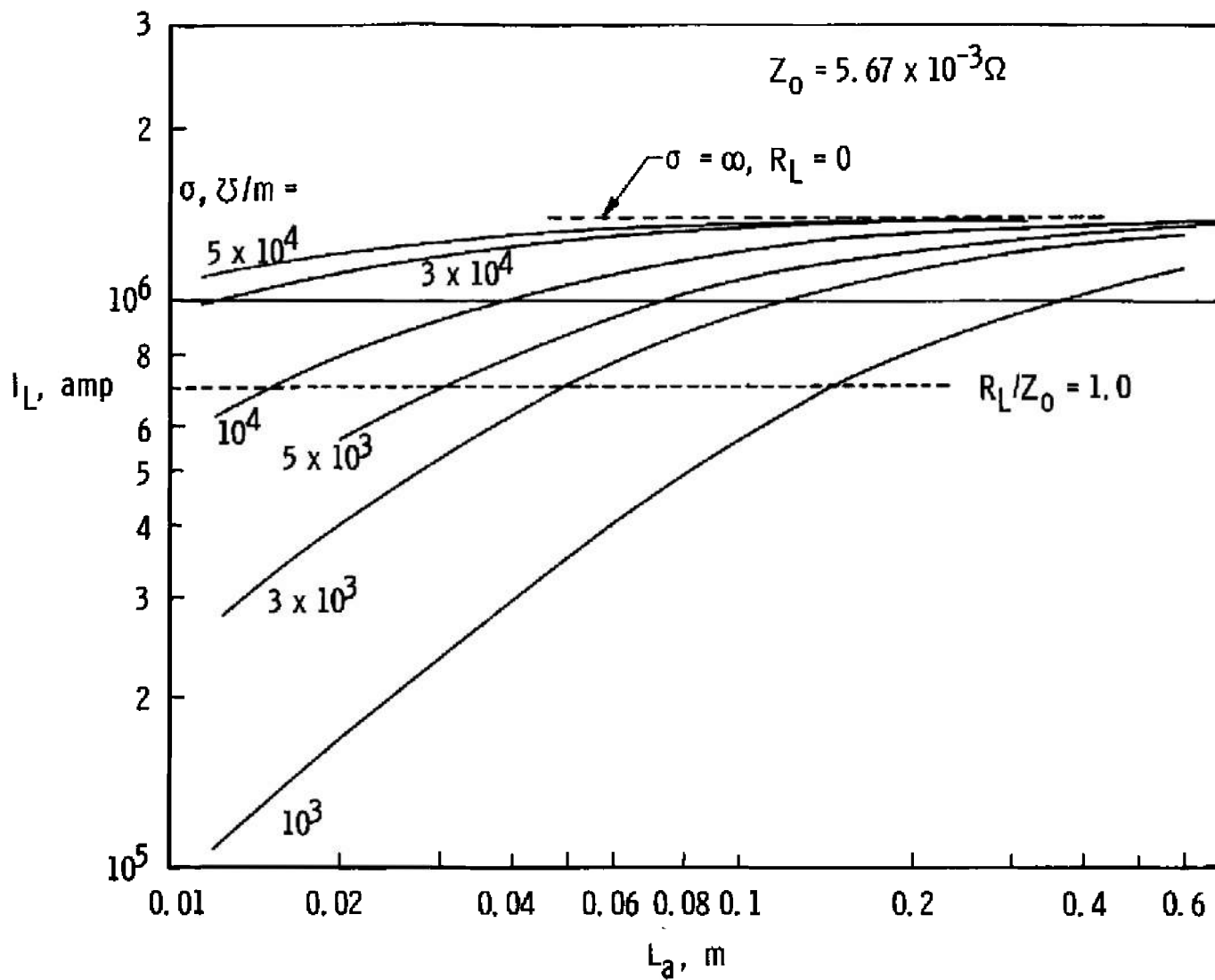


Fig. 29 Load Current as a Function of Accelerator Electrode Length for Different Gas Conductivities

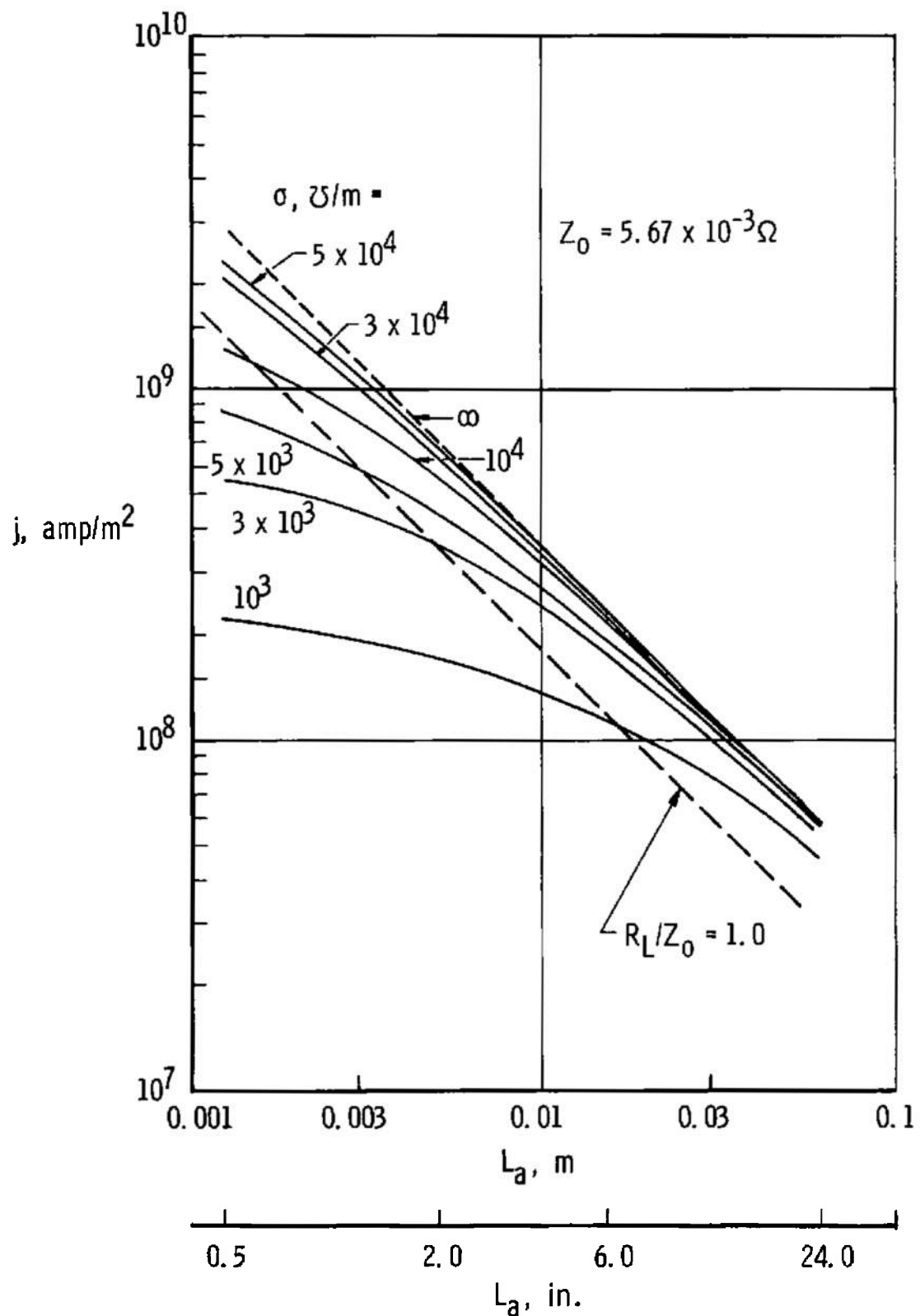


Fig. 30 Current Density as a Function of Accelerator Electrode Length
for Different Gas Conductivities

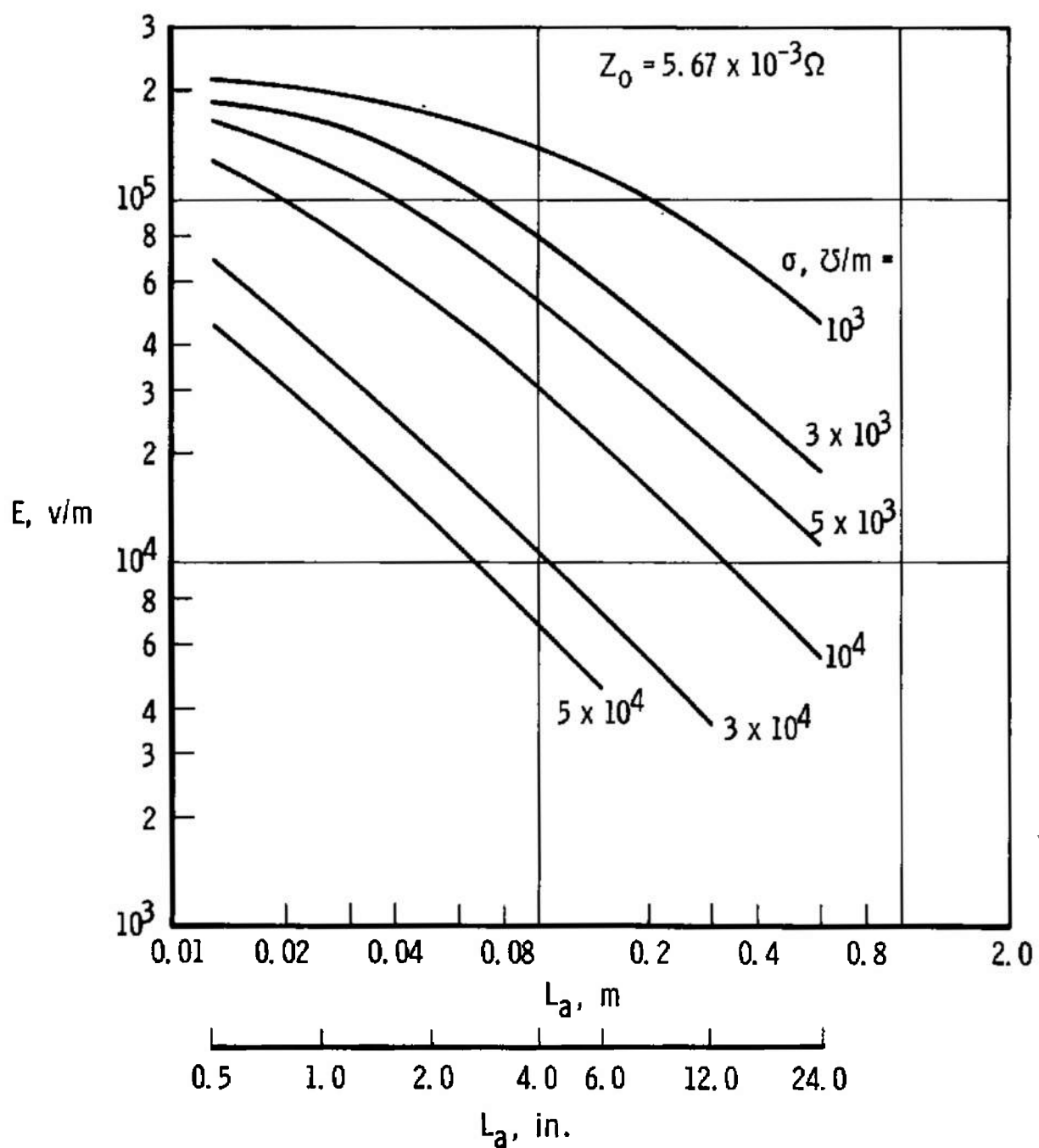
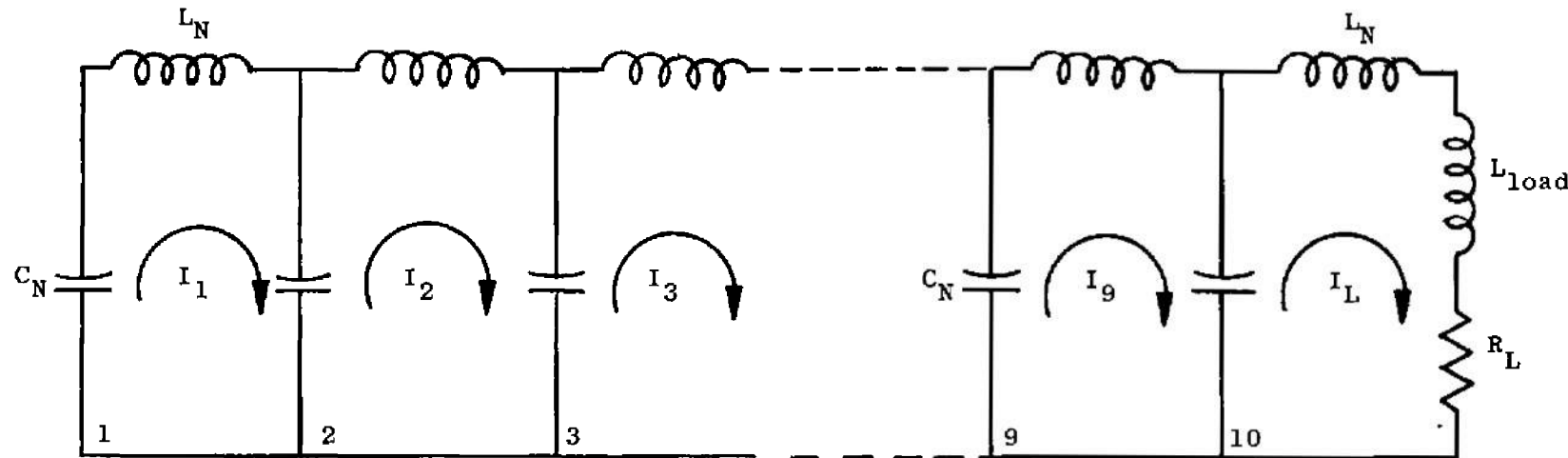


Fig. 31 Electric Field Intensity as a Function of Accelerator Electrode Length for Different Gas Conductivities



$$L_N = 1.0 \times 10^{-7} \text{ henries}$$

$$C_N = 0.0031 \text{ farad}$$

$$Z_o = 0.00567 \text{ ohm}$$

$$V_o = 8000 \text{ volts}$$

Fig. 32 Schematic Diagram for Lossless Transmission Line with a Load Consisting of Resistance and Inductance - Case Two

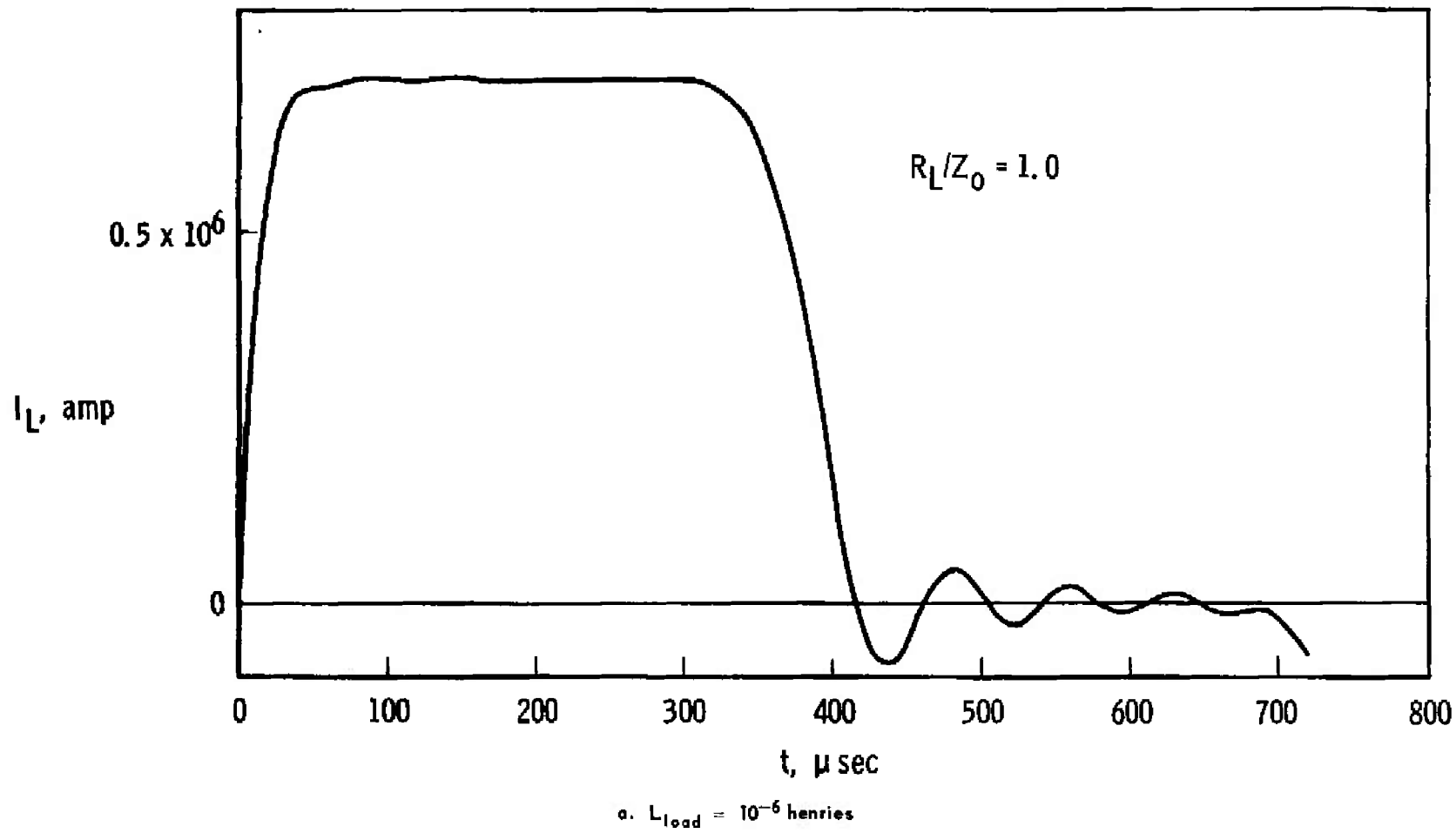
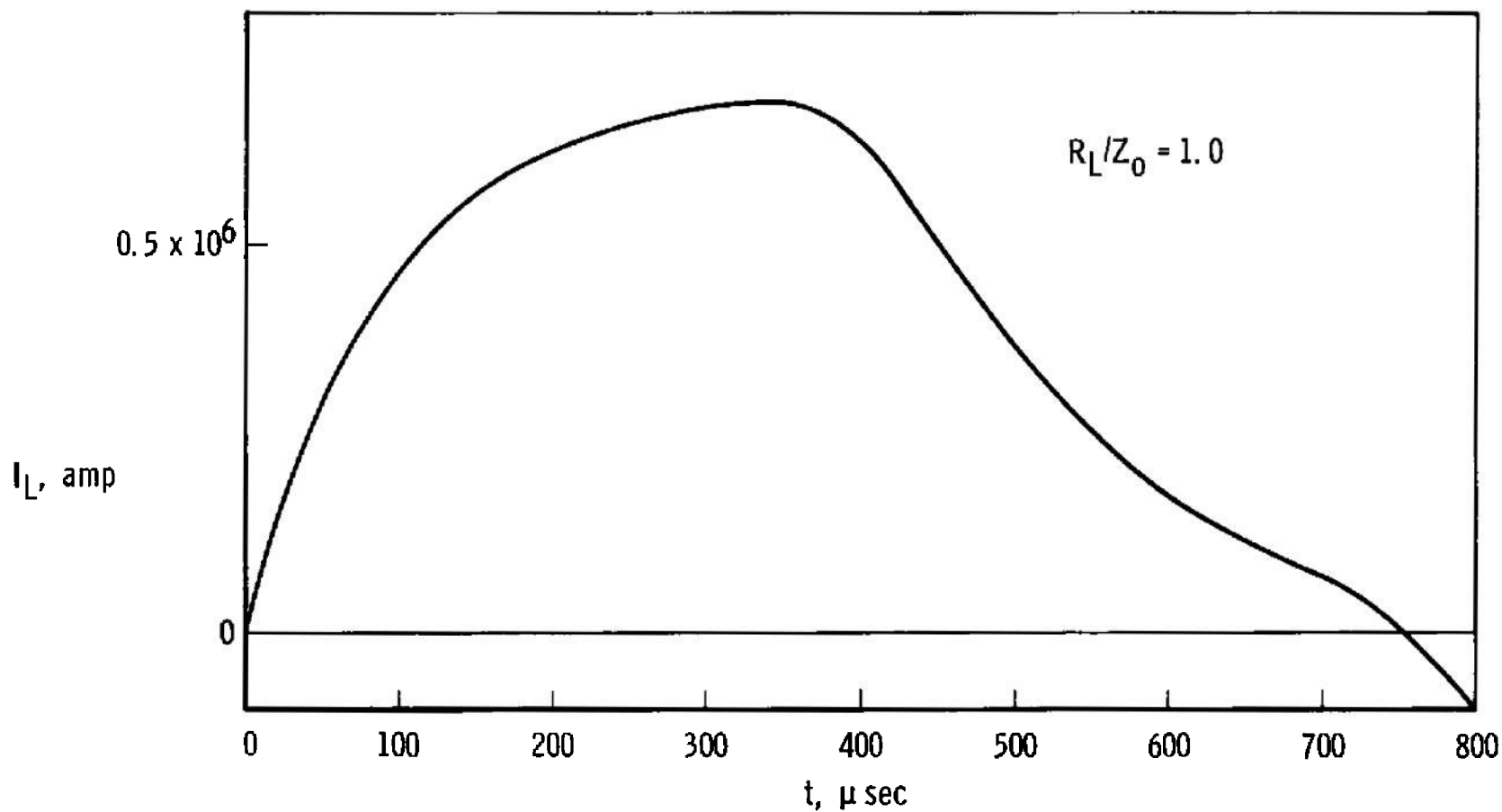
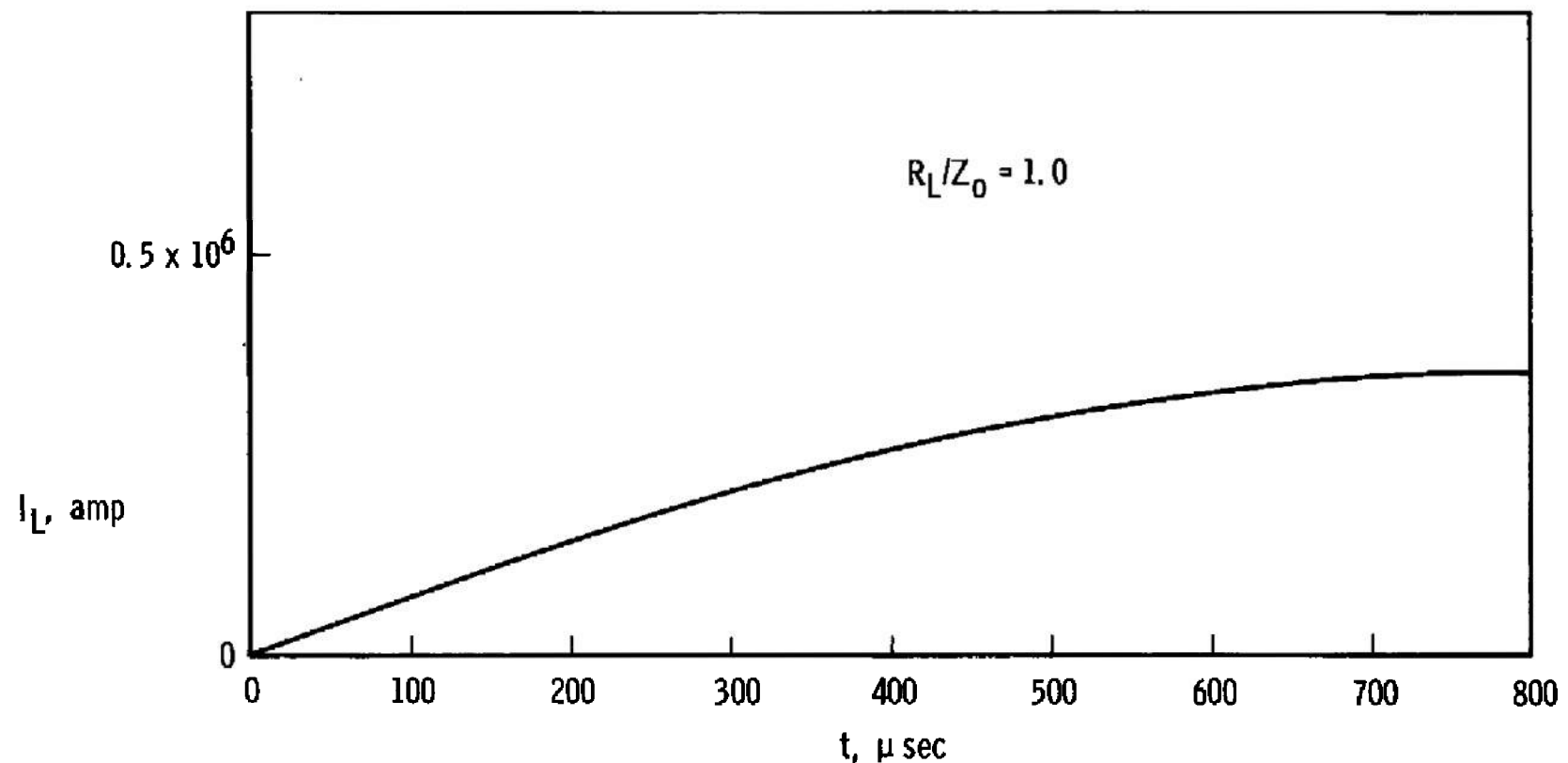


Fig. 33 Load Current as a Function of Time and Load Inductance



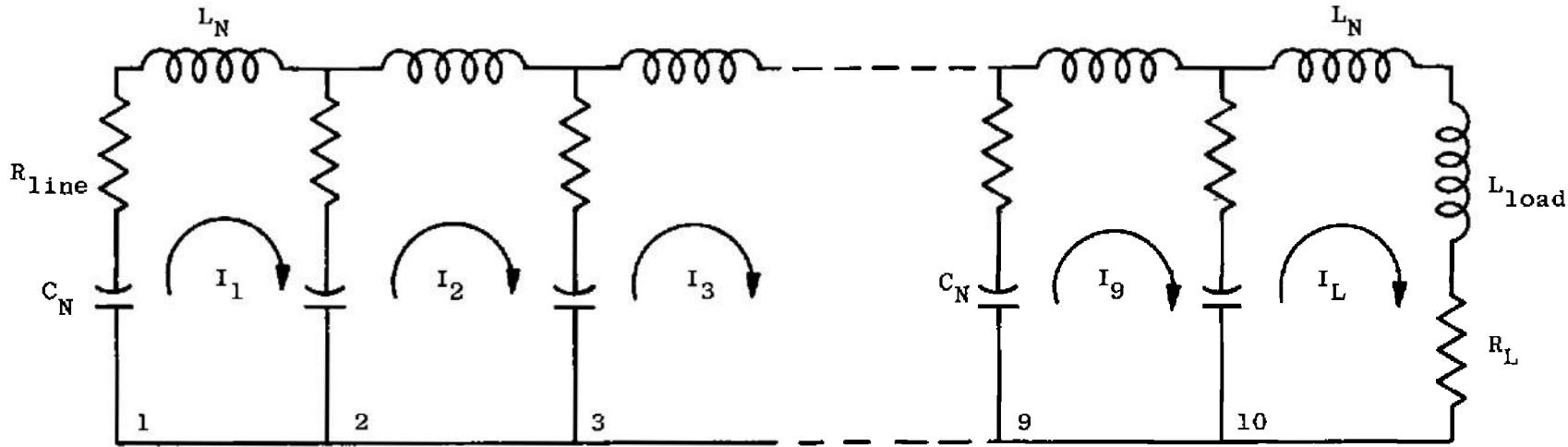
b. $L_{load} = 5 \times 10^{-6}$ henries

Fig. 33 Continued



c. $L_{load} = 10^{-5}$ henries

Fig. 33 Concluded



$$L_N = 1.0 \times 10^{-7} \text{ henries}$$

$$C_N = 0.0031 \text{ farad}$$

$$Z_O = 0.00567 \text{ ohm}$$

$$V_O = 8000 \text{ volts}$$

$$\underline{R_{line}, \text{ ohms}}$$

$$(1) 5.0 \times 10^{-5}$$

$$(2) 0.5 \times 10^{-3}$$

$$(3) 1.0 \times 10^{-3}$$

$$(4) 5.0 \times 10^{-3}$$

Fig. 34 Schematic Diagram for a Transmission Line with Uniform Resistance in Each Loop - Case Three

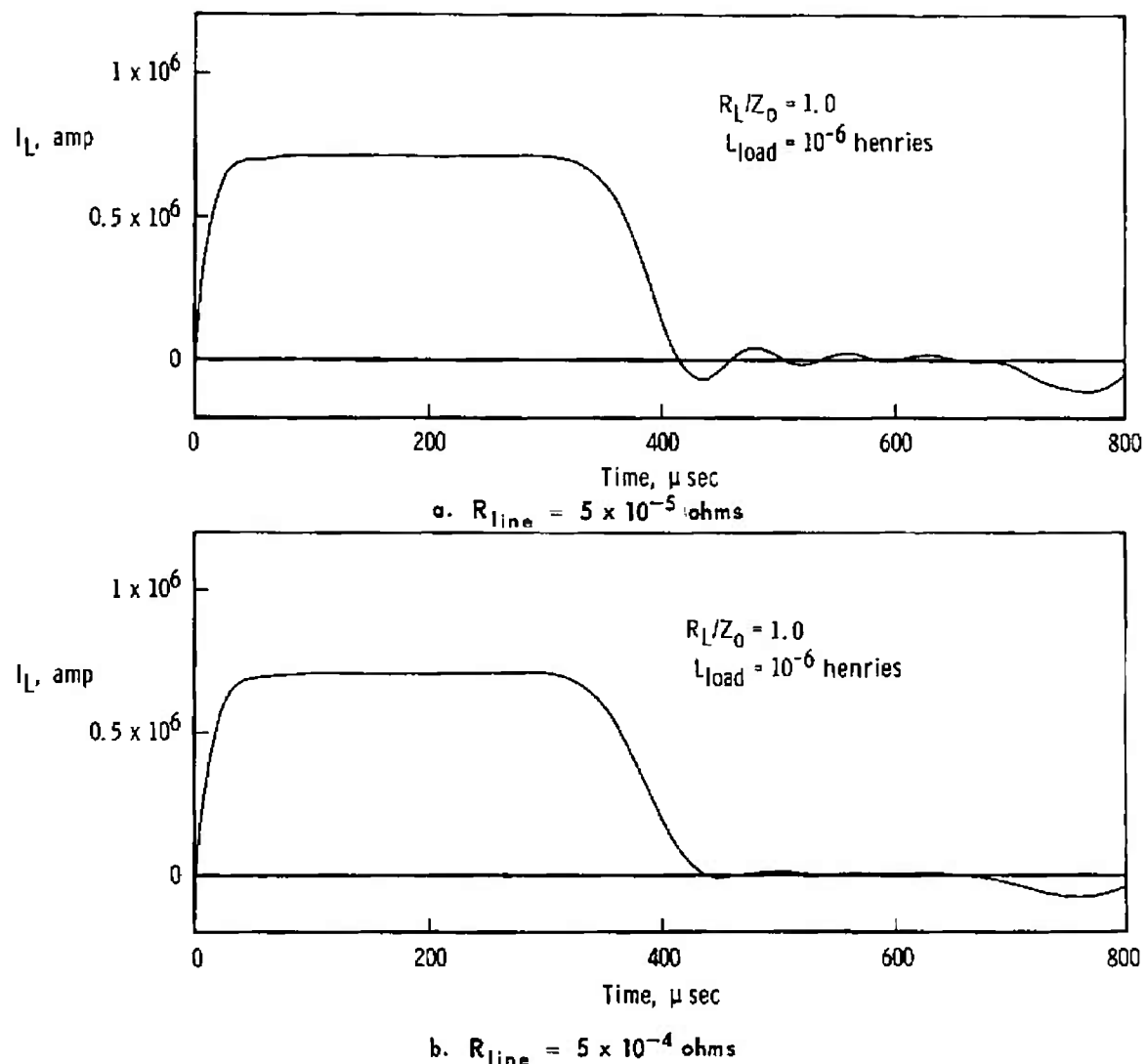


Fig. 35 Load Current as a Function of Time and Line Resistance

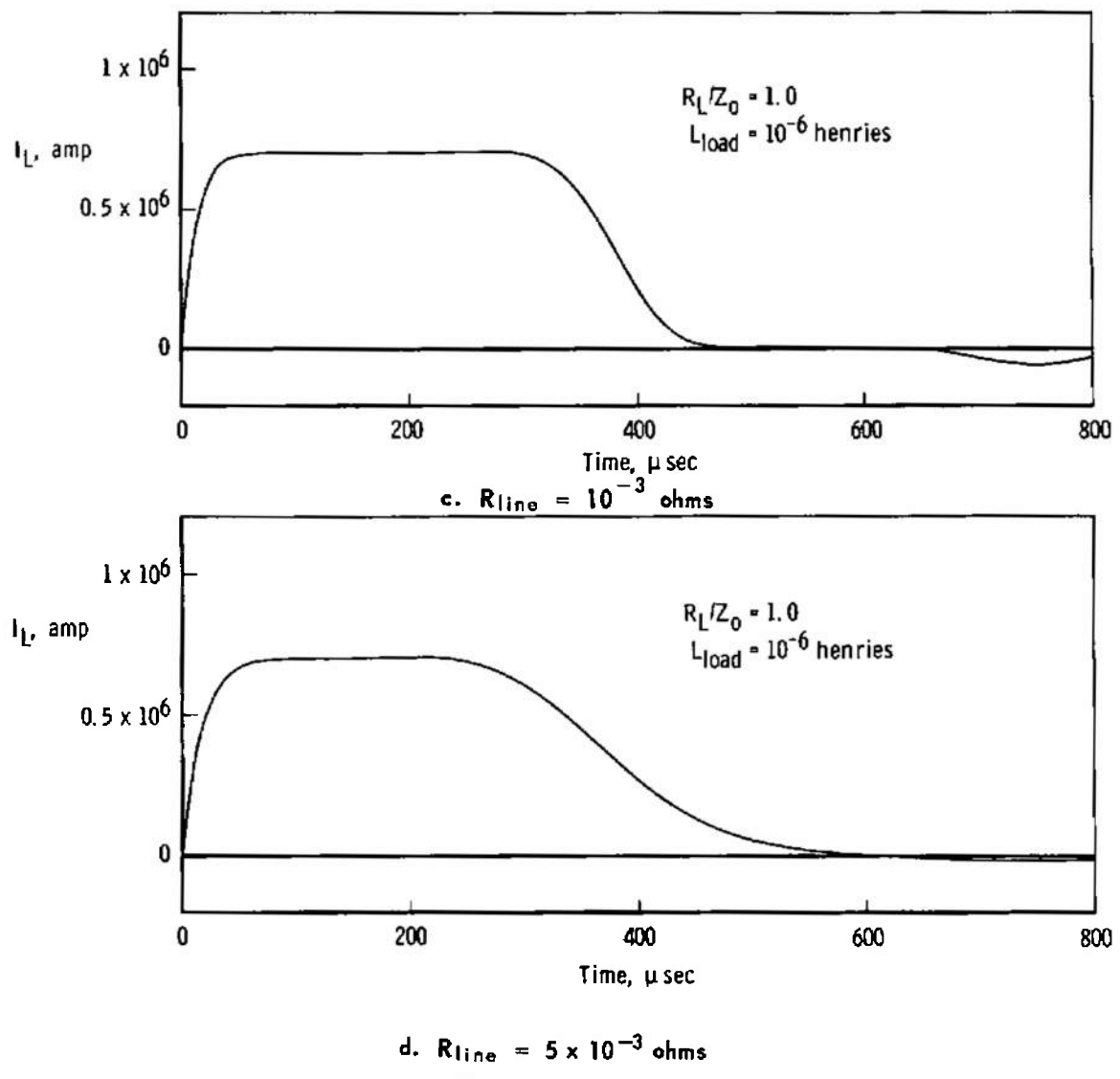
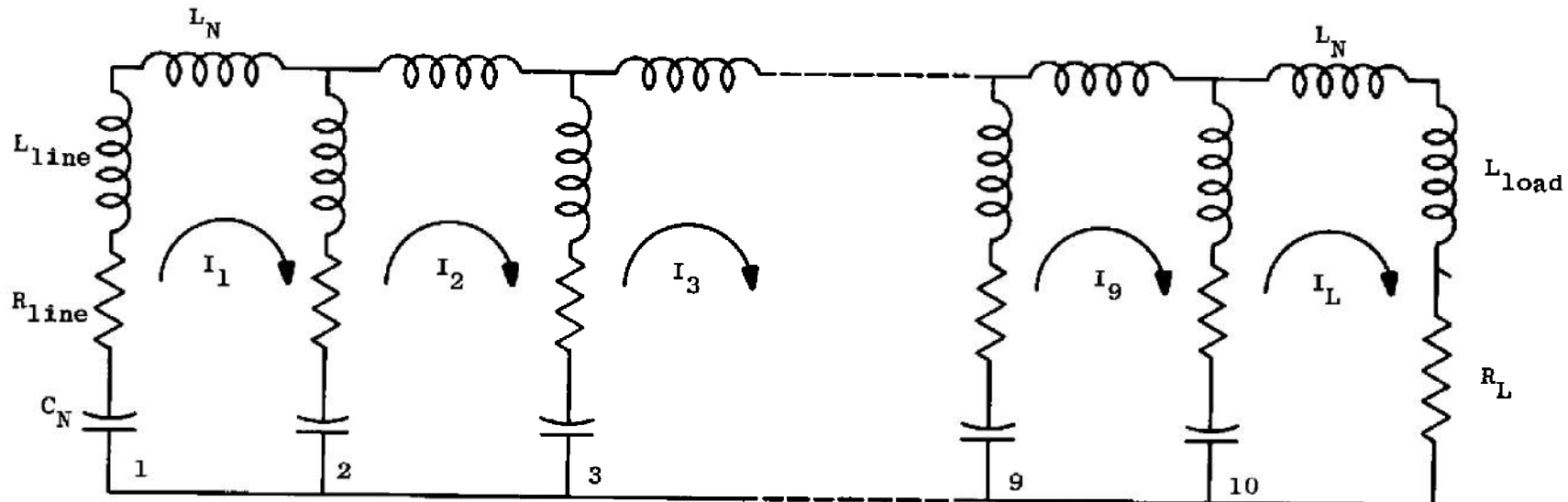


Fig. 35 Concluded



$$C_n = 0.00315 \text{ farad}$$

$$L_{\text{line}} = 2.86 \times 10^{-8} \text{ henries}$$

$$R_{\text{line}} = 1.04 \times 10^{-3} \text{ ohms}$$

$$L_{\text{load}} = 0.1 \times 10^{-6} \text{ henries}$$

$$L_N, \text{ henries}$$

$$(1) 0.128 \times 10^{-6}$$

$$(2) 0.512 \times 10^{-6}$$

$$(3) 1.15 \times 10^{-6}$$

$$(4) 1.77 \times 10^{-6}$$

$$(5) 3.20 \times 10^{-6}$$

$$Z_o, \text{ ohms}$$

$$0.0064$$

$$0.0128$$

$$0.0192$$

$$0.0238$$

$$0.032$$

$$t, \mu\text{sec}$$

$$400$$

$$800$$

$$1200$$

$$1600$$

$$2000$$

Fig. 36 Schematic Diagram for a Transmission Line with Inductance and Resistance in Series with the Capacitor of Each Loop - Case Four

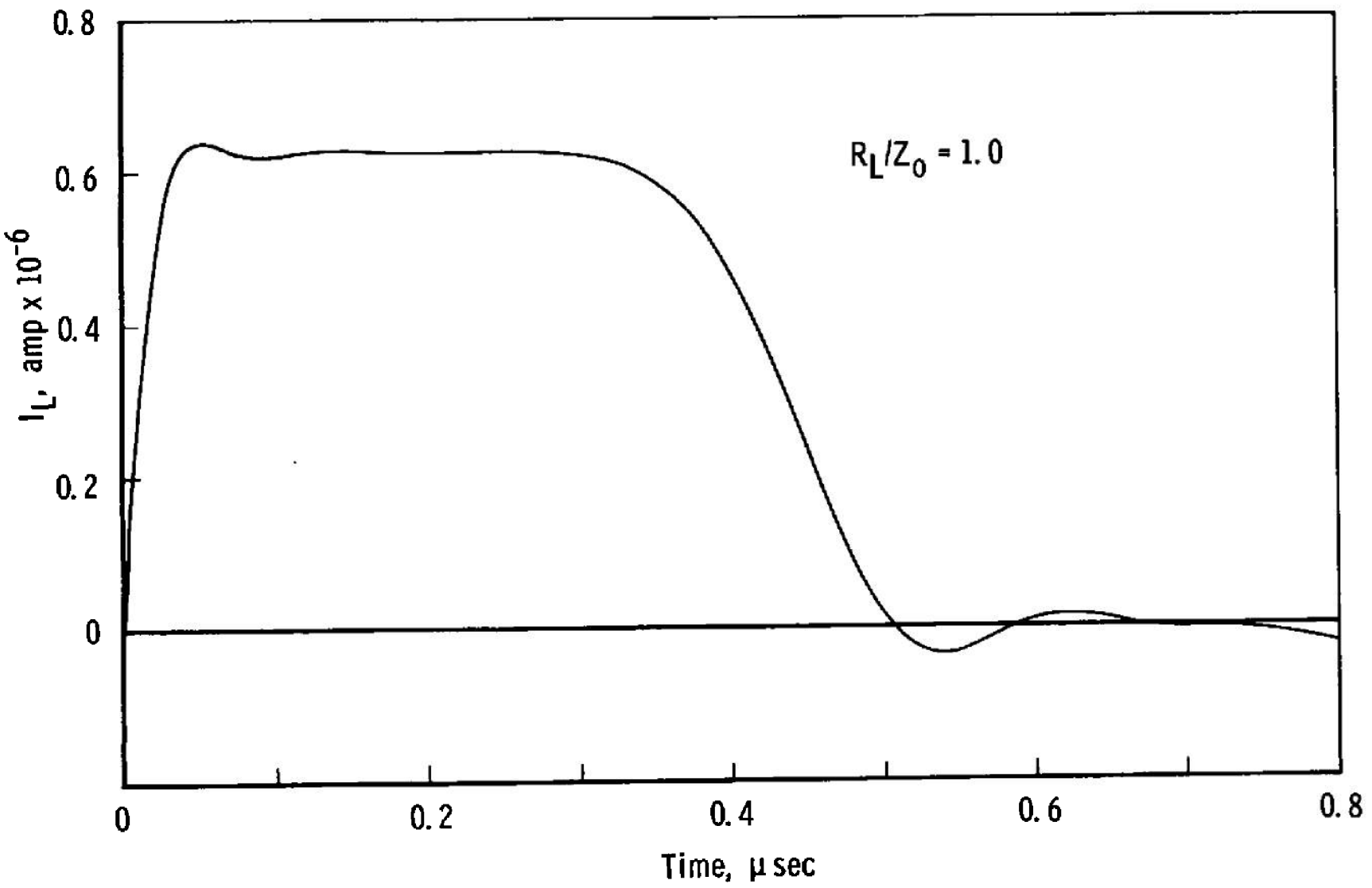


Fig. 37 Load Current as a Function of Time and Load Resistance for $L_N = 0.128 \times 10^{-6}$ henries

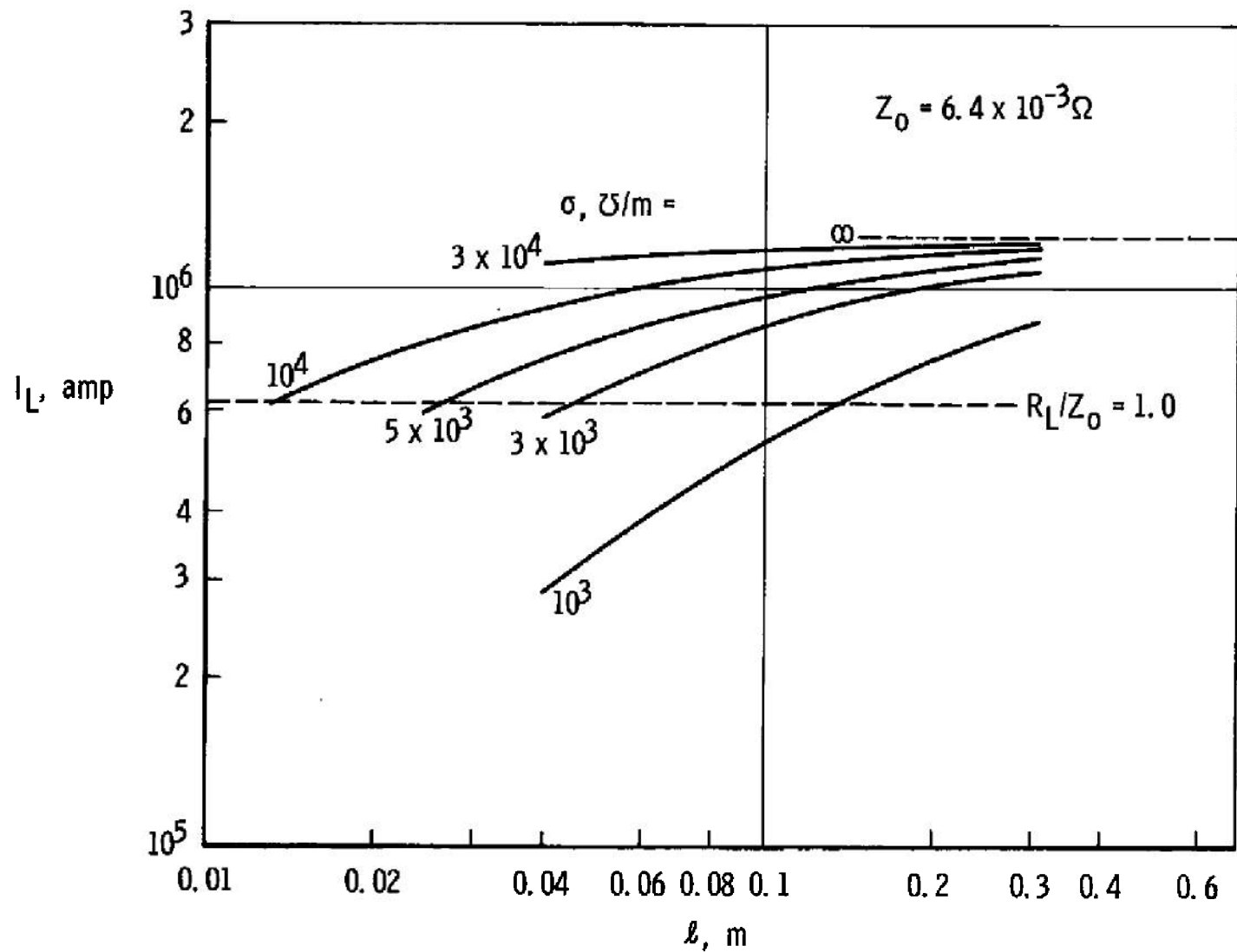


Fig. 38 Load Current as a Function of Accelerator Electrode Length and Gas Conductivity for $L_N = 0.128 \times 10^{-6}$ henries

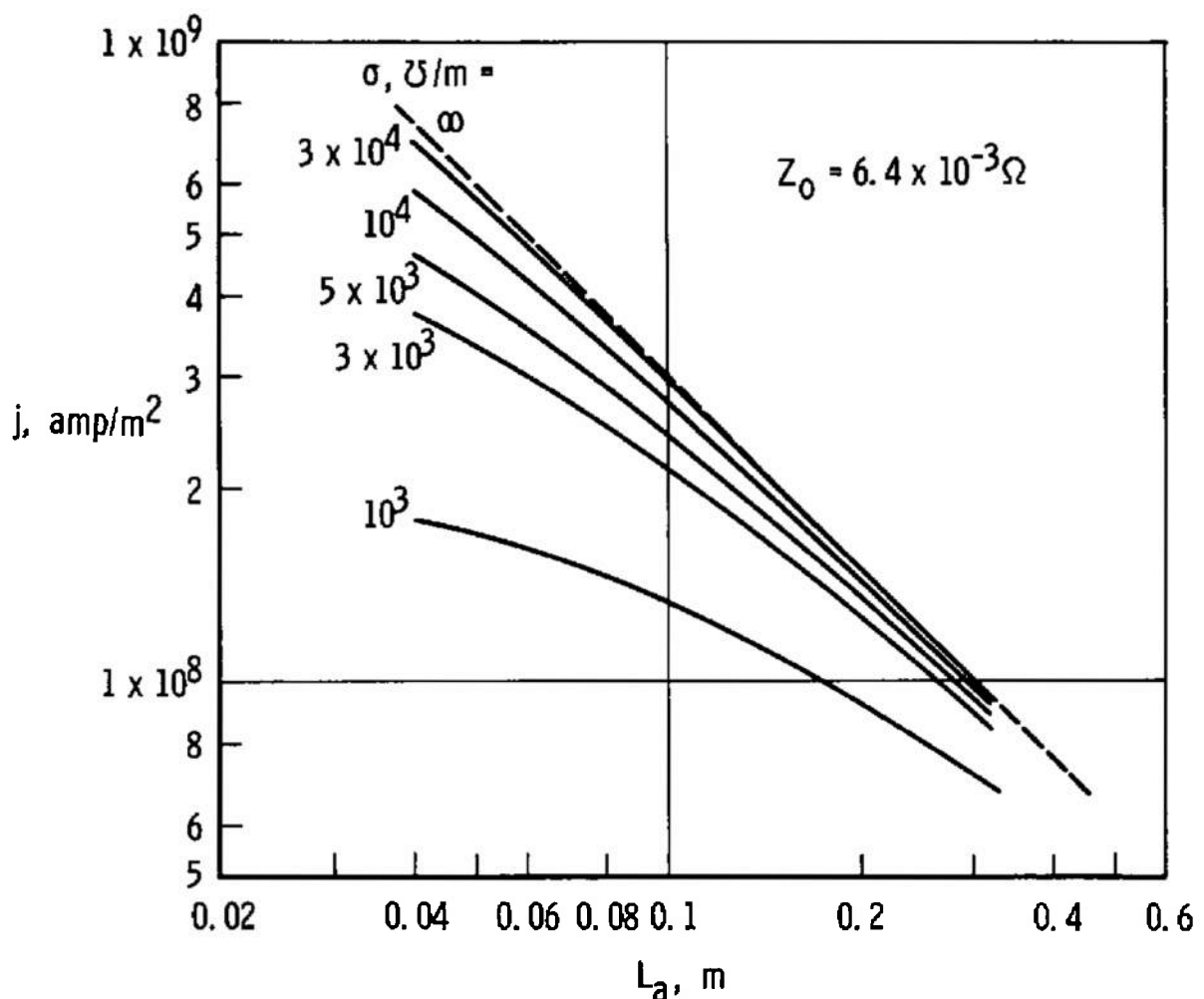
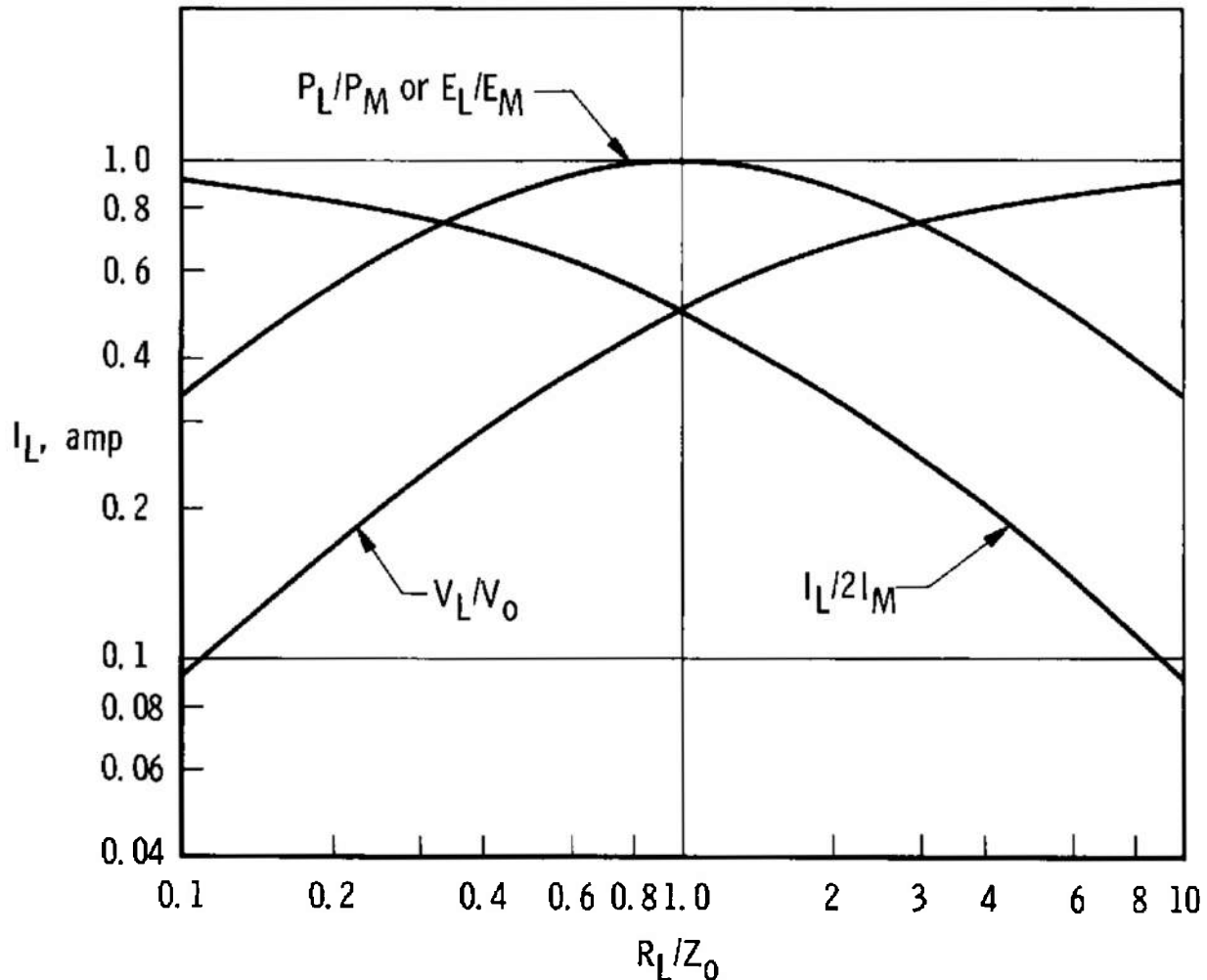


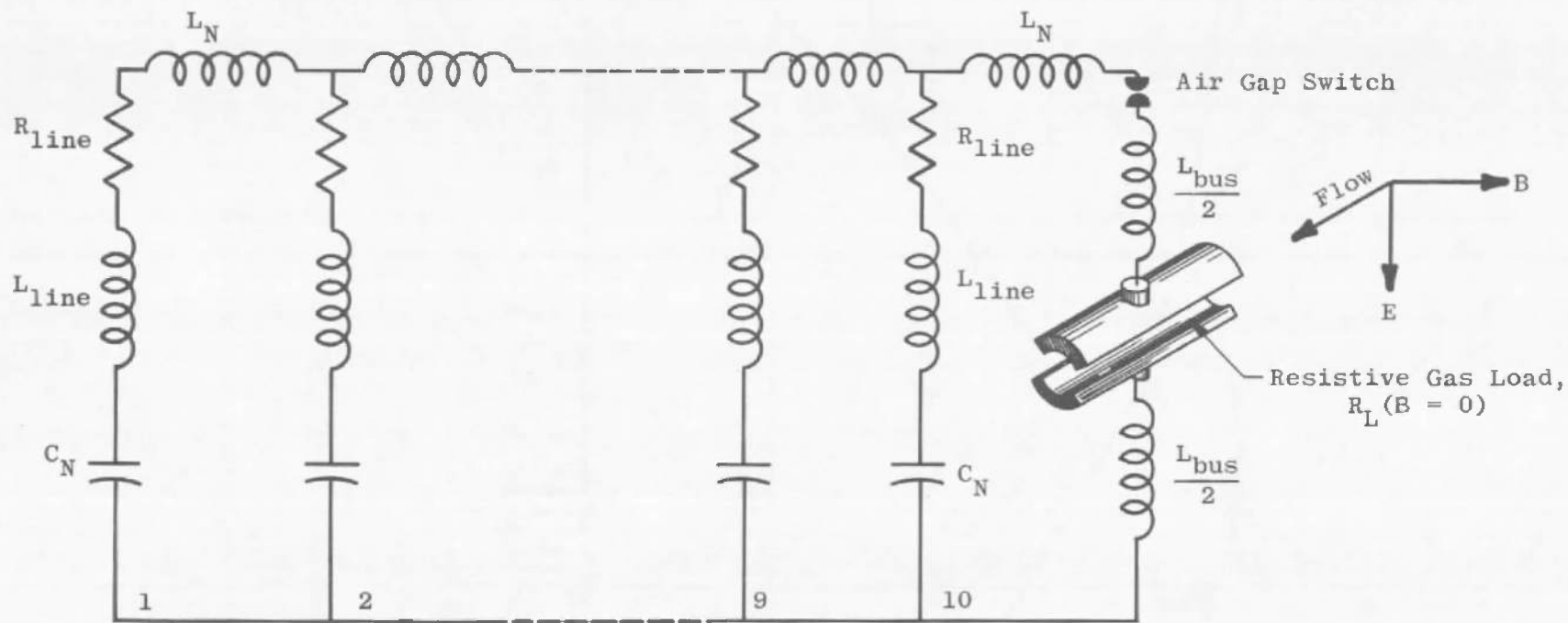
Fig. 39 Current Density as a Function of Accelerator Electrode Length and Gas Conductivity for $L_N = 0.128 \times 10^{-6}$ henries



Subscripts:

- M - denotes matched case
- L - denotes load
- o - denotes condition initial capacitor

Fig. 40 Nondimensional Power, Energy, Current, and Voltage as a Function of Impedance Matching



	<u>$t, \mu\text{sec}$</u>	<u>$L_N, \mu\text{H}$</u>	<u>$Z_O, \text{milliohms}$</u>
$C_N = 0.003125 \text{ farad}$			
$L_{\text{line}} = 0.0286 \text{ microhenries}$	400	0.128	6.4
$R_{\text{line}} = 1.04 \text{ milliohms}$	800	0.512	12.8
$L_{\text{bus}} = 0.8 \text{ microhenries}$	1200	1.15	19.2
$V_{O_{\text{max}}} = 8000 \text{ volts}$	1600	1.77	23.8
	2000	3.20	32.0

Fig. 41 Schematic Diagram for Simulated Transmission Line Electric Field System - Final Configuration

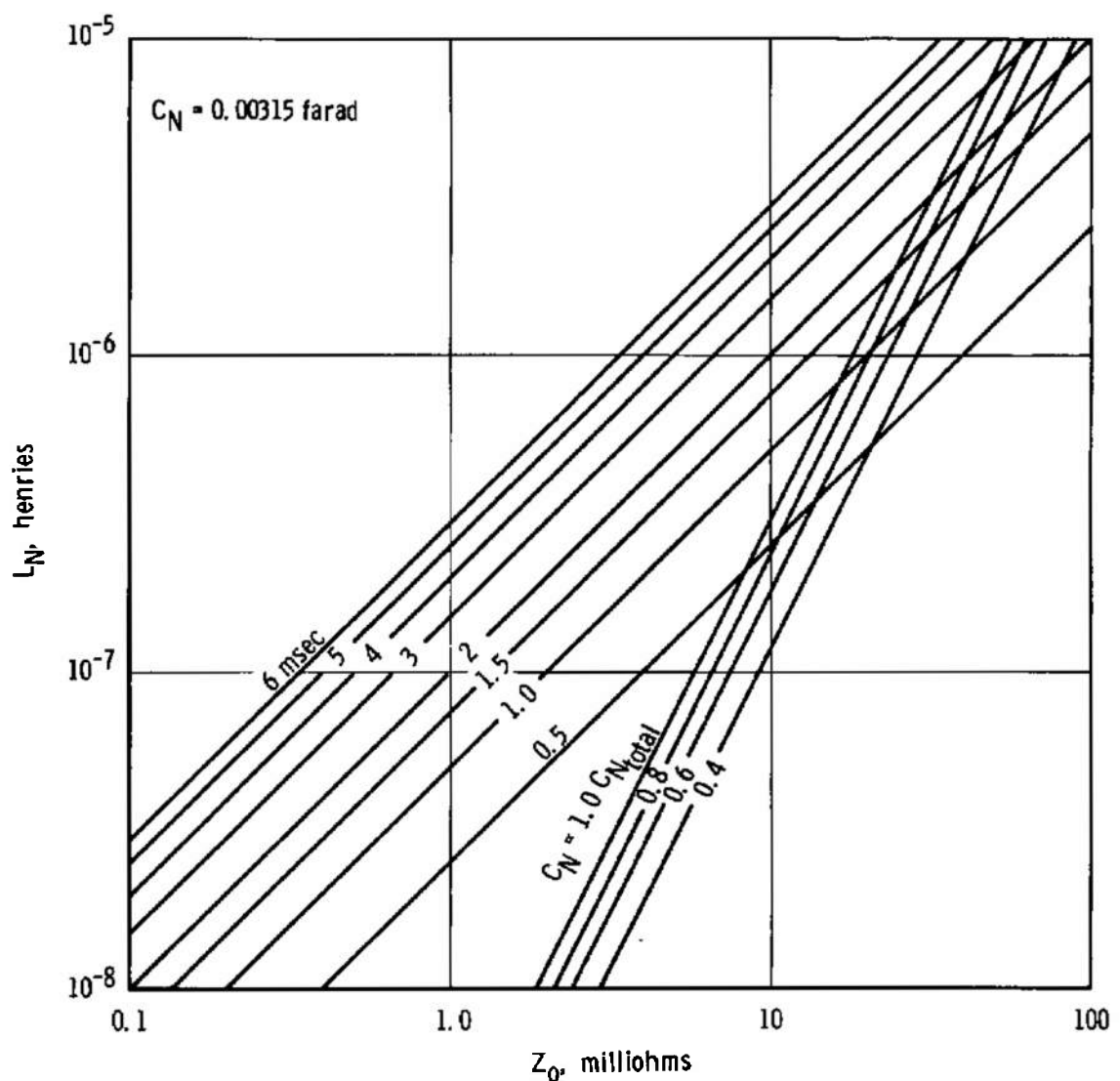
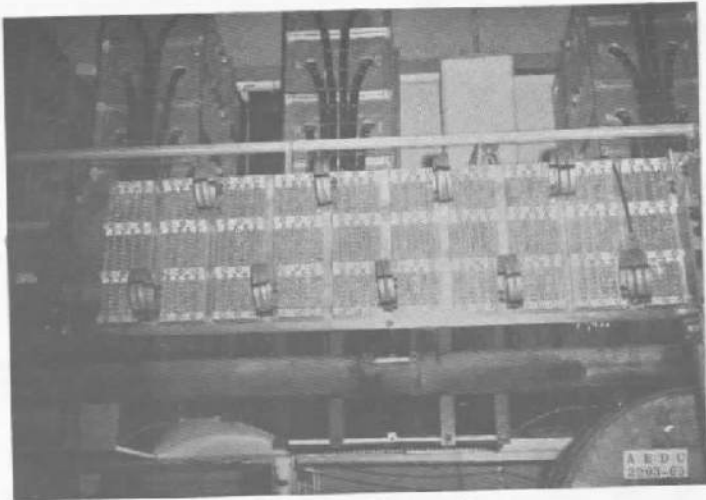


Fig. 42 Range of Impedance Match as a Function of L_N , C_N , and Total Test Time



Racked Capacitors in One
Section

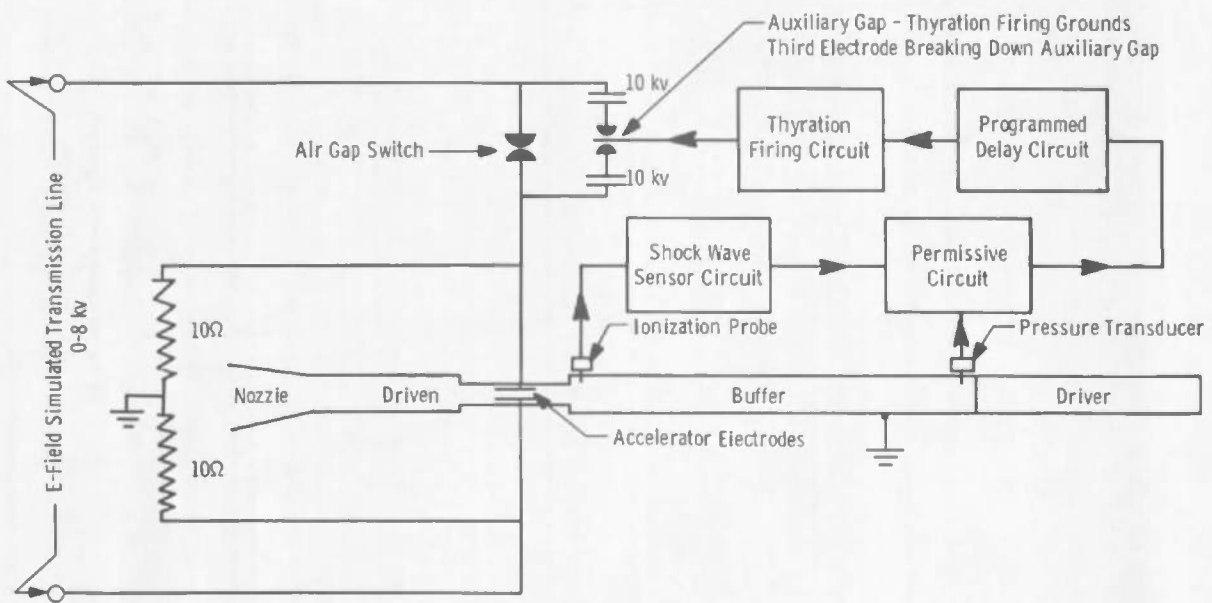


Inductor-Collector Plates



View of Complete System

Fig. 43 Photographs of Electric Field System and Components



Schematic

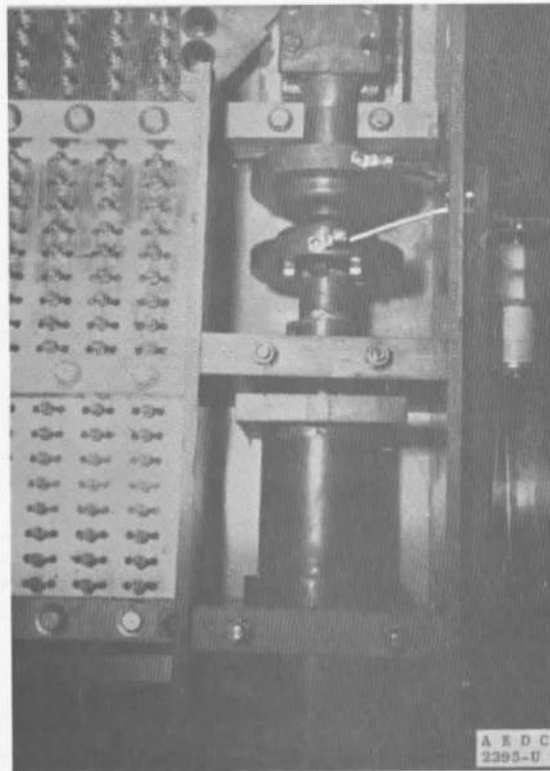


Fig. 44 Schematic and Photograph of Air Gap Switch

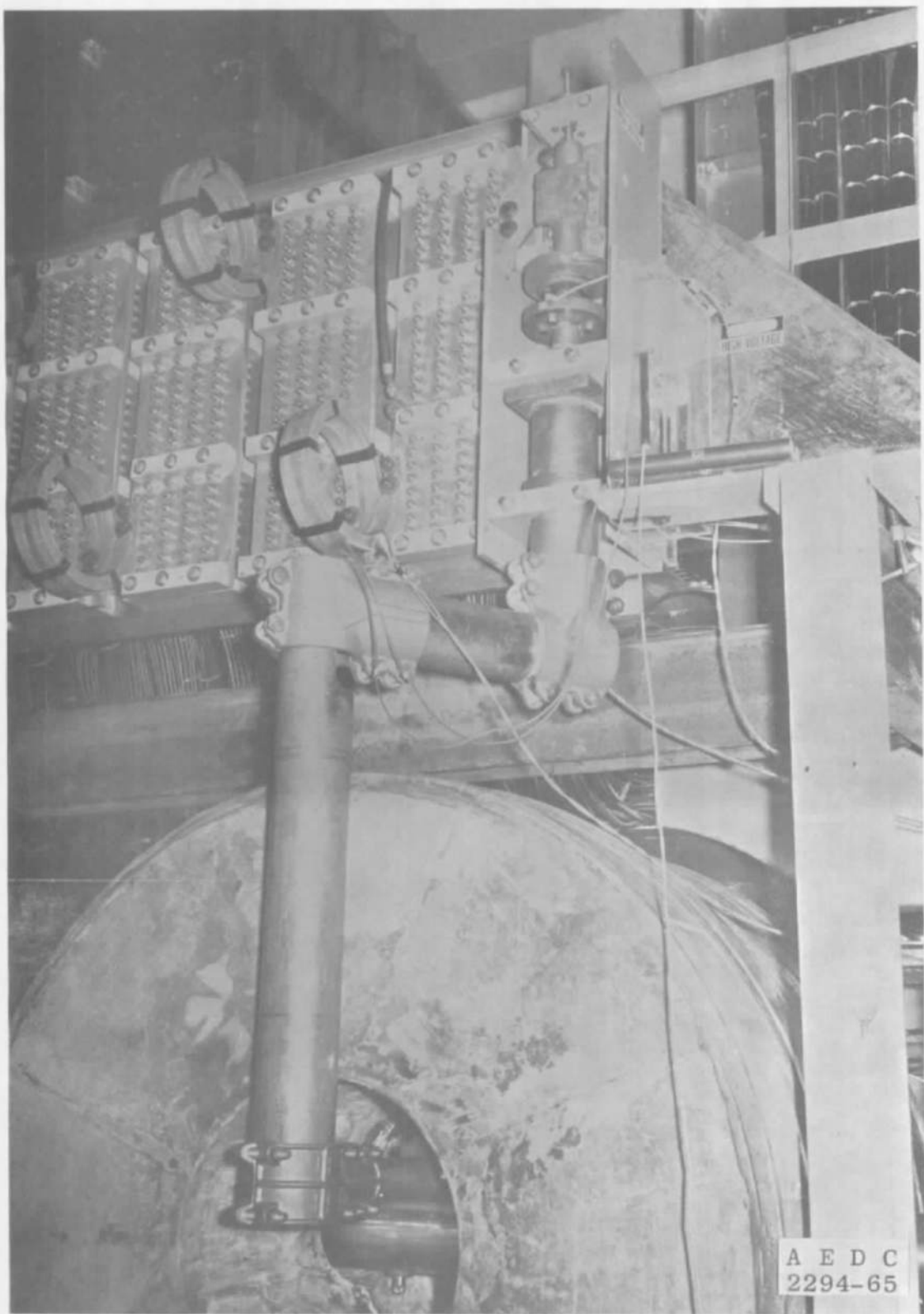
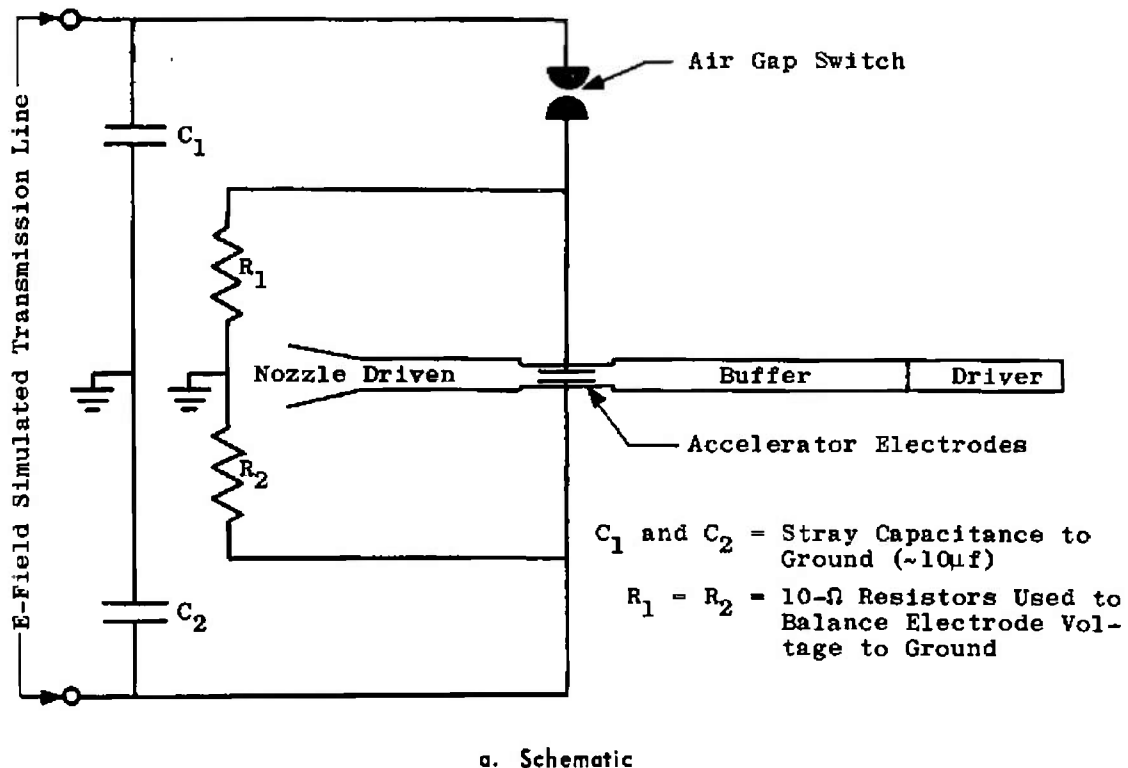
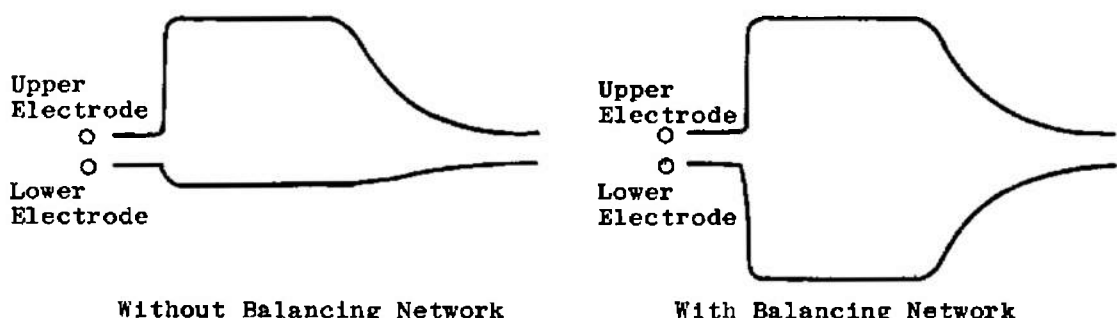


Fig. 45 Photograph of Coaxial Bus System to Accelerator Electrodes



a. Schematic



b. Typical Electrode to Ground Voltage Traces

Fig. 46 Accelerator Electrode Voltage Balancing Network

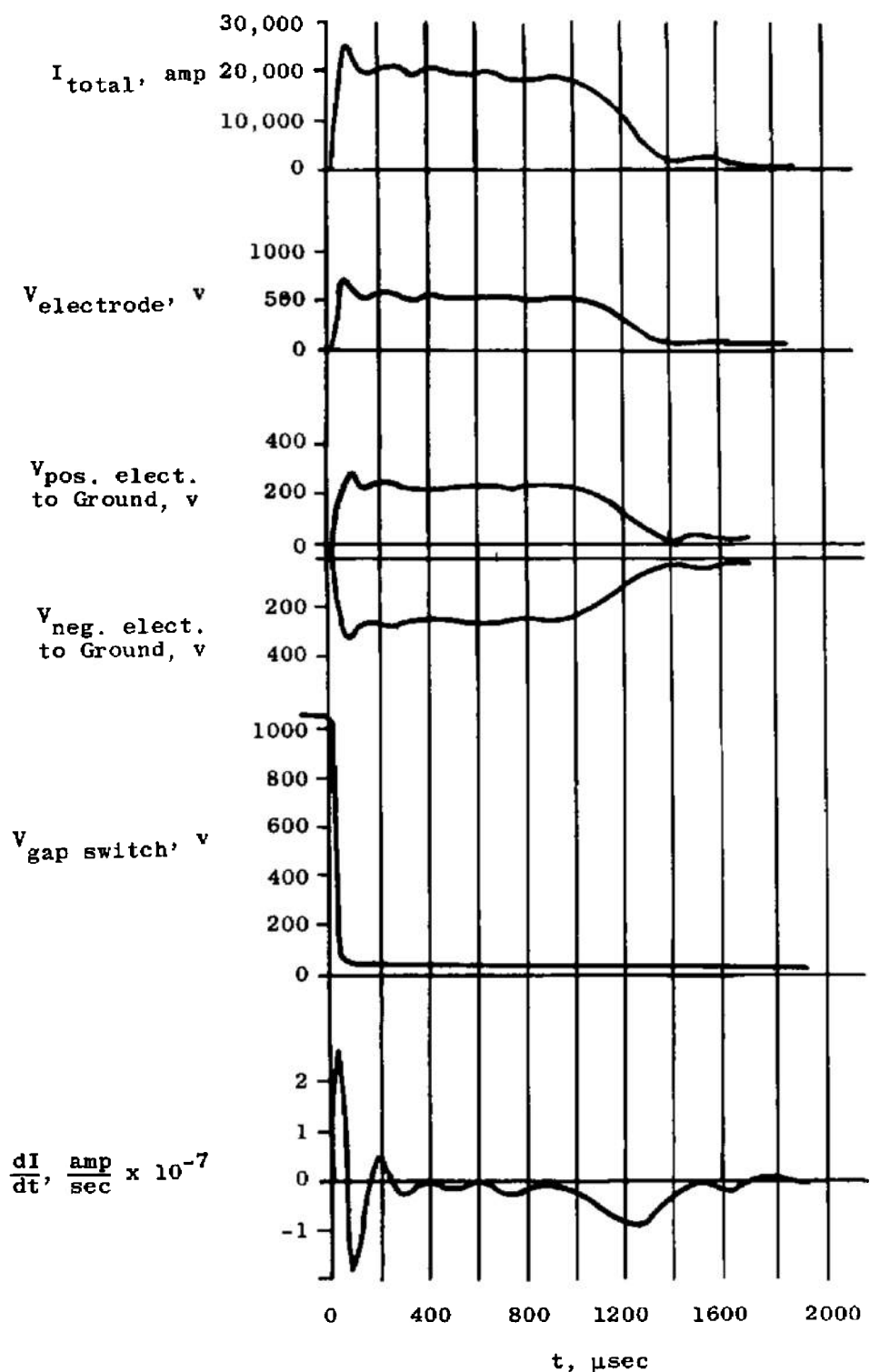
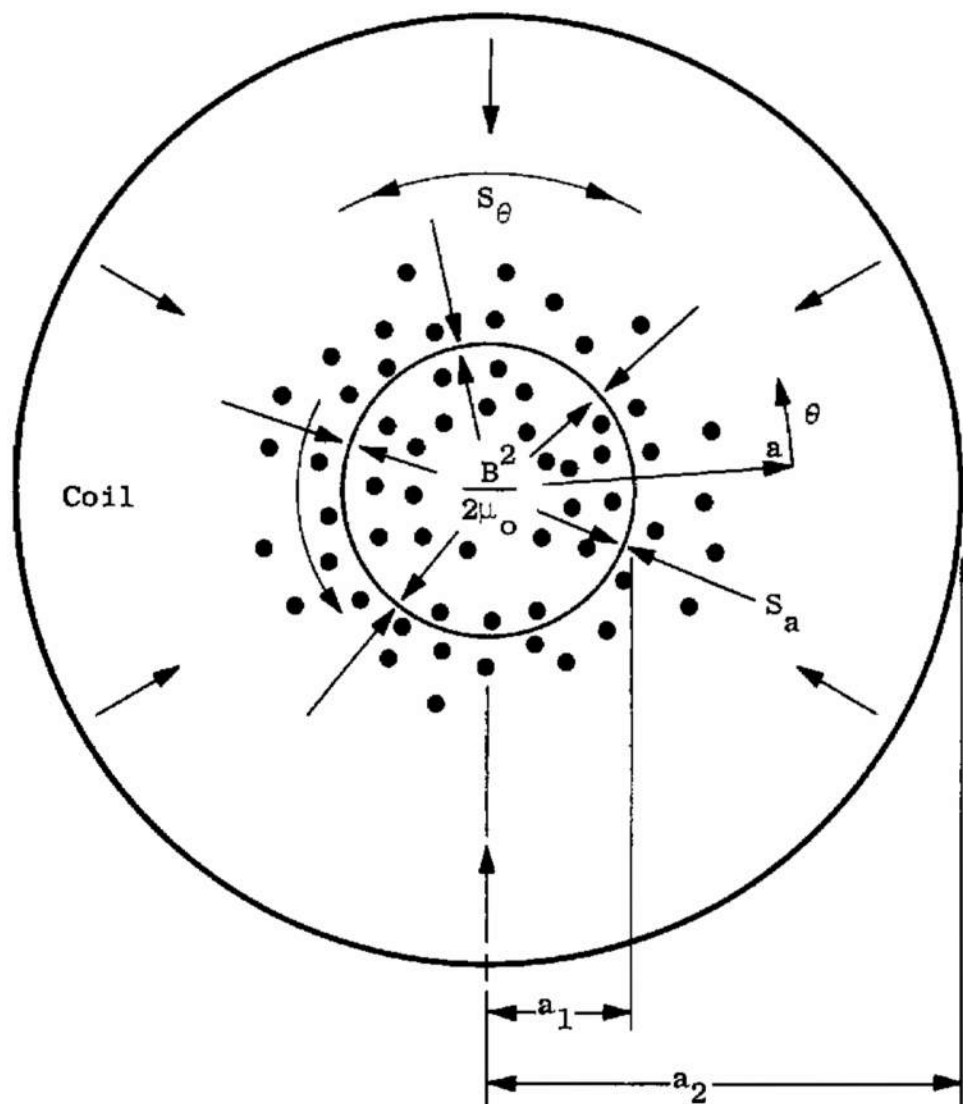


Fig. 47 Typical Electrical Discharge Characteristics of Electric Field System Using Dummy Load



● - Denote Magnetic Field Lines
Perpendicular to Paper

Fig. 48 Magnetic Stresses in a Helical or Single-Turn Coil Caused by Magnetic Pressure

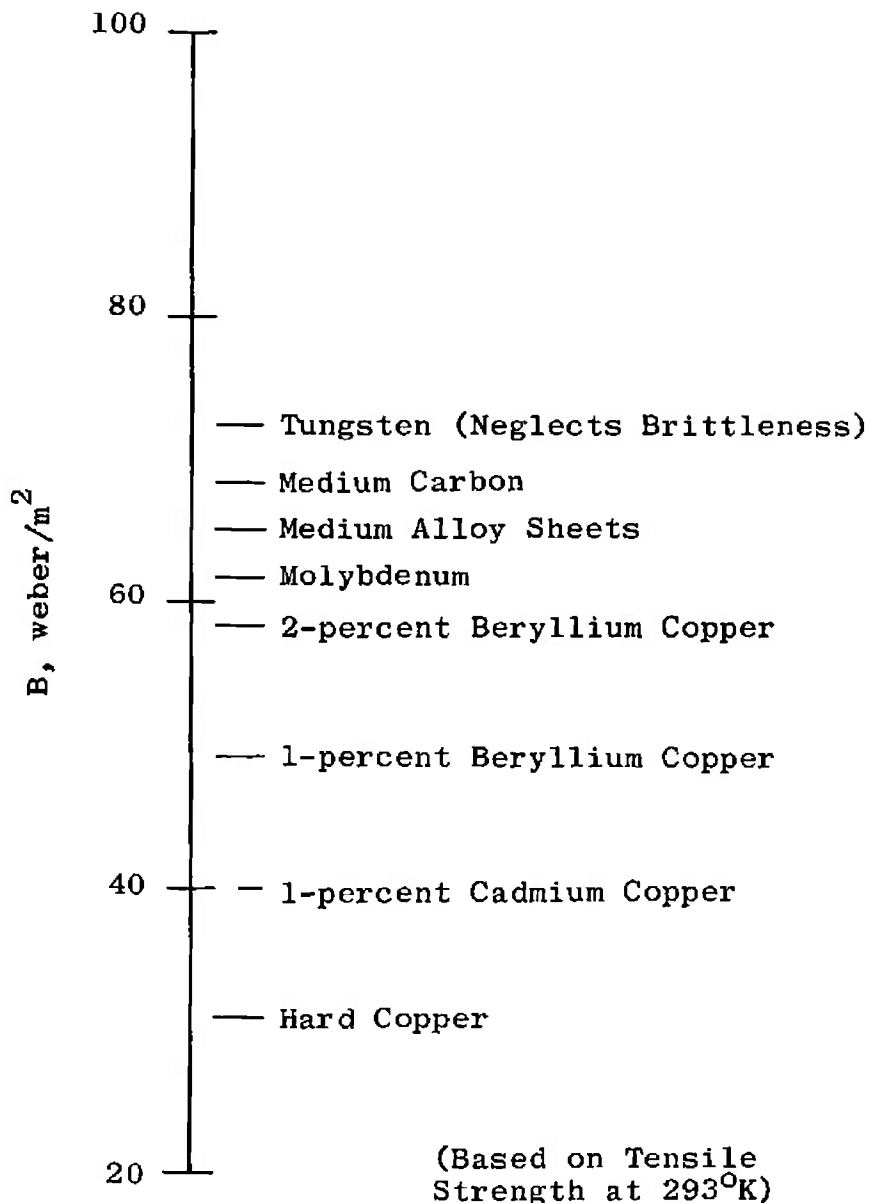


Fig. 49 Maximum Magnetic Field - Limited by Yield Stress of Coil Material - All Coils

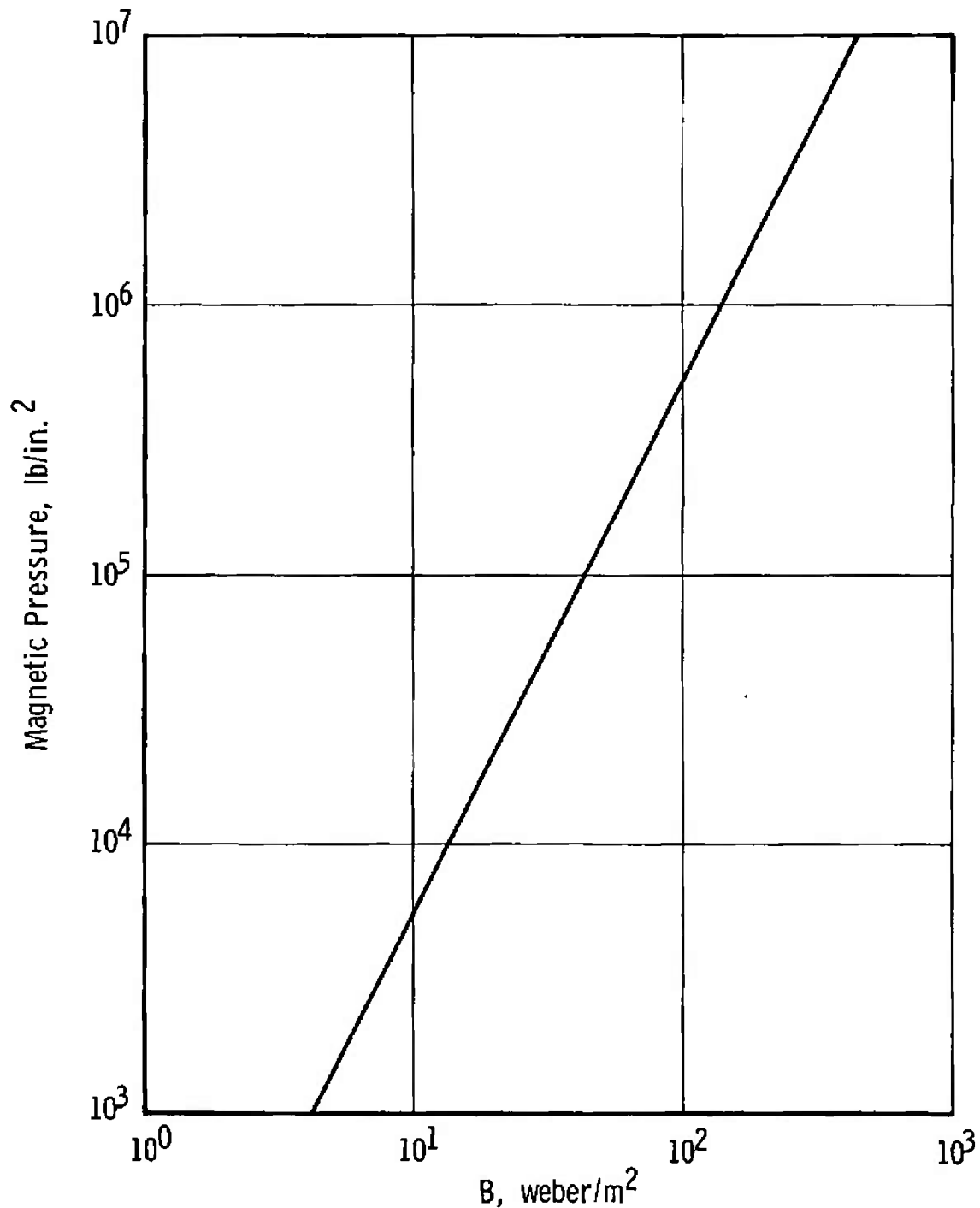


Fig. 50 Magnetic Pressure Developed inside a Coil as a Function of Magnetic Field Level

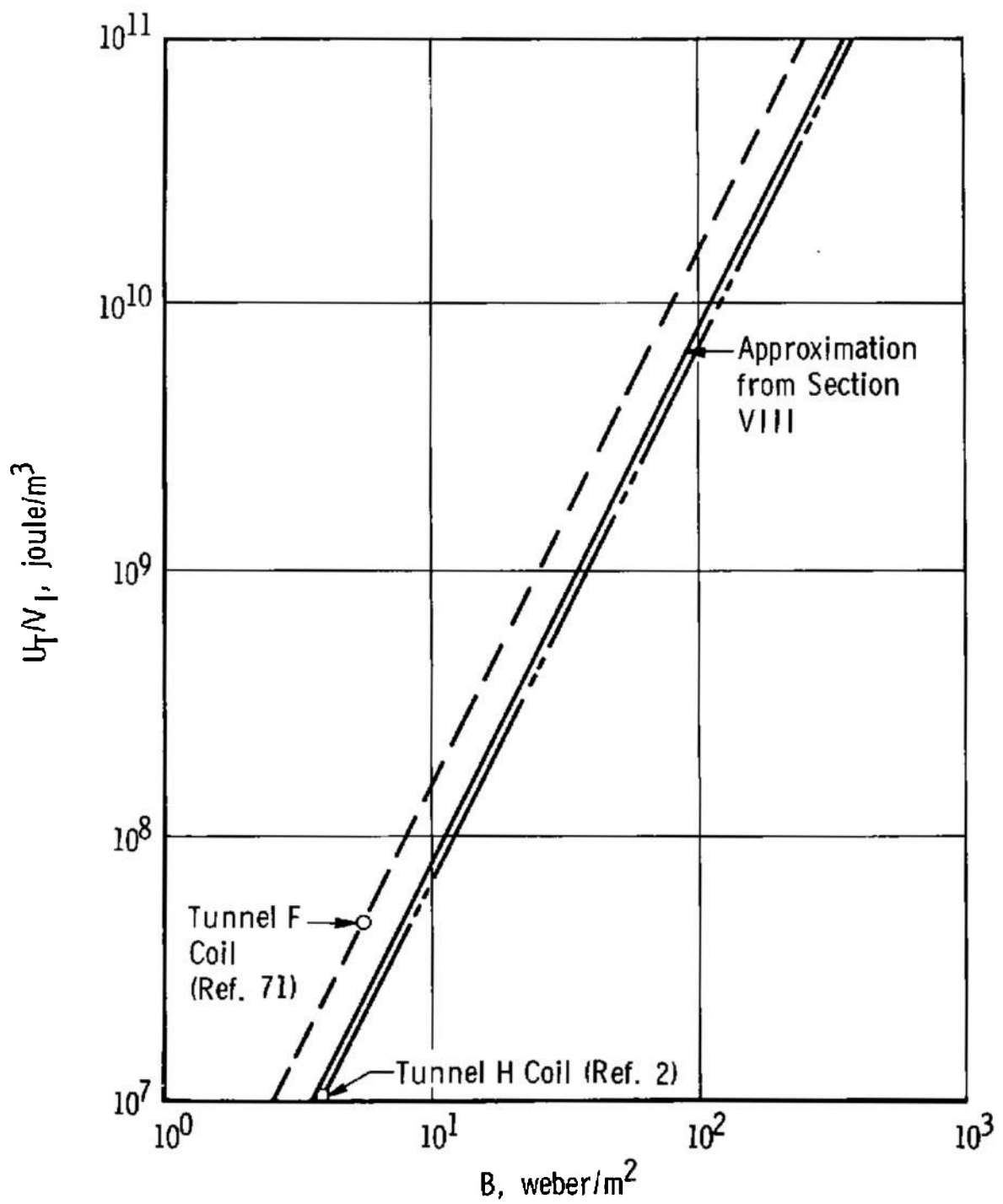


Fig. 51 Total Energy per Unit Inside-Coil-Volume Stored in a Magnetic Field

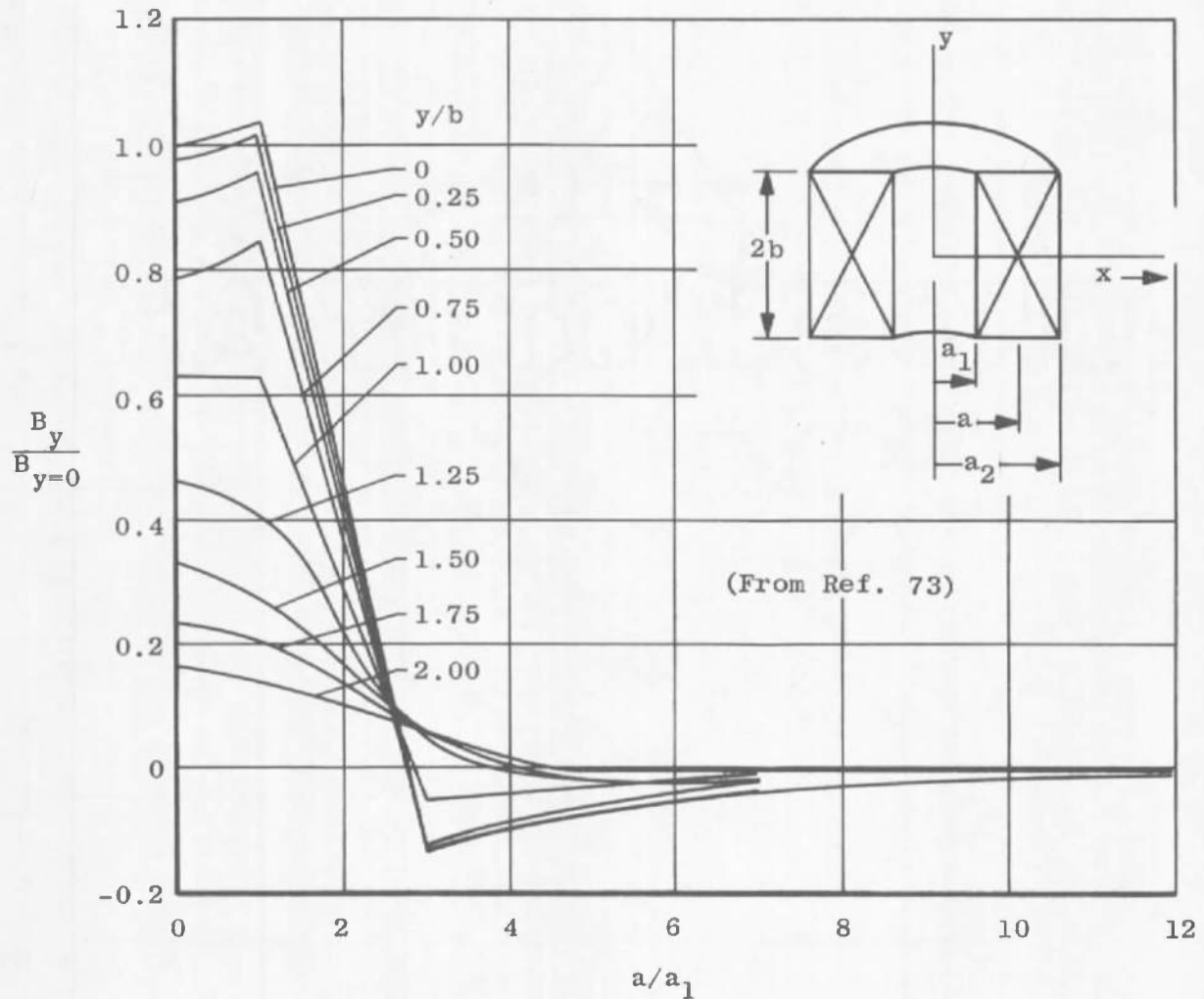
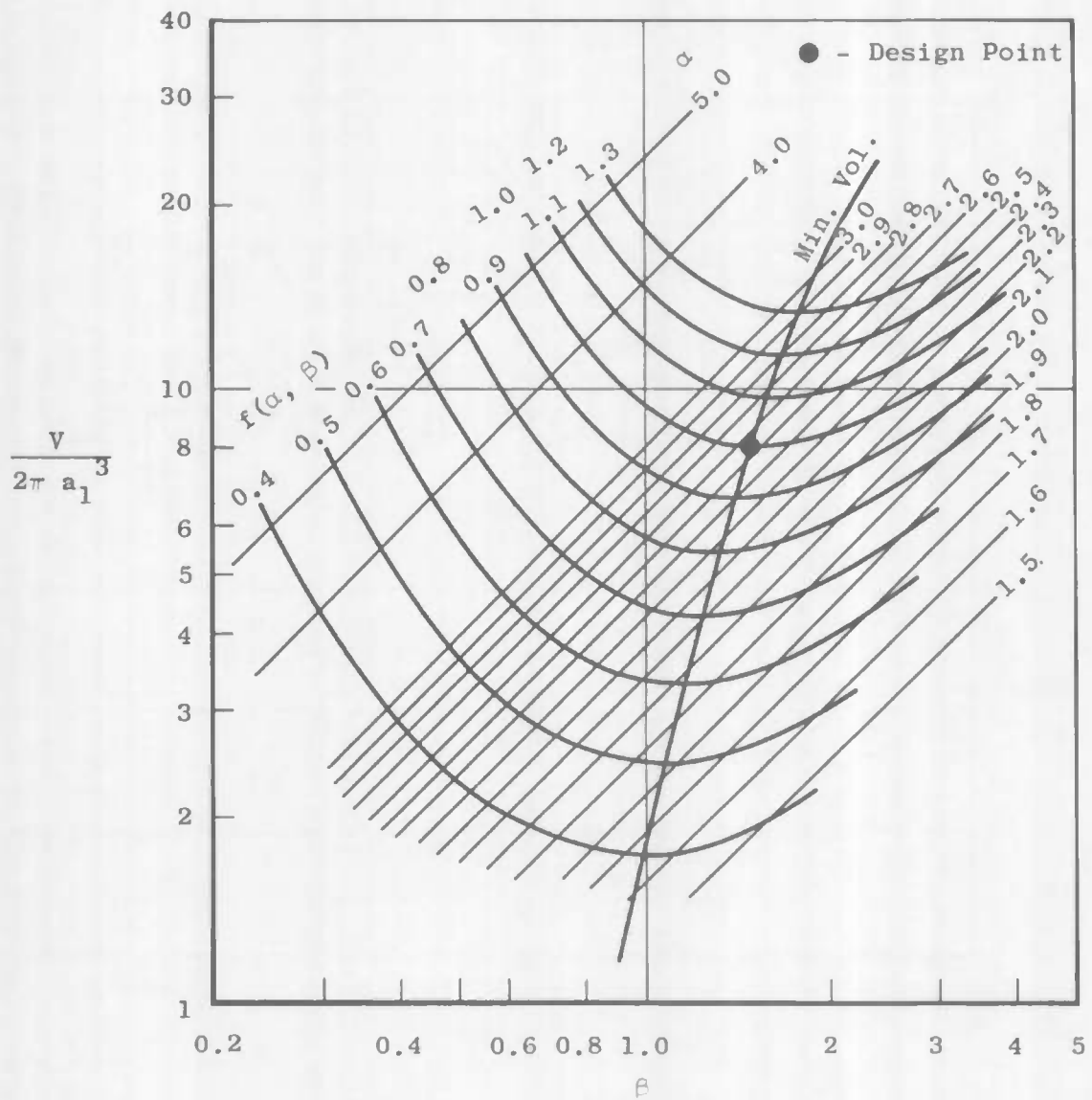


Fig. 52 Dimensionless Axial Field of a Thick Coil, $a = 3$, $\beta = 2$, J Constant with Radius

Fig. 53 Normalized Coil Volume as a Function of β and α

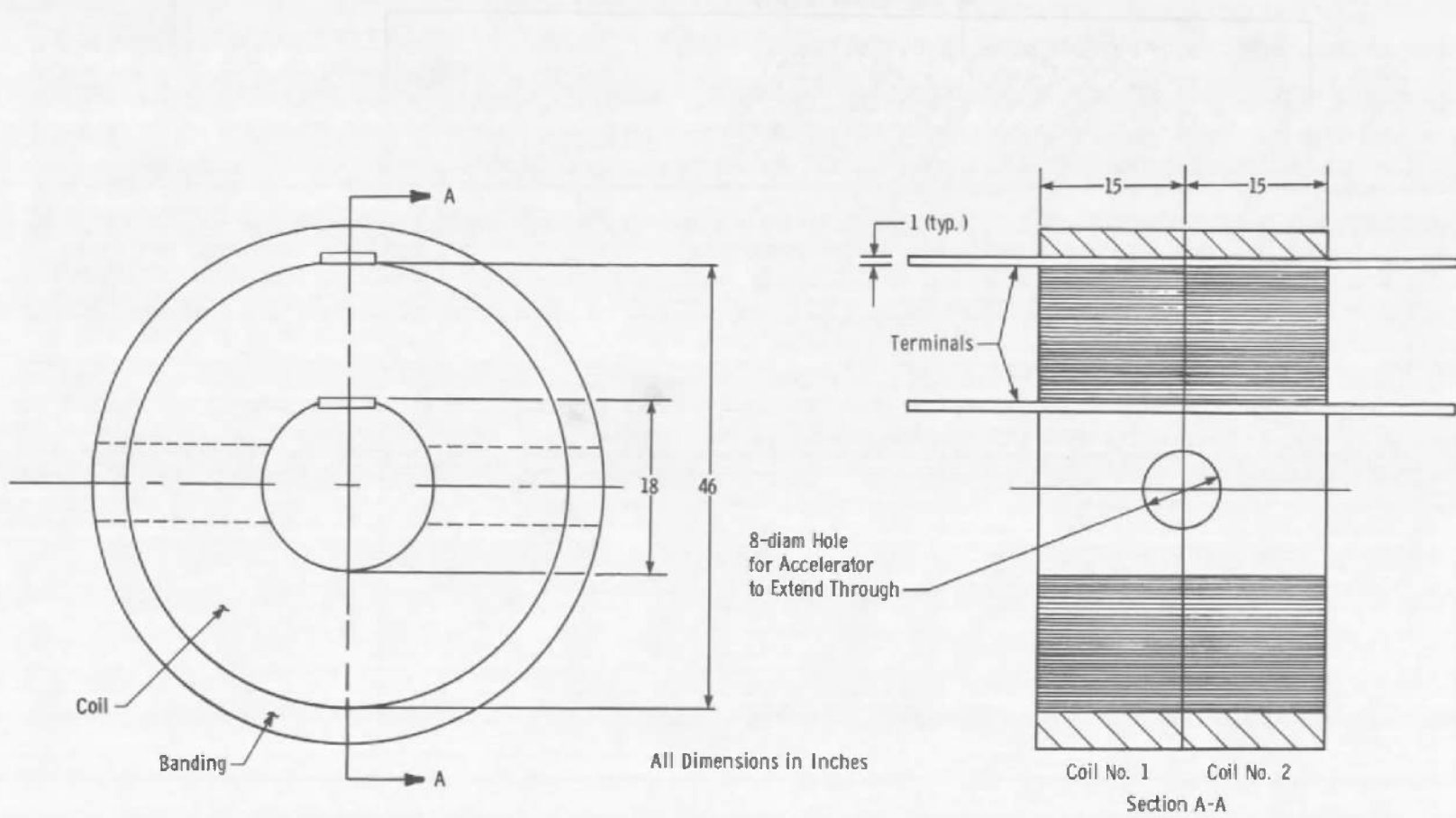
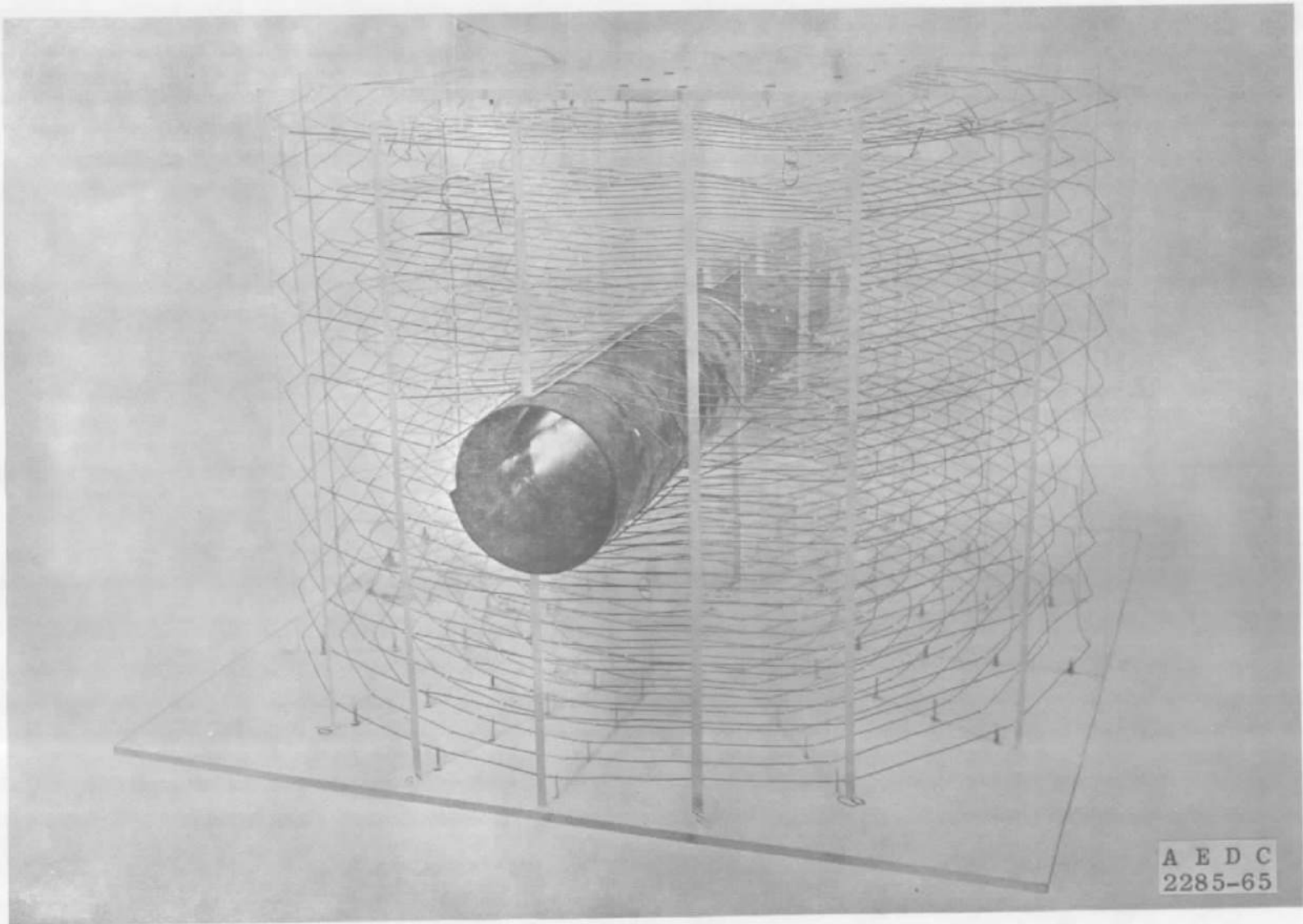


Fig. 54 Drawing of First Coil Design



A E D C
2285-65

Fig. 55 Photograph of Half-Scale Coil Model

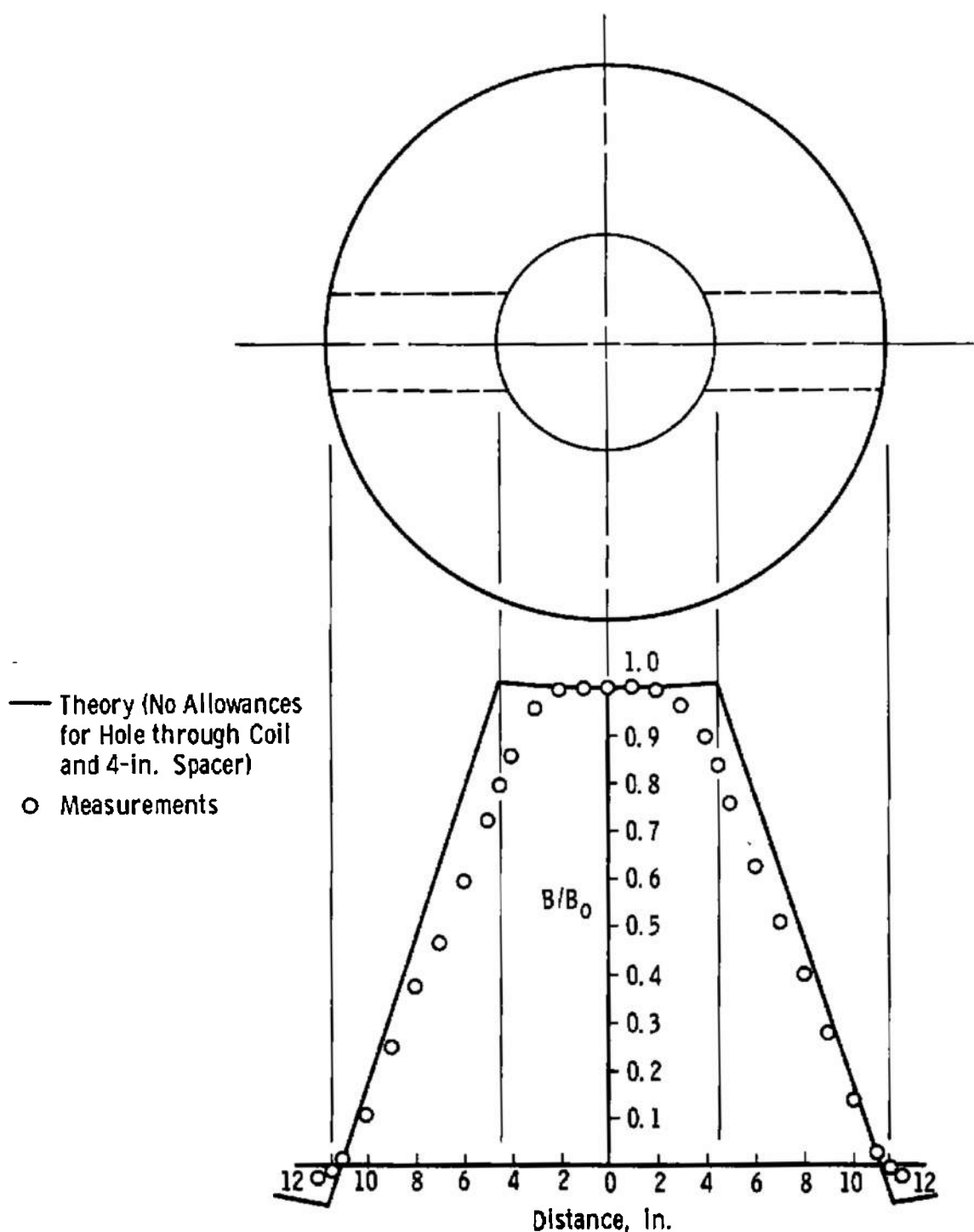


Fig. 56 B-Field Distribution in Half-Size Model

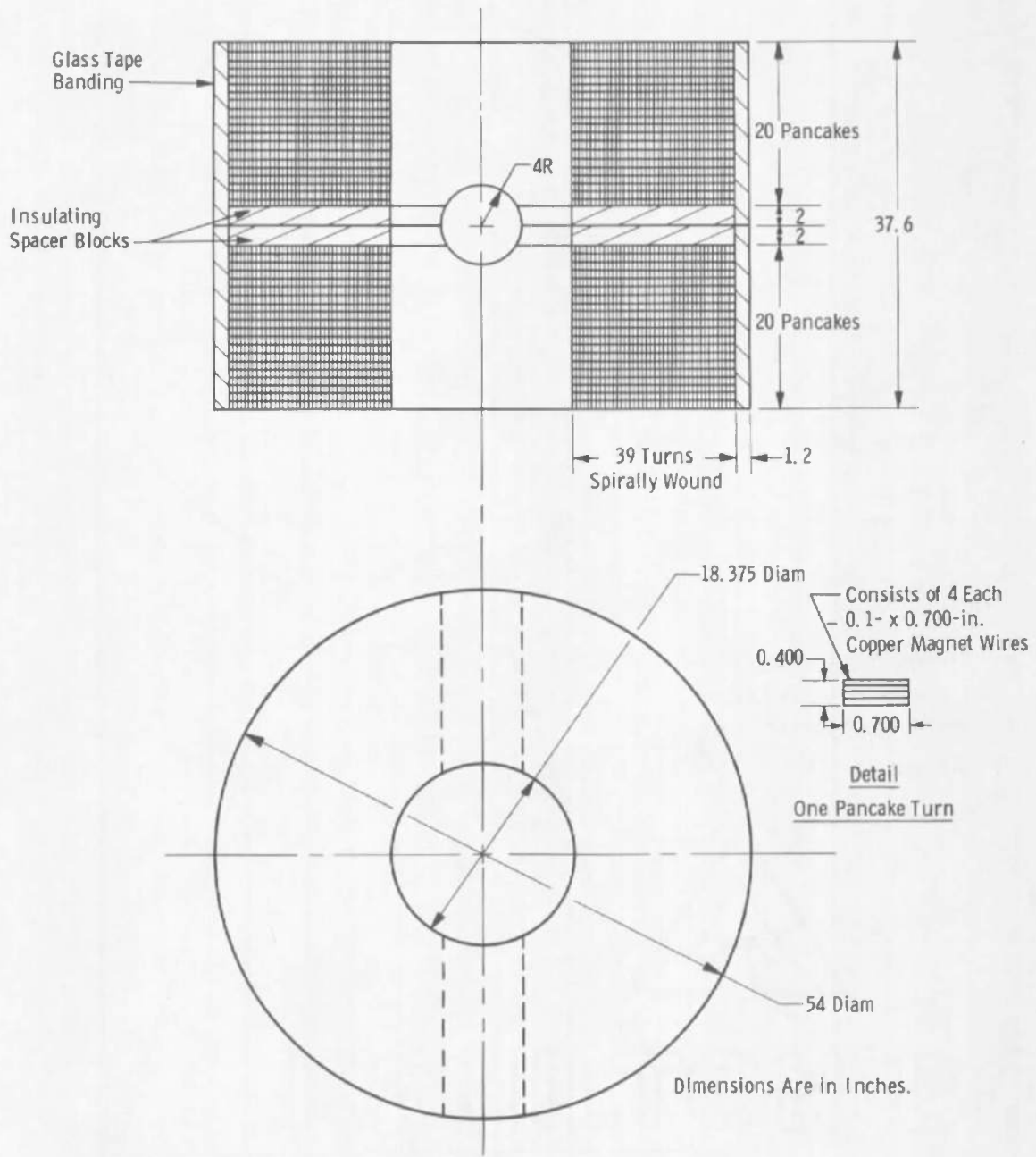
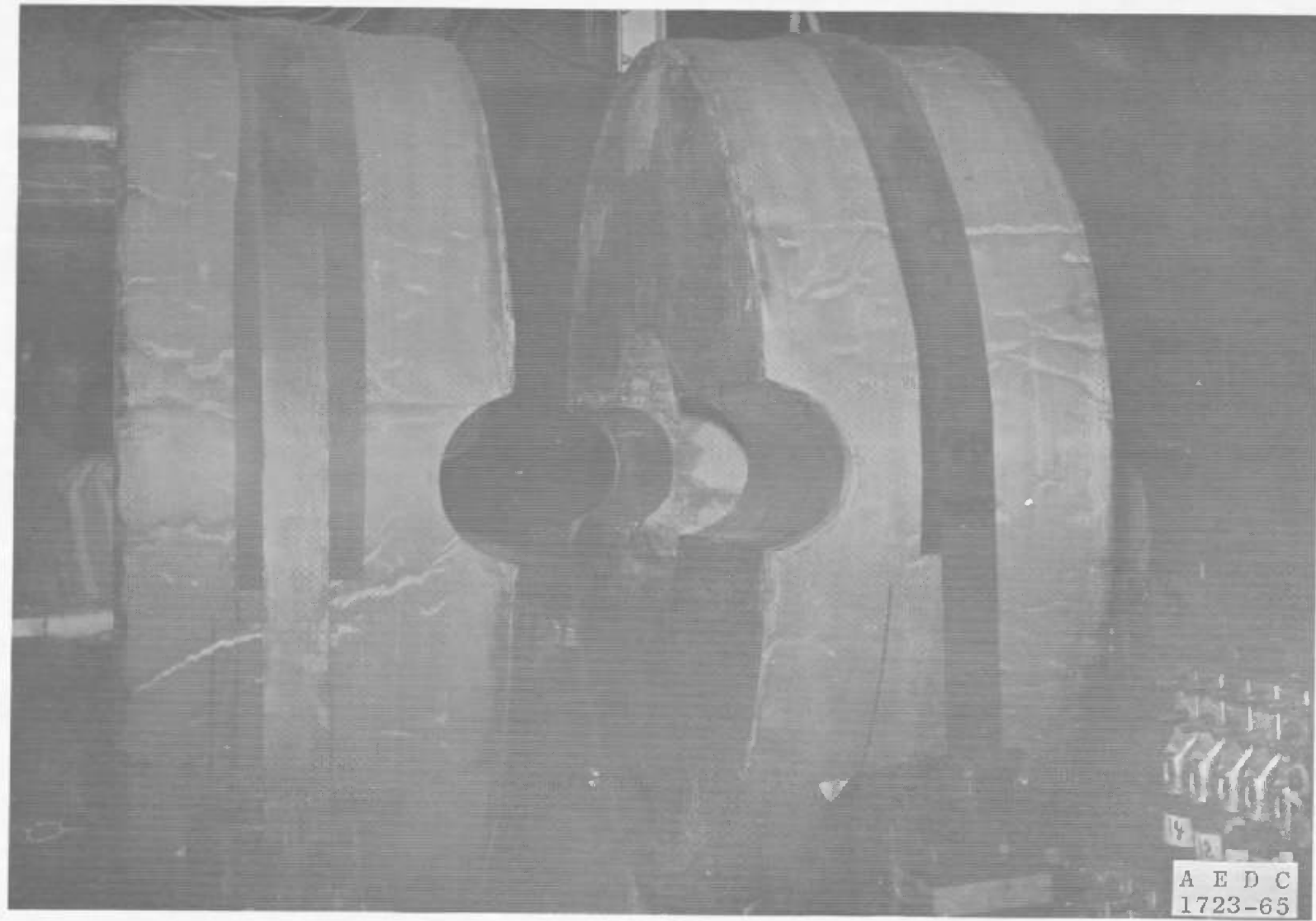


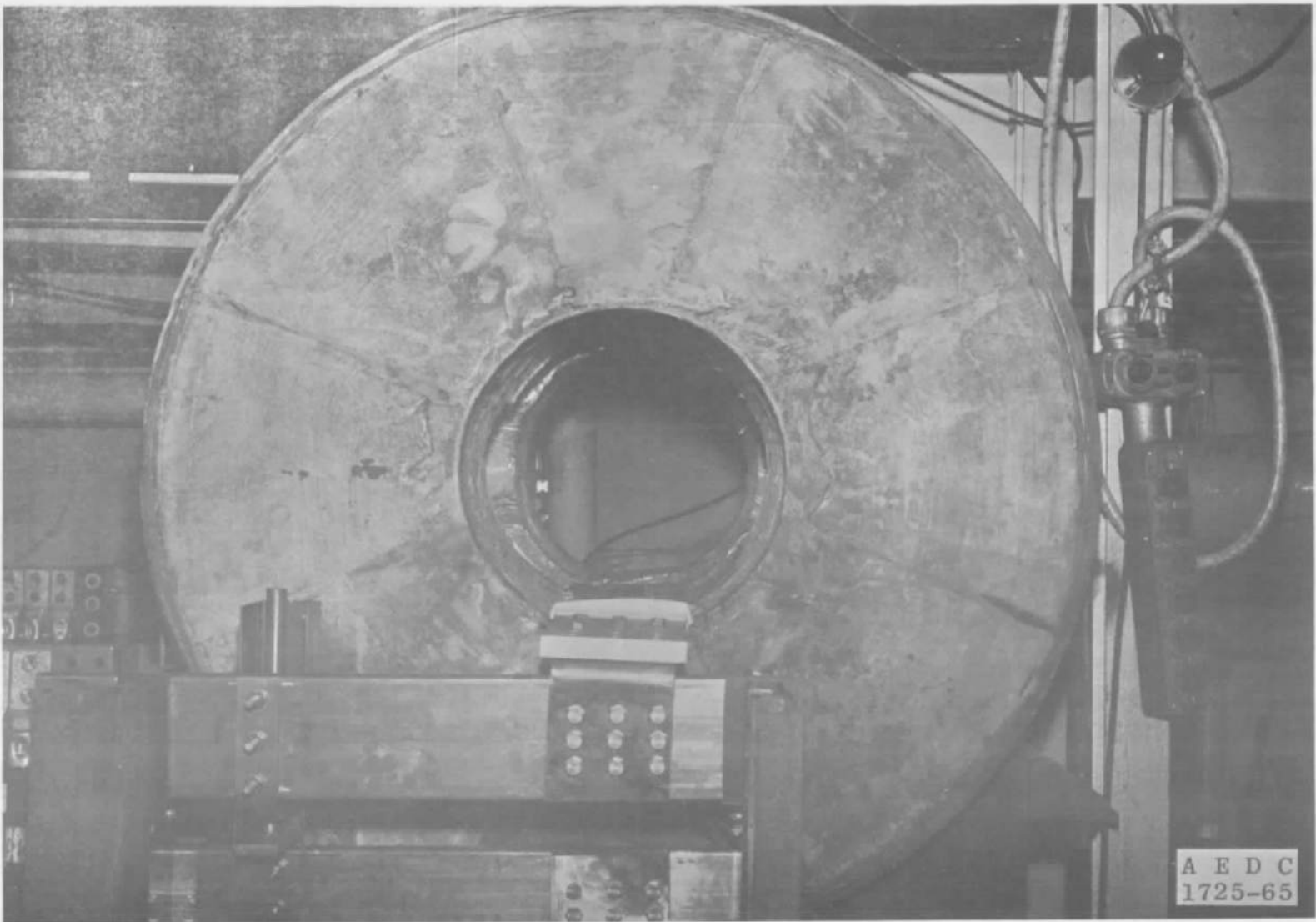
Fig. 57 Drawing of Final Coil Design



A E D C
1723-65

a. Along Tube Axis

Fig. 58 Photographs of Magnetic Field Coil



b. Along Coil Axis

Fig. 58 Concluded

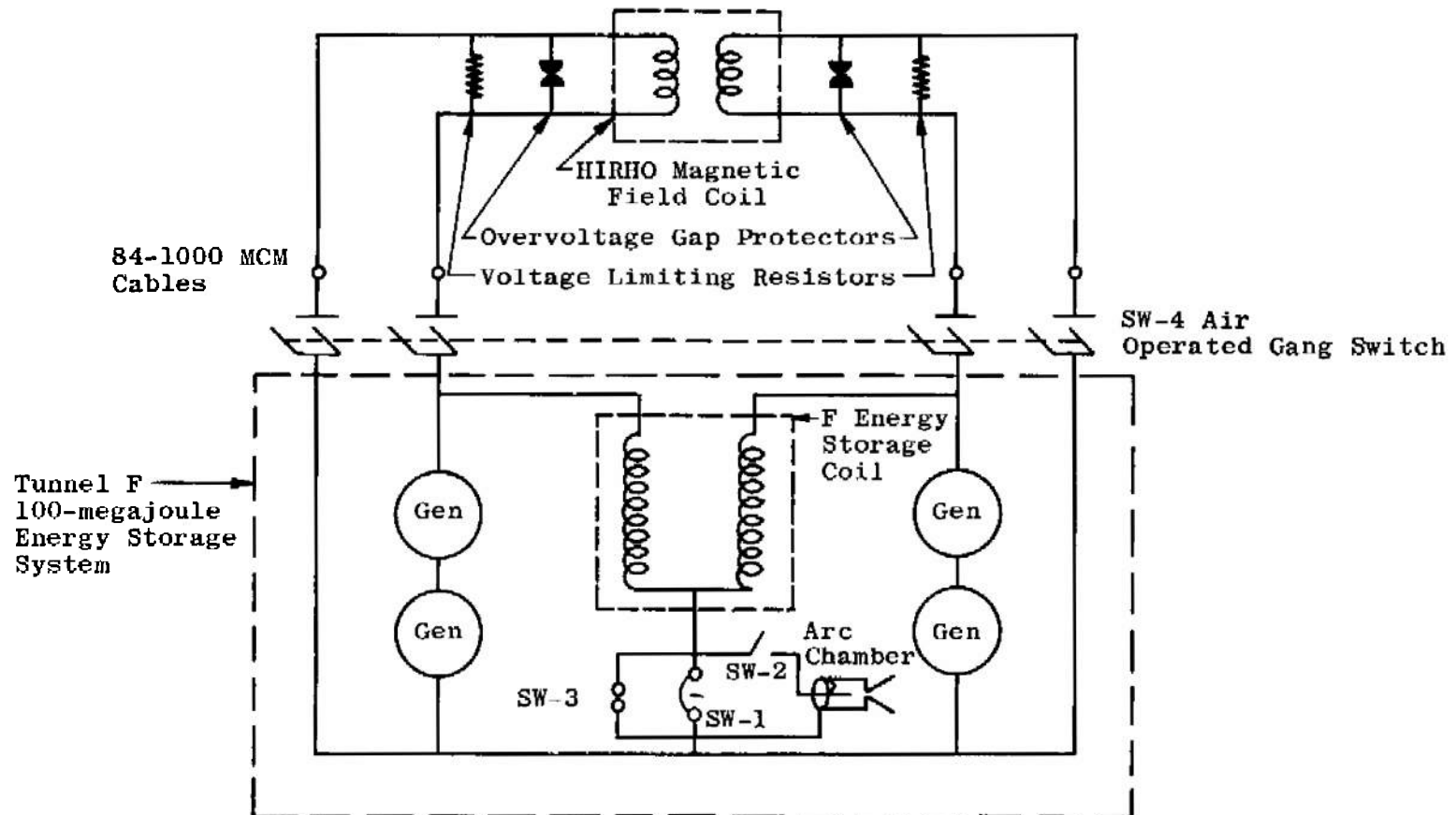
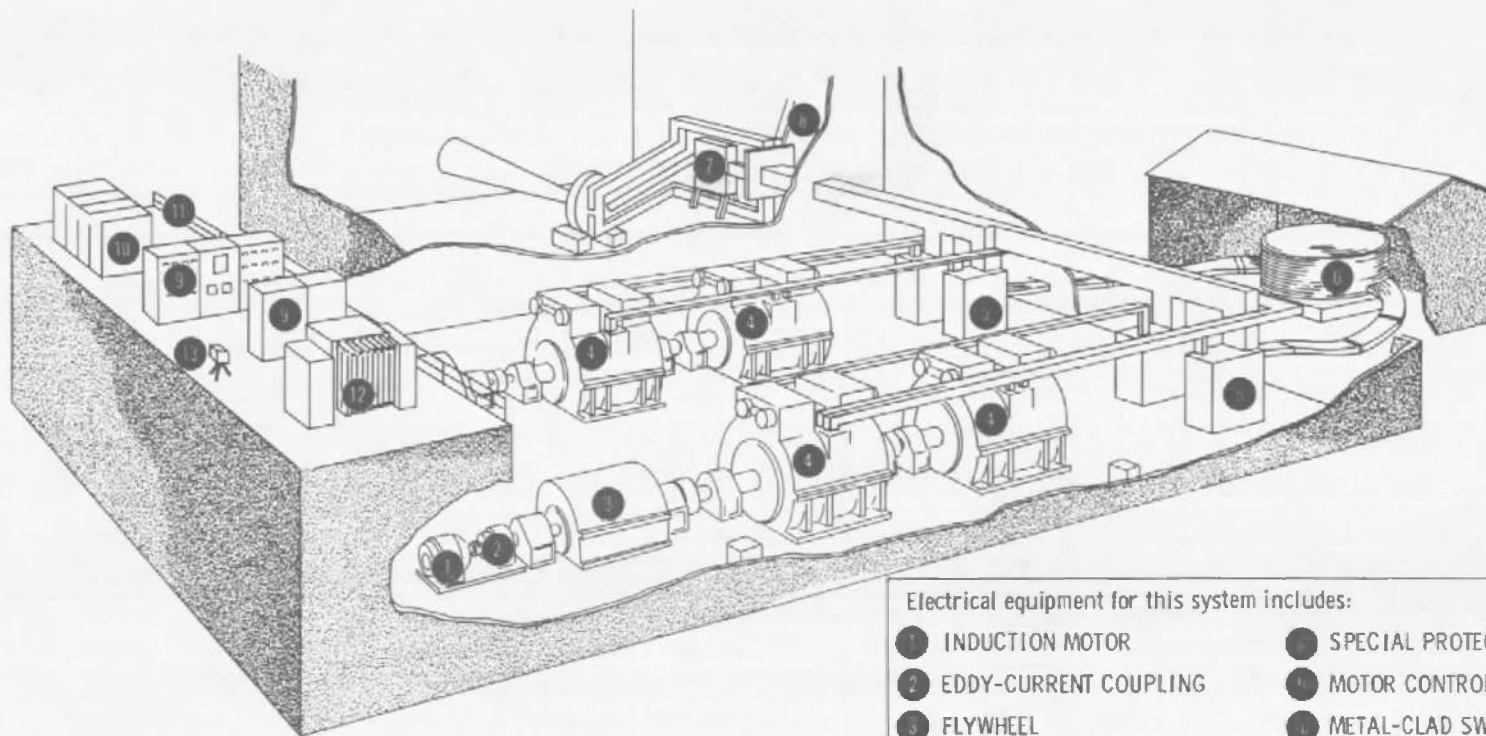


Fig. 59 Electrical Schematic of Magnetic Field System



Electrical equipment for this system includes:

- | | |
|-------------------------|-----------------------------|
| ① INDUCTION MOTOR | ⑧ SPECIAL PROTECTIVE GAP |
| ② EDDY-CURRENT COUPLING | ⑨ MOTOR CONTROL CENTER |
| ③ FLYWHEEL | ⑩ METAL-CLAD SWITCHGEAR |
| ④ ACYCLIC GENERATORS | ⑪ AMPLIDYNE MG SETS |
| ⑤ TRANSFER SWITCHES | ⑫ LOAD CENTER SUBSTATION |
| ⑥ STORAGE COIL | ⑬ CLOSED-CIRCUIT TELEVISION |
| ⑦ LOAD ISOLATING SWITCH | |

Fig. 60 Pictorial Representation of Tunnel F 100-megajoule Inductive Energy Storage System

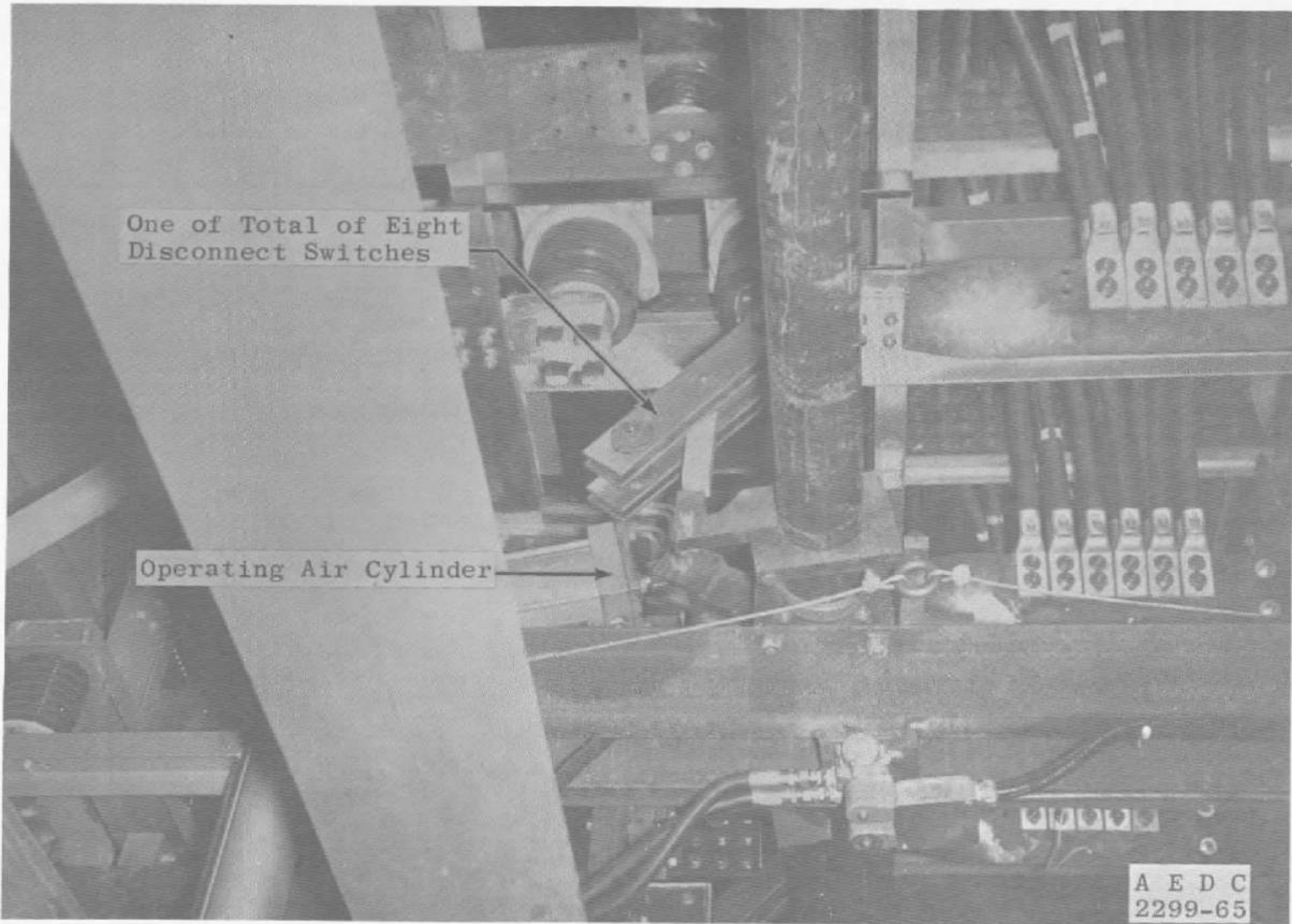


Fig. 61 Photograph of B-Field SW-4 Assembly

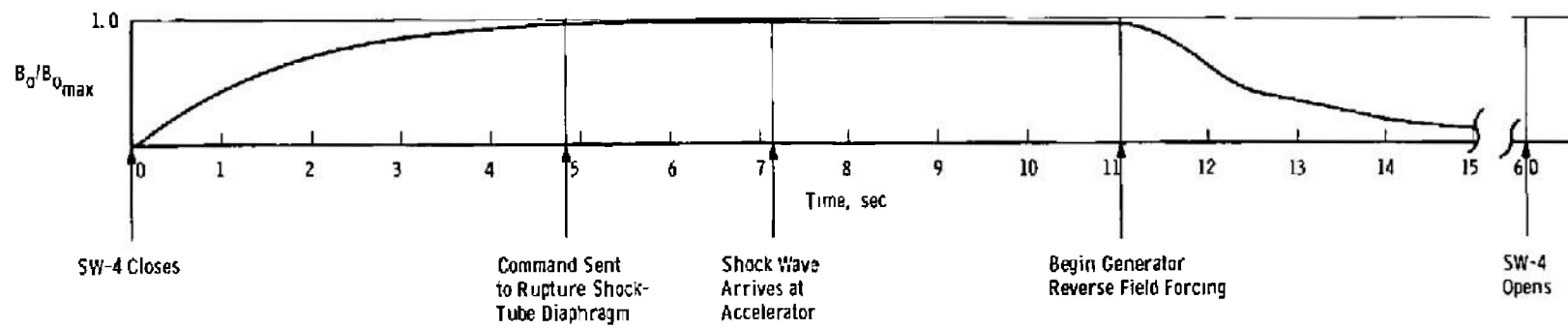


Fig. 62 Typical B-Field Coil Charging – Discharging Cycle

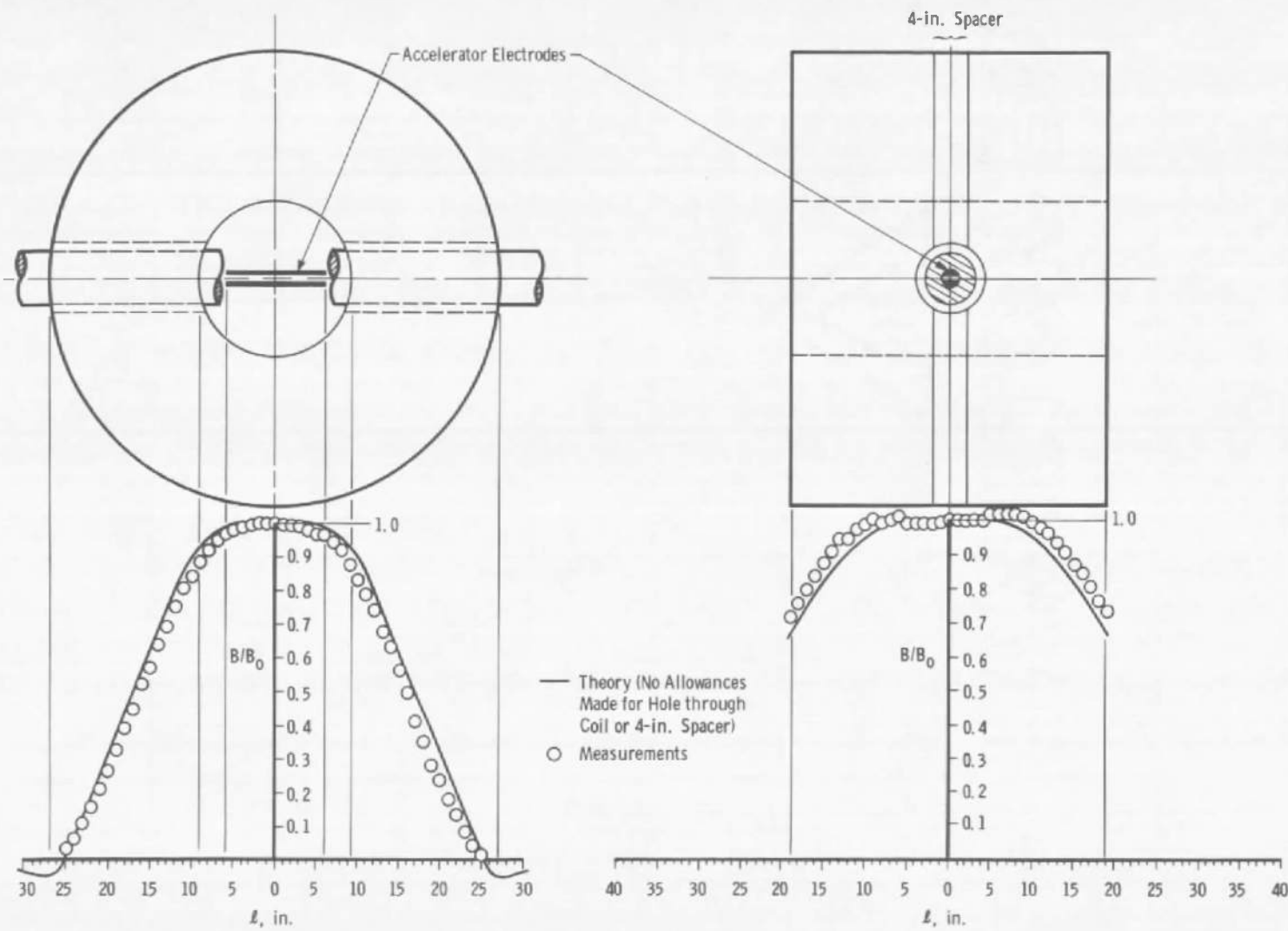


Fig. 63 Comparison of Measured Magnetic Field Distribution to Theory – Final Coil Installation

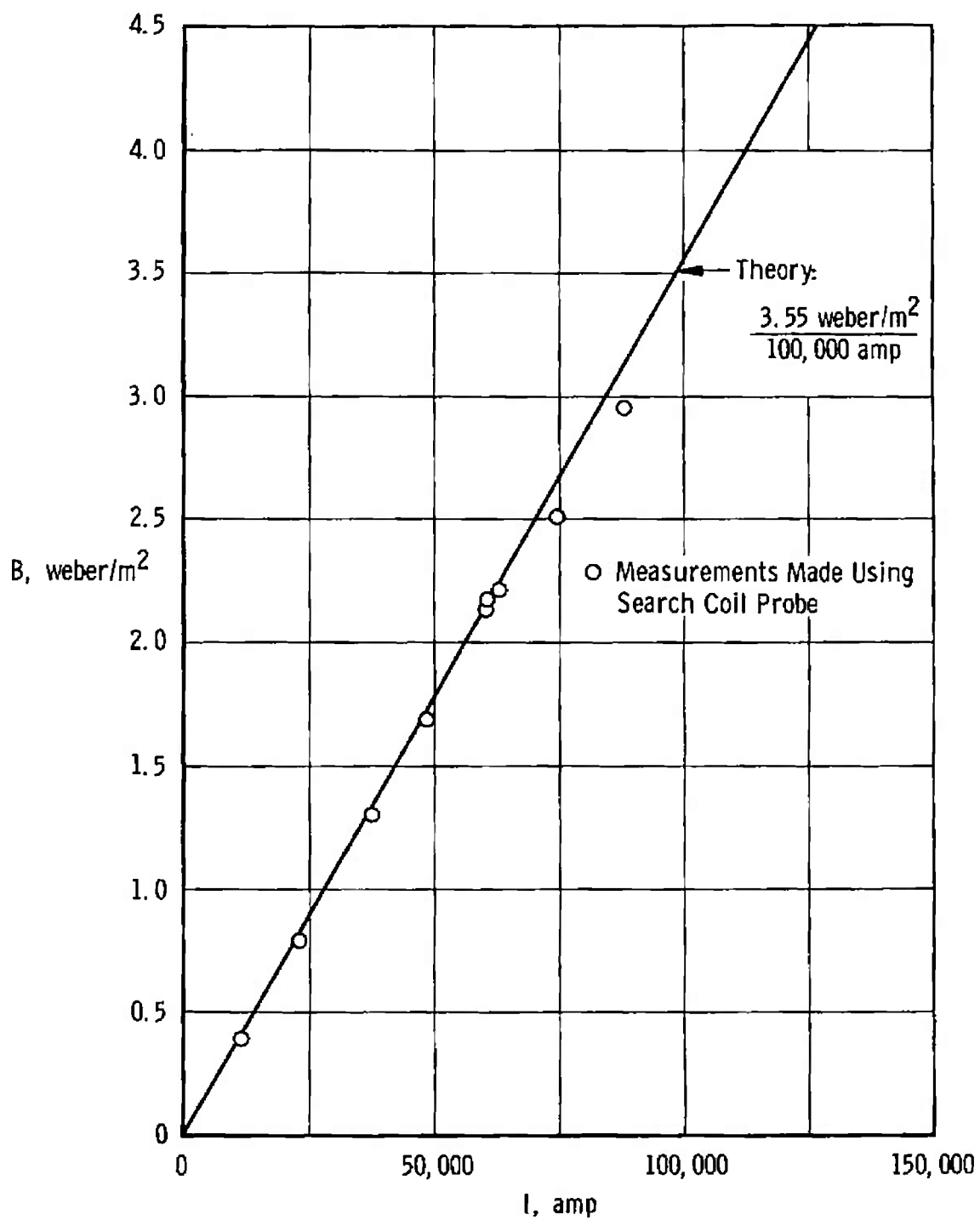


Fig. 63 Concluded

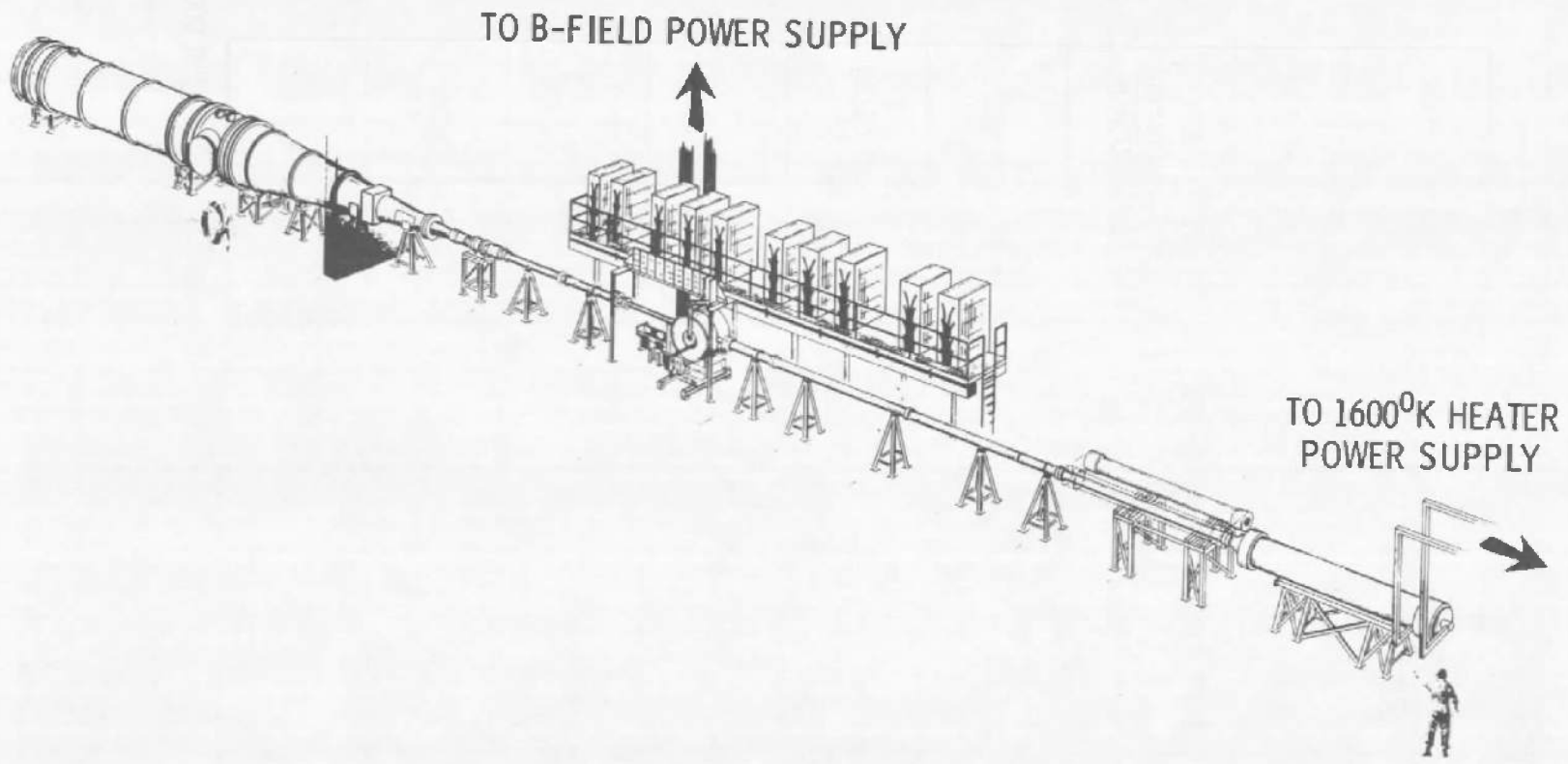


Fig. 64 Research Shock Tunnel System

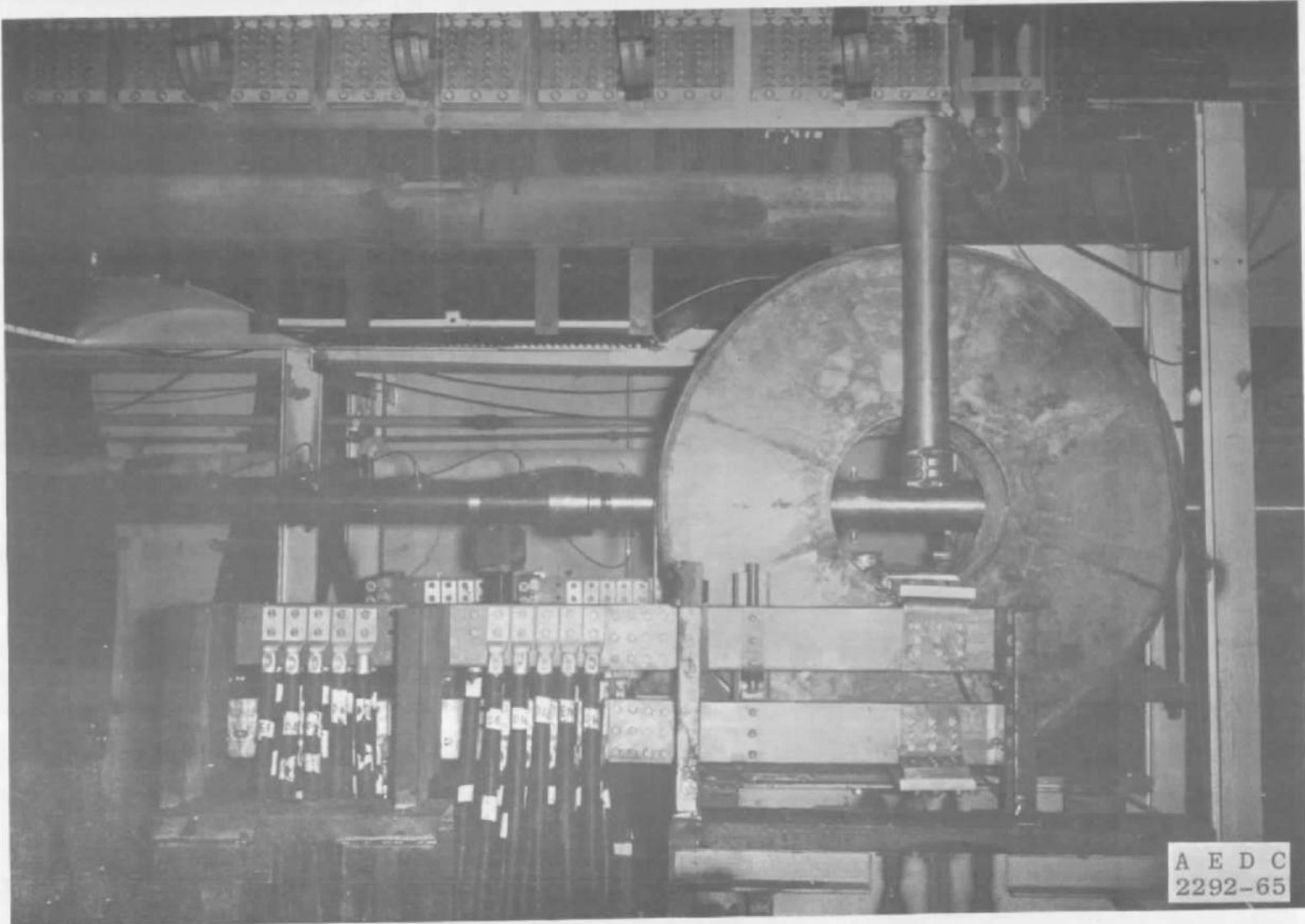


Fig. 65 Photograph of Buffer Accelerator Installation

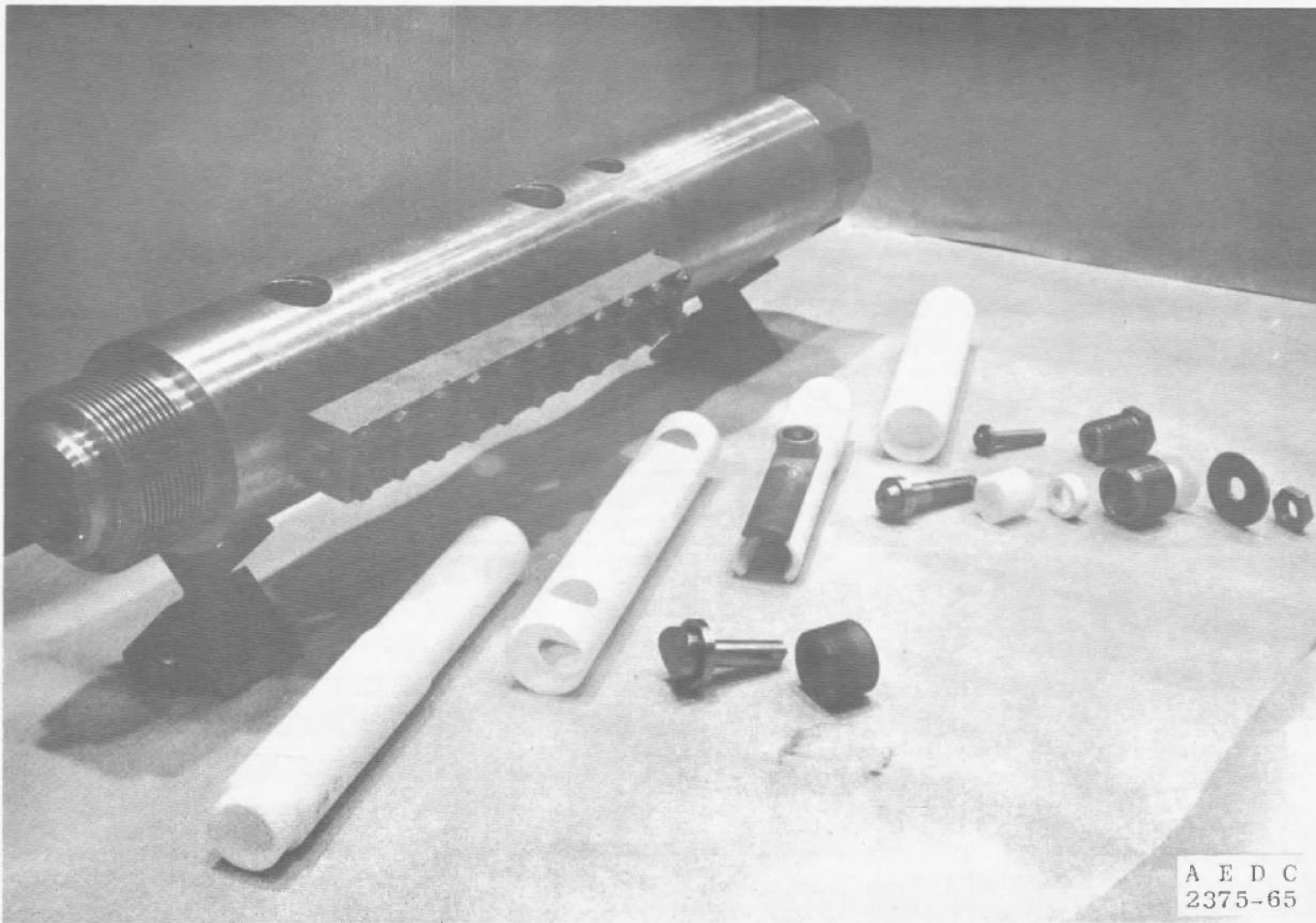


Fig. 66 Photograph of Components of Buffer Accelerator

A E D C
2375-65

AEDC-TR-66-25

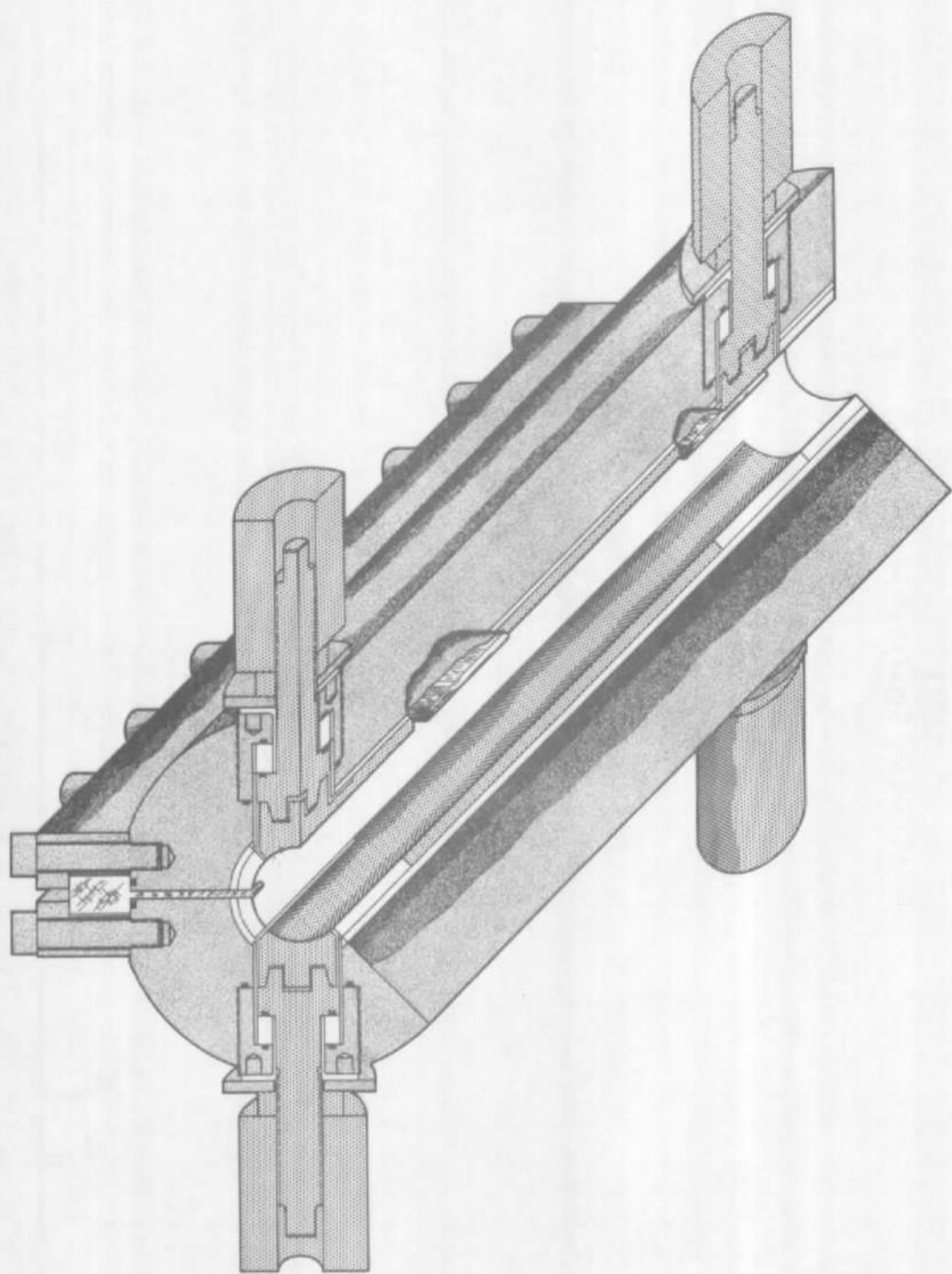


Fig. 67 Cutaway Isometric Drawing of Buffer Accelerator

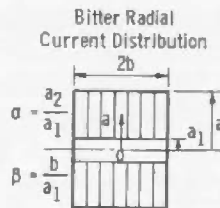
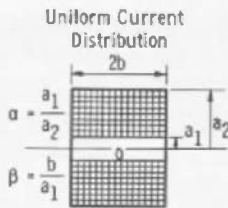
TABLE I
SUMMARY OF D-C COILS IN OPERATION

Name of Laboratory	Field Strength, weber/m ²	Working Opening, cm	Power Consumption, mw	Cooling Method	Supply	Year of Construction	Principal Investigator	Lit. Ref. No.
Univ. in Leiden	6.0	8	1.4	Orthodichlorobenzene	Rectifier	1960	D. de Clerk	52
Los Alamos, USA	8.0	6.3	0.015	Liquid Hydrogen		1959	H. L. Laquer	53
Lyons, France	7.0		1.3	Water	Motor-Generator, 7 ka, 190 v	1958	F. I. Gaum	54
Bell, Murray-Hill, USA	8.8	5	1.5	Water	Motor-Generator	1957	I. F. Kunzler	55
Univ. in Berkeley, USA	10.0	10	7.5	Kerosene	Motor-Generator, 8.5 ka, 700 v	1959	W. F. Giaque	56
Mass. Inst. of Tech., USA	10.0	2.5	1.7	Water	Motor-Generator, 10 ka, 170 v	1939	F. Bitter	69
Research Center in Cleveland, USA	10.0	30	--	Liquid Neon	--	1961	J. C. Lawrence	57
Univ. of Tokyo	12.0	--	3	--	--	Under Construction	S. Maeda	58
Nat'l. Magnetic Lab., Boston, USA	12.6	2.5	1.88	Water in Local-Boiling	Motor-Generator, 10 ka, 170 v	1961	H. Kolm	59
Nat'l. Magnetic Lab., Boston, USA	25.0		8-12	Water in Local-Boiling	Four 2-mw Motor-Generators	Under Construction	F. Bitter	60
NASA, Cleveland Ohio	20.0	30	--	Liquid Neon	Unipolar Gen. 76,000 amp at 30 v	Under Construction	J. C. Lawrence	57

TABLE II
SUMMARY OF PULSE COILS IN OPERATION

Name of Laboratory	Magnetic Field, weber/m ²	Working Opening, cm	Pulse Length, sec	Cooling	Supply	Year of Construction	Principal Investigator	Lit. Ref. No.
Phillips, Holland	10.0	--	2.5×10^{-6}	--	Capacitor, 4 kv, 2 μ f	1961	W. DeBlois	61
GERN	20.0	5	10^{-2}	Oil	Capacitor Bank, 3×10^5 joule	1960	M. Morquo	62
Max Planck Inst., Munich, Germany	30.0		10^{-5}	Inside Liquid N	Capacitor Bank, 3×10^5 joule	1960	H. Bergmann	66
Harvard Univ., USA	60.0	0.45	5×10^{-5}	--	Capacitor Bank, 3 kv, 1725 μ f	1956	H. Furth	40
Moscow State Univ.	65.0	0.45	10^{-4}	--	Capacitor Bank, 3 kv, 1200 μ f	1957	V. R. Karsik	63
Physics Inst., Acad. of Sciences, Moscow, USSR	70.0	0.45	10^{-4}	--	Capacitor Bank, 5 kv, 1000 μ f	1961	V. R. Karsik	63
Mass. Inst. of Tech., USA	75.0	0.45	10^{-4}	--	Capacitor Bank, 2 kv, 3000 μ f	1957	S. Foner H. Kolm	64
Harvard Univ., USA	160.0	0.4	10^{-5}	--	Capacitor Bank, 4 kv, 3000 μ f	1957	H. Furth	40
Los Alamos, USA	1400.0	0.3	2×10^{-6}	--	Energy of Explosion and Capacitor Bank, 20 kv, 7.5 μ f	1960	C. Fowler	43
KOL Leiden, The Netherlands	30.0	0.6	10^{-2}	Liquid H ₂	Capacitor Bank, 5000 joule	1961	J. C. A. van der Sluijs	65
Atm. Wpn. Res. Est. Aldermaston, Eng.	10.0	15.25	1	Liquid N ₂	Bat. 6700 amp at 900 v	1961	S. Skellott	67

TABLE III
SUMMARY OF CURRENT, FIELD, AND POWER RELATIONS FOR DIFFERENT
CURRENT DISTRIBUTIONS



Current Distribution

$$j(a, x) = j_1$$

$$\text{Geometry Factor, } G(\alpha, \beta) \left[\frac{(8\pi \times 10^{-2})\beta}{(\alpha^2 - 1)} \right]^{1/2} \ln \left[\frac{\alpha + (\alpha^2 + \beta^2)^{1/2}}{1 + (1 + \beta)^{1/2}} \right]$$

$$\text{Field Factor, } F(\alpha, \beta) \left[\frac{4\pi}{10} \beta \ln \frac{\alpha + (\alpha^2 + \beta^2)^{1/2}}{1 + (1 + \beta)^{1/2}} \right]$$

$$\text{Field vs Power} \quad B_0 = G(\alpha, \beta) \left(\frac{W\lambda}{\rho a_1} \right)^{1/2} \times 10^{-6}$$

$$\text{Field vs Current Density } B_0 = F(\alpha, \beta) [ja_1 \lambda] \times 10^{-6}$$

Field vs Ampere-Turns

$$B_0 = F(\alpha, \beta) \left[\frac{NI}{2\beta(\alpha - 1)} \right] \times 10^{-6}$$

Resistance

$$R = \frac{N^2 \rho}{\lambda a_1} \frac{\pi(\alpha + 1)}{(\alpha - 1) 2\beta}$$

$$j(a, x) = \frac{j_1 a_1}{a}$$

$$\left[\frac{4\pi \times 10^{-2}}{\beta \ln \alpha} \right]^{1/2} \ln \left[\frac{\beta + (1 + \beta)^{1/2}}{\beta + (\alpha^2 + \beta^2)^{1/2}} \right]$$

$$[4\pi \beta \ln \alpha]^{1/2} G(\alpha, \beta)$$

$$B_0 = G(\alpha, \beta) \left(\frac{W\lambda}{\rho a_1} \right)^{1/2}$$

$$B_0 = F(\alpha, \beta) [ja_1 \lambda] \times 10^{-6}$$

$$B_0 = F(\alpha, \beta) \left[\frac{NI}{2\beta(\alpha - 1)} \right] \times 10^{-6}$$

$$R = \frac{N^2 \rho}{\lambda a_1} \frac{\pi}{\beta \ln \alpha}$$

TABLE III (Concluded)

	Gauze Current Distribution	Kelvin Current Distribution
	 $\alpha = \frac{a_2}{a_1}$ $\beta = \frac{b}{a_1}$ $\gamma = \frac{x}{a_1}$	 $\alpha = \frac{a_2}{a_1}$ $\beta = \frac{b}{a_1}$ $\gamma = \frac{x}{a_1}$
Current Distribution	$j(a, x) = j_1 \frac{a_1}{a} \left[\left(\frac{1}{\gamma^2 + 1} \right)^{1/2} - \left(\frac{1}{\gamma^2 + \alpha^2} \right)^{1/2} \right] \left(\frac{\alpha}{\alpha - 1} \right)$	$j(a, x) = j_1 \left[\frac{a/a_1}{[(a/a_1)^2 + \gamma^2]^{3/2}} \right]$
Geometry Factor, $G(\alpha, \beta)$	$\left[\frac{4\pi \times 10^{-2}}{2\ln \alpha} \right]^{1/2} \left[\tan^{-1} \beta + \frac{1}{\alpha} \tan^{-1} \frac{\beta}{\alpha} - 2F(\phi, K) \right]^{1/2}$	$\left[(5\pi \times 10^{-3})^{1/2} \right] \left[\left(\frac{1}{1 + \beta^2} - \frac{\beta}{\alpha^2 + \beta^2} \right) - 3 \left(\frac{1}{\alpha} \tan^{-1} \frac{\beta}{\alpha} - \tan^{-1} \beta \right) \right]^{1/2}$
	$F(\phi, K) = \text{Elliptic of 1st kind}$ $\phi = \tan^{-1} \beta, K = \alpha^2 - 1/\alpha$	
Field Factor, $F(\alpha, \beta)$	$\left\{ \frac{10a \ln \alpha}{\alpha - 1} [G(\alpha, \beta)]^2 \right\}$	-----
Field vs Power	$B_0 = G(\alpha, \beta) \left(\frac{W\lambda}{\rho a_1} \right)^{1/2}$	$B_0 = G(\alpha, \beta) \left(\frac{W\lambda}{\rho a_1} \right)^{1/2}$
Field vs Current Density	$B_0 = F(\alpha, \beta) [j a_1 \lambda] \times 10^{-6}$	-----
Field vs Ampere-Turns	$B_0 = F(\alpha, \beta) \left\{ (N/I) / \left[20(\alpha - 1) \right] \right\} \times 10^{-6}$	-----
Resistance	$R = (a_1 \rho) N_e^2 \lambda \left\{ [(10a \lambda)/a - 1][G(\alpha, \beta)] \right\}^2$	-----
	$N_e = \text{number of turns}$ $\lambda = \text{thickness of center turn in meters}$	

TABLE IV
COIL DATA

	First Design	Final Design
$B_{0\max}$, weber/m ²	10.6	9.91
i_{\max} , amp	255,000	280,000
v_{\max} , v	66.9	74.2
R_{\max} , microhm	262.5	265
L , microhenry	555	520
J_{\max} , amp/in. ²	25,000	25,000
Number of Turns	37	39
A_{turn} , in. ²	11.34	11.2
ΔT_{\max} , °F/10-sec Pulse	125	125
Coil Dimensions		
I. D., in.	18.0	18.375
O. D., in. (Less Banding)	46.0	50.5
Width, in.	30.0	37.6
$\alpha = a_2/a_1$	2.55	2.76
$\beta = b/a_1$	1.67	2.05
$f(\alpha, \beta)$	1.06	1.086
λ	0.9	0.803
Conductor Material	Copper	Copper
Conductor Shape	Sheet	Magnet Wire
Banding Material	Glass Tape	Glass Tape

UNCLASSIFIED

Security Classification

DOCUMENT CONTROL DATA - R&D

(Security classification of title, body of abstract and indexing annotation must be entered when the overall report is classified)

1 ORIGINATING ACTIVITY (Corporate author) Arnold Engineering Development Center ARO, Inc., Operating Contractor Arnold Air Force Station, Tennessee		2a REPORT SECURITY CLASSIFICATION UNCLASSIFIED
		2b GROUP N/A
3 REPORT TITLE STATUS OF RESEARCH ON MAGNETOHYDRODYNAMIC AUGMENTATION OF A SHOCK TUNNEL		
4 DESCRIPTIVE NOTES (Type of report and inclusive dates) N/A		
5 AUTHOR(S) (Last name, first name, initial) Wendell Norman and R. R. Walker, III, ARO, Inc.		
6 REPORT DATE May 1966		7a TOTAL NO OF PAGES 146
8a CONTRACT OR GRANT NO AF40(600)-1200		7b NO OF REFS 73
b PROJECT NO 7778		9a ORIGINATOR'S REPORT NUMBER(S) AEDC-TR-66-25
c Program Element 62410034		9b OTHER REPORT NO(S) (Any other numbers that may be assigned this report) N/A
d Task 777806		
10 AVAILABILITY/LIMITATION NOTICES Qualified users may obtain copies of this report from DDC. Report is subject to special export controls and each transmittal to foreign govts. or nat'l's. needs approval of AEDC		
11 SUPPLEMENTARY NOTES N/A		12. SPONSORING MILITARY ACTIVITY Arnold Engineering Development Center, Air Force Systems Command, Arnold AF Station, Tennessee
13 ABSTRACT Two concepts for the augmentation of shock tunnel performance are analyzed. In the first of these, termed the buffer accelerator, a magnetohydrodynamic (MHD) accelerator is used to accelerate a buffer gas, which in turn drives a shock into the test gas. In the second approach, termed the nozzle accelerator, an MHD accelerator is used to accelerate the test gas directly. The latter approach is shown to be capable of providing higher velocities and longer test times, but the aerodynamic quality of the resulting test gas suffers because of the necessity of adding seed material to develop the conductivity required for accelerator operation. Descriptions are given of the major pieces of equipment that have been built for an experimental program to investigate the two augmentation concepts. These are (1) a 10^6 -joule capacitor bank for the electric field, (2) a $10\text{-weber}/\text{m}^2$ coil for the magnetic field, and (3) a buffer accelerator.		

UNCLASSIFIED

Security Classification

14	KEY WORDS	LINK A		LINK B		LINK C	
		ROLE	WT	ROLE	WT	ROLE	WT
1	magnetohydrodynamics						
2 MHD	accelerators						
3	shock tunnels						
	performance						
	augmentation						
	seeding						
4	capacitor banks						
	coils						
5	buffer accelerators						
6.	MHD augmentation						

INSTRUCTIONS

1. ORIGINATING ACTIVITY: Enter the name and address of the contractor, subcontractor, grantee, Department of Defense activity or other organization (**corporate author**) issuing the report.

2a. REPORT SECURITY CLASSIFICATION: Enter the overall security classification of the report. Indicate whether "Restricted Data" is included. Marking is to be in accordance with appropriate security regulations.

2b. GROUP: Automatic downgrading is specified in DoD Directive 5200.10 and Armed Forces Industrial Manual. Enter the group number. Also, when applicable, show that optional markings have been used for Group 3 and Group 4 as authorized.

3. REPORT TITLE: Enter the complete report title in all capital letters. Titles in all cases should be unclassified. If a meaningful title cannot be selected without classification, show title classification in all capitals in parenthesis immediately following the title.

4. DESCRIPTIVE NOTES: If appropriate, enter the type of report, e.g., interim, progress, summary, annual, or final. Give the inclusive dates when a specific reporting period is covered.

5. AUTHOR(S): Enter the name(s) of author(s) as shown on or in the report. Enter last name, first name, middle initial. If military, show rank and branch of service. The name of the principal author is an absolute minimum requirement.

6. REPORT DATE: Enter the date of the report as day, month, year, or month, year. If more than one date appears on the report, use date of publication.

7a. TOTAL NUMBER OF PAGES: The total page count should follow normal pagination procedures, i.e., enter the number of pages containing information.

7b. NUMBER OF REFERENCES: Enter the total number of references cited in the report.

8a. CONTRACT OR GRANT NUMBER: If appropriate, enter the applicable number of the contract or grant under which the report was written.

8b, 8c, & 8d. PROJECT NUMBER: Enter the appropriate military department identification, such as project number, subproject number, system numbers, task number, etc.

9a. ORIGINATOR'S REPORT NUMBER(S): Enter the official report number by which the document will be identified and controlled by the originating activity. This number must be unique to this report.

9b. OTHER REPORT NUMBER(S): If the report has been assigned any other report numbers (either by the originator or by the sponsor), also enter this number(s).

10. AVAILABILITY/LIMITATION NOTICES: Enter any limitations on further dissemination of the report, other than those

imposed by security classification, using standard statements such as:

- (1) "Qualified requesters may obtain copies of this report from DDC."
- (2) "Foreign announcement and dissemination of this report by DDC is not authorized."
- (3) "U. S. Government agencies may obtain copies of this report directly from DDC. Other qualified DDC users shall request through _____."
- (4) "U. S. military agencies may obtain copies of this report directly from DDC. Other qualified users shall request through _____."
- (5) "All distribution of this report is controlled. Qualified DDC users shall request through _____."

If the report has been furnished to the Office of Technical Services, Department of Commerce, for sale to the public, indicate this fact and enter the price, if known.

11. SUPPLEMENTARY NOTES: Use for additional explanatory notes.

12. SPONSORING MILITARY ACTIVITY: Enter the name of the departmental project office or laboratory sponsoring (paying for) the research and development. Include address.

13. ABSTRACT: Enter an abstract giving a brief and factual summary of the document indicative of the report, even though it may also appear elsewhere in the body of the technical report. If additional space is required, a continuation sheet shall be attached.

It is highly desirable that the abstract of classified reports be unclassified. Each paragraph of the abstract shall end with an indication of the military security classification of the information in the paragraph, represented as (TS), (S), (C), or (U).

There is no limitation on the length of the abstract. However, the suggested length is from 150 to 225 words.

14. KEY WORDS: Key words are technically meaningful terms or short phrases that characterize a report and may be used as index entries for cataloging the report. Key words must be selected so that no security classification is required. Identifiers, such as equipment model designation, trade name, military project code name, geographic location, may be used as key words but will be followed by an indication of technical context. The assignment of links, rules, and weights is optional.

UNCLASSIFIED

Security Classification